NASA Contractor Report 3278

An Improved Panel Method for the Solution of Three-Dimensional Leading-Edge Vortex Flows

Volume I - Theory Document

F. T. Johnson, P. Lu, E. N. Tinoco,
and M. A. Epton

CONTRACTS NAS1-15169 and NAS1-15275
JULY 1980

NASA

NASA Contractor Report 3278

An Improved Panel Method for the Solution of Three-Dimensional Leading-Edge Vortex Flows

Volume I - Theory Document

F. T. Johnson, P. Lu, E. N. Tinoco,
and M. A. Epton
Boeing Aerospace Company
Seattle, Washington

Prepared for
Langley Research Center
under Contracts NAS1-15169 and NAS1-15275

NASA
National Aeronautics
and Space Administration

**Scientific and Technical
Information Office**

1980

CONTENTS

FIGURES

FIGURES (CONCLUDED)

1.0 SUMMARY

An improved panel method for the solution of three dimensional flow about wing and wing-body combinations with leading edge vortex separation is presented. The method employs a three-dimensional inviscid flow model in which the configuration, the rolled-up vortex sheets, and the wake are represented by quadratic doublet and linear source distributions. The strength of the singularity distribution as well as shape and position of the vortex spirals are computed in an iterative fashion starting with an assumed initial sheet geometry. The method calculates forces and moments as well as detail surface pressure distributions. Improvements include the implementation of improved panel numerics for the purpose of eliminating the highly non-linear effects of ring vortices around doublet panel edges, and the development of a least squares procedure for damping vortex sheet geometry update instabilities.

The documentation is divided up into two parts:

Volume I	Theory Document
Volume II	User's Guide and Programmer's Document

Volume I contains a complete description of the method. A variety of cases generated by the computer program implementing the method are presented. These cases are of two types. The first type consists of numerical studies, which verify the underlying mathematical assumptions of the method and moreover show that the results are strongly invariant with respect to such user dependent input as wing panel layout, initial sheet shape, sheet rollup, etc. The second type consists of cases run for the purpose of comparing computed results with experimental data, and these comparisons verify the underlying physical assumptions made by the method.

Volume II contains instructions for the proper set up and input of a problem into the computer code. Program input formats and output are described. A description of the computer program and its overlay structure is also presented.

2.0 INTRODUCTION

2.1 Background

The flow at the leading and tip edges of a swept wing with sharp edges separates at moderate to high angles of attack, the separation producing vortex sheets that roll up into strong vortices above the upper surface of the wing. The formation of these vortices is responsible for the well-known nonlinear aerodynamic characteristics exhibited over the angle-of-attack range, (Figure 1). Experimental studies (ref. 1) of the vortex sheet separating from a slender sharp-edged wing revealed that the rolled-up part of the vortex sheet consists of three regions: an outer, convection dominated region in which the distance between turns is large compared to the diffusion distance; and an inner region where the distance between turns is of the same order of magnitude as the diffusion distance; and inner, diffusion-dominated, viscous core which is very small, representing only about 5 percent of the vortex diameter. In addition, studies (refs. 1, 2) of the principal vortex indicate that its shape and strength are relatively independent of Reynolds number. The relative lack of viscosity dependence suggests that the flow may be regarded as potential, with the free shear layer represented either as a vortex sheet or, equivalently, a doublet distribution, supporting a discontinuity in tangential velocity.

Many theoretical methods have exploited this fact to predict various flow characteristics. The leading-edge-suction analogy described in references 3, 4, and 5 provides a method suitable for calculating the magnitude of the nonlinear vortex lift on a rather broad class of wing planforms. Polhamus (ref. 3) reasoned that the normal force needed for the flow around a leading edge to reattach to the wing is equivalent to the leading edge suction force necessary to force the flow to be attached to the leading edge in an unseparated condition. The unseparated leading edge suction force is calculated, and is then rotated normal to the wing to obtain the lift contribution of the leading edge vortex. The total wing lift computed by this method agrees well with experimental data, but the leading-edge-suction analogy does not give flow-field details or detailed surface pressure distributions. Several attempts had been made in the past toward the theoretical prediction of detailed pressure distributions and flow fields about swept wings with leading edge vortex separation. Most of these past methods are limited to slender configurations, a considerable simplification because the problem can be reduced to a solution of Laplace's equation in the cross flow plane, for which conformal mapping becomes a powerful tool. Smith (ref. 6) developed the best known method of this type by improving the work done earlier in collaboration with Mangler (ref. 7). Assuming conical flow, which is approximately valid near the apex of the wing, he was able to predict qualitatively the type of pressure distributions that had been observed experimentally. Those pressure distributions exhibit a vortex-induced pressure peak at about 70 percent of the local semispan of the wing. Toward the trailing edge, Smith's method overpredicts the experimental load distribution by a considerable amount, because the conical theory

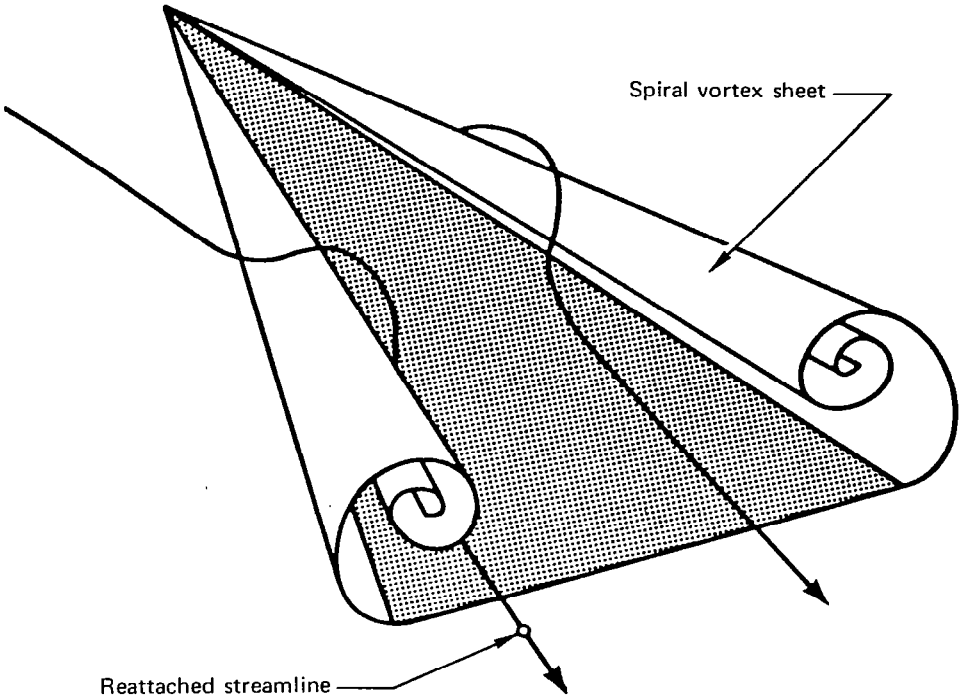

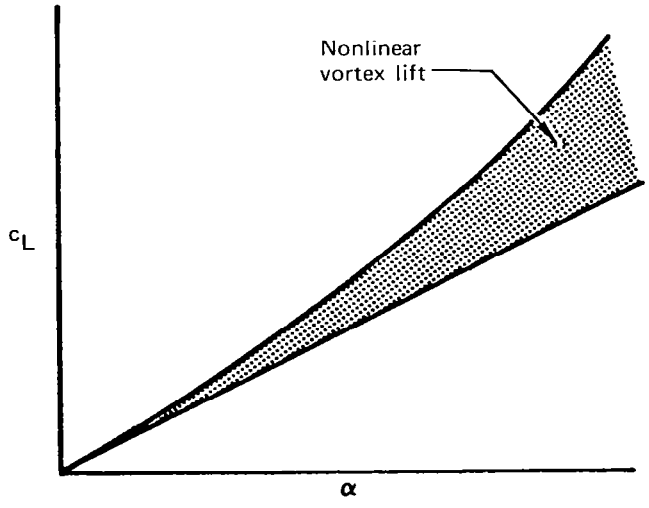

FIGURE 1 LEADING EDGE VORTEX FLOW

does not satisfy the Kutta condition at the trailing edge. Conical flow methods were followed by fully three-dimensional techniques in which the vortex is represented by single or multiple line vortices (refs. 8-13) or by a vortex sheet (refs. 14-16), and in which the trailing edge Kutta condition is enforced. These methods have enjoyed reasonable success in predicting overall configuration forces and moments and in some cases wing pressure distributions. A current review of various methods is presented in reference 17.

The method presented in this report is basically that of reference 15. This method was originally developed by the Boeing Company under contracts NAS1-12185 and NAS1-13833 from the Langley Research Center. The method is capable of predicting forces, moments and detailed surface pressures on wing and wing/body combinations assuming the separation lines are known. The wing geometry may be arbitrary in the sense that leading and trailing edges may be curved or kinked and the wing may have arbitrary camber and twist as long as in real flow it produces only a single well developed vortex system. The method employs an inviscid flow model in which the configuration surface is represented by source and/or doublet singularity panels, and the rolled-up vortex sheets and wakes are represented by doublet panels alone. The Kutta condition is imposed along all wing edges. Strengths of the singularities as well as shape and position of the free vortex sheet spirals are computed iteratively starting with an assumed initial sheet geometry. The original method had been in use for some time now with generally good results, however certain shortcomings had become apparent. First the iterations determining sheet shape and position became unstable in seemingly random cases, making parametric studies difficult (reference 18). Minor changes in wing paneling, for example, have sometimes caused a well converged case to diverge. Secondly, computed lift coefficients for wings of large aspect ratio tended to be higher than those predicted by the suction analogy and experiment (reference 18). The effort to solve these problems became the focus of contracts NAS1-15169 and NAS1-15275 from the Langley Research Center. A coordinated effort which also included work conducted for the Boeing Independent Research and Development Program was ultimately successful in overcoming these deficiencies. The effort to solve these problems is summarized in the following sections. For purposes of completeness the independent Boeing work is included in this documentation.

2.2 Approach to the Problem

The convergence problem was addressed first in the hope of creating a more reliable tool for investigating the aspect ratio problem. To improve confidence in the numerical features of the method a general upgrade of the numerics was made. The upgrade included such minor things as more precise calculation of the geometry and network edge matching sensitivities, but the major effort was the implementation of parametrized panels and doublet splines in order to ensure continuity of geometry and doublet singularity strength across all panel edges, thereby eliminating the highly non-linear effects of line vortices (discontinuities in doublet strength). This upgrade did indeed enlarge the class of problems over which convergence was achieved; nevertheless some rather simple cases

still diverged. It was therefore necessary to look at more fundamental possibilities. A detailed analysis of divergence indicated that because of certain paneling anomalies, satisfaction of some of these boundary conditions required rather substantial kinks in the vortex sheet locally which, as pointed out by Rubbert, set off a built-in instability in the vortex sheet updating procedure. A very simple least-squares penalty technique was developed to damp this instability with the result that convergence was achieved in all of a wide variety of previously diverged cases to which the technique was applied.

It has been the author's belief that the lift coefficients calculated by the current method should tend to agree with those of the suction analogy wherever the assumptions of that theory are valid; hence the attack on the second problem began with studies designed to check the numerical implementation of the method. These studies included the determination of the effect of variations in panel density, panel layout, sheet roll-up, initial sheet shape, etc. In all cases the studies proved that the boundary value problem associated with the model was being solved quite accurately so that the model itself was in error. It was subsequently discovered that use of the linearized pressure formula in the wing wake (known to be somewhat inadequate at low aspect ratios) was causing substantial loss of the wing trailing edge Kutta condition at high aspect ratios. The use of a fixed design wake then eliminated the problem and produced excellent lift coefficient comparisons.

The remainder of this report is organized as follows: Section 4 describes the general features of the current method as a point of departure for section 5 where the advances leading to the solution of the aforementioned problems are detailed. Section 6 gives examples of numerical verification of the method and Section 7 gives examples verifying the physical assumptions of the model. An appendix containing further details of some of the features of the method is also included. A users guide and programmers document is provided in a separate volume.

3.0 NOMENCLATURE

a	tangent basis vector
A	compressibility matrix
AR	aspect ratio
b	local span
B	boundary of fluid domain
c	chord
C_D	drag coefficient
C_ℓ	rolling moment coefficient
C_L	lift coefficient
C_N	normal force coefficient
C_M	pitching moment coefficient
C_P	pressure coefficient
D	fluid domain
F	equations determining singularity parameters
$\vec{F}$	force vector
G	equations determining vortex geometry parameters
H	hyperboloidal panel
K	equations penalizing panel twist
ℓ	panel width
$\hat{\ell}$	unit vector along vortex core or network junction
L	curve on B across which μ is discontinuous
M	number of grid point rows on a network
M_∞	free stream Mach number
$\hat{n}$	surface unit normal vector
$\vec{n}$	normal vector at panel center

NOMENCLATURE (CONTINUED)

$\vec{n}_c$	surface co-normal center
N	number of grid point columns on a network
p	pressure
p_i	isentropic pressure
p_2	second-order pressure
$\vec{P}$	field point
$\vec{Q}$	point on boundary B
$\vec{Q}_i$	nine canonical panel points
$\vec{Q}_o$	panel center
$\vec{Q}_s, \vec{Q}_t, \vec{Q}_{st}$	parametric coefficients defining H
R	compressible magnitude of $\vec{R}$
$\vec{R}$	vector from $\vec{Q}$ to $\vec{P}$
s,t	hyperboloidal surface parameters
S	singularity surface
$\vec{v}$	perturbation velocity
$\vec{V}$	total velocity
$\vec{V}_A$	average surface value of total velocity
V_∞	free stream velocity magnitude
$\vec{V}_\infty$	free stream velocity
$\vec{w}$	perturbation mass flux vector
$\vec{W}$	total mass flux vector
$\vec{W}_A$	average surface value of toal mass flux vector
$\hat{x}$	unit vector along x-axis
x,y,z	Cartesian coordinates
α	angle of attack

NOMENCLATURE (CONTINUED)

β	$\sqrt{1 - M^2}$
γ	delta wing semi apex angle
γ	ratio of specific heats
Δ	jump in quantity across singularity surface or line
Δ	change in quantity from one iteration to the next
δ	flap angle
ζ	surface vorticity vector
η	span fraction
θ	vortex system orientation angles
Θ	all vortex systems geometry parameters
λ	vortex system scale factor
Λ	all singularity parameters
μ	doublet strength
μ_i	doublet strength at Q
ν	fed sheet scale factor
ξ	chord fraction aft of trailing edge
(ξ, η, ζ)	panel point coordinates in local panel coordinate system
ρ	fluid density
ρ	Newton iteration step size limiter
ρ_∞	free stream fluid density
σ	source strength
ϕ	perturbation potential
(ϕ_x, ϕ_y, ϕ_z)	gradient of perturbation potential
$\bar{\nabla}$	gradient operator

NOMENCLATURE (CONCLUDED)

$\tilde{\nabla}$	co-gradient operator
ϵ	belongs to
$\otimes$	vector cross product

4.0 DESCRIPTION OF THE METHOD

4.1 Theoretical Model

The essential elements of the present flow model, as outlined in Figure 2, are the configuration surfaces (wing, body, etc.), the trailing sheet (wake), the sheet emerging from the wing leading edge and tip (free sheet), and the rolled-up core or spiral region (fed sheet) fed by the leading-edge and tip-vortex sheets. The following boundary conditions are imposed on these elements:

- o The configuration surface must be impermeable.
- o The free sheet and wake cannot support a pressure difference and must be impermeable as well.
- o The fed sheet is an extension of the free sheet and feeds vorticity to the vortex core (modeled as a simple line vortex). The boundary condition governing fed sheet size and core orientation is that the total force induced on the fed sheet and core by the rest of the configuration be parallel to the core. The size of the fed sheet is chosen initially by experience or from the conical flow results of Smith (ref. 6).
- o Kutta conditions are imposed along the appropriate leading, side, and trailing edges of the wing in the presence of free sheets emanating from these edges.

4.2 Basic Concepts

The Prandtl-Glauert equation

$$\beta^2 \phi_{xx} + \phi_{yy} + \phi_{zz} = 0, \ \beta^2 = 1 - M_\infty^2 \qquad (1)$$

is assumed to govern the perturbation velocity potential ϕ in the flow field about the configuration. Here the x-axis is taken as the freestream direction, i.e. $\vec{V}_\infty = V_\infty \hat{x}$, where $\vec{V}_\infty$ is the freestream velocity and $\vec{V}$ its magnitude. Total velocity V is then defined by $\vec{V} = \vec{V}_\infty + \vec{v}$, where $\vec{v} = ((\phi_x, \phi_y, \phi_z))$ is the perturbation velocity. The definition of impermeability and pressure appropriate to equation (1) is an open subject. The mathematically natural choice of zero normal mass flux and the second order pressure formula (reference 19) is preferred. The total mass flux vector $\vec{W}$ is defined as

$$\vec{W} = \rho_\infty \vec{V}_\infty + \vec{w} \qquad (2)$$

where w is the perturbation mass flux vector defined by

$$\vec{w} = \rho_\infty (\beta^2 \phi_x, \phi_y, \phi_z) \qquad (3)$$

- **DIFFERENTIAL EQUATION**

$$(1 - M_\infty^2)\,\phi_{xx} + \phi_{yy} + \phi_{zz} = 0$$

- **BOUNDARY CONDITIONS**
  - WING, BODY : IMPERMEABLE
  - WAKE, FREE SHEET: IMPERMEABLE ZERO PRESSURE JUMP
  - FED SHEET; ZERO TOTAL FORCE
  - KUTTA CONDITION

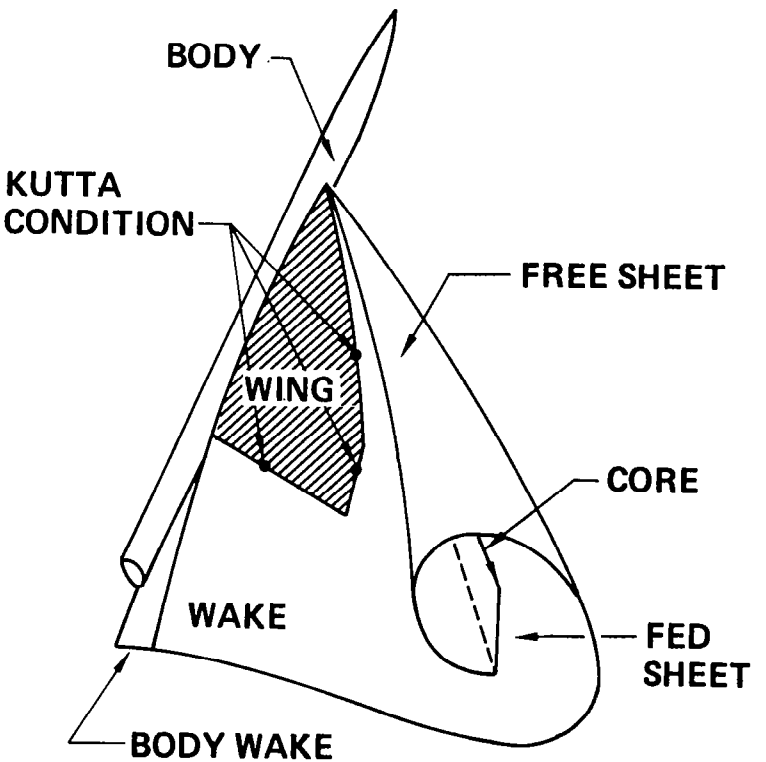

FIGURE 2 FLOW MODEL

To first order in perturbation quantities $\vec{W}$ is equal to $\rho\vec{V}$ (reference 19) hence impermeability can be expressed by

$$(\vec{W} \cdot \hat{n}) = 0 \tag{4}$$

where n is the surface normal. Equation (1), rewritten as $\vec{\nabla} \cdot \vec{W} = 0$, expresses conservation of mass, and equation (4) then guarantees that even if the configuration is such that the assumptions used to derive equation (1) are violated locally there is still no net production of fluid at the boundary surfaces.

The second order pressure formula is

$$p_2 = p_\infty - [\rho_\infty(\vec{V}_\infty \cdot \vec{v}) + \tfrac{1}{2}(\vec{v} \cdot \vec{w})] \tag{5}$$

and it agrees with the isentropic formula

$$p_i = p_\infty + \frac{\rho_\infty V_\infty^2}{\gamma M_\infty^2}\left\{\left[1 - \frac{\gamma-1}{2}\frac{M_\infty^2}{V_\infty^2}\left(|\vec{V}|^2 - V_\infty^2\right)\right]^{\frac{\gamma}{\gamma-1}} - 1\right\} \tag{6}$$

to first order in perturbation quantities. Mathematically the second order formula is closely associated with equations (1) an (4) in that equation (1) is simply the Euler-Lagrange equation for the Bateman variational principle,

$$\iiint_D p_2 \, dD = \text{stationary} \tag{7}$$

for which specification of $(\vec{W} \cdot \hat{n})$ is the natural Neumann boundary condition. Of great importance in this case is that the second order pressure formula produces consistent force calculations for arbitrary configurations when force is defined in the usual way, i.e.,

$$F = -\iint_S [\vec{V}(\vec{W} \cdot \hat{n}) + p_2 \hat{n}] \, dS \tag{8}$$

Equation (1) implies that $\vec{F}$ is zero when the surface S encloses fluid only, hence momentum is conserved exactly and the force on a given surface may be computed on any enclosing surface.

Under rather general assumptions Green's third identify (references 20, 21) shows that any solution of (1) at a field point $\vec{P}$ may be expressed as the potential induced by a combination of source singularities of strength $\sigma(\vec{Q})$ and doublet singularities of strength $\mu(\vec{Q})$ on the boundary $\vec{Q} \epsilon$ B of the fluid domain D:

$$\phi(\vec{P}) = \iint_B \sigma(\vec{Q})\left(\frac{-1}{4\pi R}\right) dS_Q + \iint_B \mu(\vec{Q}) \hat{n} \cdot \vec{\nabla}_Q\left(\frac{1}{4\pi R}\right) dS_Q \tag{9}$$

Here $\vec{R}$ is the position vector $\vec{P}-\vec{Q}$, R is the compressible magnitude of $\vec{R}$ defined by

$$R = \sqrt{\vec{R} \cdot A \cdot \vec{R}} \qquad \text{where} \qquad A = \begin{pmatrix} 1 & 0 & 0 \\ 0 & \beta^2 & 0 \\ 0 & 0 & \beta^2 \end{pmatrix} \tag{10}$$

and $\vec{\nabla}_Q$ is the co-gradient with respect to $\vec{Q}$ defined by

$$\vec{\nabla}_Q = \beta^2 \, A^{-1} \, \vec{\nabla}_Q \tag{11}$$

The perturbation velocity $\vec{v}(\vec{P})$ associated with ϕ may be computed by differentiating (9):

$$\vec{v}(\vec{P}) = \iint_B \sigma(\vec{Q}) \vec{\nabla}_P \left(\frac{-1}{4\pi R}\right) dS_Q + \iint_B \mu(\vec{Q}) \hat{n} \cdot \vec{\nabla}_Q \left(\vec{\nabla}_P \frac{1}{4\pi R}\right) dS_Q \tag{12}$$

whereupon application of Stokes' theorem to the second term on the right yields

$$\begin{aligned} \vec{v}(\vec{P}) = & \iint_B \sigma(Q) \vec{\nabla}_P \left(\frac{-1}{4\pi R}\right) dS_Q + \cdots \\ & \cdots \iint_B \vec{\zeta}(\vec{Q}) \otimes \vec{\nabla}_Q \left(\frac{1}{4\pi R}\right) dS_Q + \\ & \cdots \int_L \Delta\mu(\vec{Q}) \vec{\nabla}_Q \left(\frac{1}{4\pi R}\right) \otimes d\vec{\ell} \end{aligned} \tag{13}$$

Here $\vec{\zeta}(\vec{Q})$ is the surface vorticity vector defined by

$$\vec{\zeta} = \hat{n} \otimes \vec{\nabla} \mu \tag{14}$$

and L is any curve on B across which μ has a discontinuity, say $\Delta\mu$.

It is possible to show from equations (8), (9), (12), and (13) that across any singularity surface S

$$\Delta\phi = \mu \tag{15}$$

$$\hat{n} \otimes \Delta \vec{V} = \vec{\zeta} \tag{16}$$

$$(\hat{n} \cdot \Delta \vec{W}) = \rho_\infty \sigma \tag{17}$$

$$\Delta p_2 = -[\vec{n}_c \cdot (\vec{W}_A \otimes \vec{\zeta}) + (\vec{W}_A \cdot \hat{n}) \sigma] / (\hat{n} \cdot \vec{n}_c) \tag{18}$$

and

$$\Delta\vec{F} = -\iint_S [\vec{W}_A \otimes \vec{\zeta} - \vec{V}_A \rho_\infty \sigma]\, dS + \int_L \mu \vec{W}_A \otimes d\vec{\ell} \qquad (19)$$

where Δ denotes the difference between the value on the side on which $\hat{n}$ is defined and the other side, and the subscript A denotes the average of the two values. Here $\vec{n}_c$ is the co-normal defined by

$$\vec{n}_c = \beta^2 A^{-1} \hat{n} \qquad (20)$$

4.3 Mathematical Implementation of the Model

The mathematical implementation of the boundary value problem set forth in section 4.1 is now described. Our basic unknowns are the source and doublet strengths on all surfaces and the position of the free, fed and wake sheet surfaces. To solve for these unknowns the following equations are derived.

On a surface bounding the fluid on both sides (i.e., thin sheets such as the free sheet, wake and possibly wing) it is required that equation (4) hold on both sides so that from equation (17) it can be seen that such a surface is source free. Hence, these two boundary conditions can be replaced by the equivalent conditions that the surface be a doublet surface and that

$$(\vec{W}_A \cdot \hat{n}) = 0 \qquad (21)$$

On the wake and free sheet surfaces we have the additional requirement that

$$\Delta p_2 \equiv -\vec{n}_c \cdot (\vec{W}_A \otimes \vec{\zeta}) / (\hat{n} \cdot \vec{n}_c) = 0 \qquad (22)$$

Although both equations involve doublet strength and surface geometry, the primary function of equation (22) in conjunction with equation (12) is to define surface doublet strength whereas the function of equation (21) is to define the surface normal and hence surface geometry. An approximation often made by many methods for wake surfaces is that

$$\vec{W}_A \approx \rho_\infty \vec{V}_\infty \qquad (23)$$

in which case equations (22) and (21) determine wake vorticity and surface slope prior to solution. Such an approximation is not precisely valid but can nevertheless be made at least in the far wake because details of the wake flow there have little effect on wing pressures. However a more accurate representation is sometimes required in the near wake, primarily because the spanwise component of vorticity in the near wake (which can be large in that a portion of the wake is underneath the primary vortex core) has a strong influence on the Kutta condition at the wing trailing edge. In this case the solution approach used is to require that equation (22)

be satisfied on a fixed wake surfaces in the immediate vicinity of the wing trailing edge, which causes the wake vorticity to seek the correct lateral alignment there.

The Kutta condition at the junction of a (thin) wing and vortex sheet can be stated in several ways; e.g., zero pressure jump at the wing edge, finite flow at the wing edge, no flow through the vortex sheet, etc. All of these phenomena are supposed to occur once the Kutta condition is satisfied, and which boundary condition is actually called the Kutta condition depends on which boundary conditions have previously been assigned to the wing and vortex sheet. In this case it has already been assumed that equation (21) holds on the wing and equation (22) on the sheet, neither of which guarantee finite flow at the wing edge. Infinite flow can be created only by a discontinuity in doublet strength or surface vorticity across the wing/sheet junction. A discontinuity in doublet strength creates a line vortex of strength equal to the discontinuity (equation 13). The powerful flow singularity induced by such a vortex is incompatible with wing impermeability and hence a discontinuity in doublet strength is already prevented by the wing boundary condition equation (21). However the weak flow singularity induced by a discontinuity in the surface vorticity vector $\vec{\zeta}$ is not. In fact there exist vorticity distributions creating infinite velocities at the junction, yet no normal mass flux on the wing, nor pressure jump on the vortex sheet. These distributions are such that $\vec{\zeta}\cdot\hat{\ell}$ tends to infinity as the junction is approached from the wing side, where $\hat{\ell}$ is the unit vector along the junction. Thus the choice as the Kutta condition (as originally proposed by Rubbert) is that $\vec{\zeta}\cdot\hat{\ell}$ be continuous from the wing to the vortex sheet, i.e., that $\Delta\vec{\zeta}\cdot\hat{\ell} = 0$ where $\Delta\vec{\zeta} = \vec{\zeta}_{vortex} - \vec{\zeta}_{wing}$. Other components of $\vec{\zeta}$ may be discontinuous; however these discontinuities will be eliminated by the process of updating the vortex sheet to satisfy equation (21) (which can only happen if the surface normal n is continuous across the junction).

Following Smith (reference 6), the purpose of the fed sheet is to condense the free sheet vorticity into a line vortex core, thereby terminating the free sheet rollup. Hence the fed sheet is chosen to be a doublet sheet whose strength is equal to the doublet value at the junction with the free sheet. Only the size and position of the fed sheet remain to be determined from boundary conditions. The boundary conditions are chosen to be consistent with those that would be applicable to the infinitely rolled up vortex sheet as well, namely that the total force normal to the core be zero, i.e., $\hat{\ell}\otimes\Delta\vec{F} = 0$ where $\hat{\ell}$ is the unit vector along the line vortex core and $\Delta\vec{F}$ is given by equation (19).

On surfaces bounded on one side by a non-fluid domain (e.g., body or thick wing) it is required that equation (4) hold on the fluid side. While this boundary condition formally completes the mathematical description of the boundary value problem set forth in section 4.1, it is not sufficient to guarantee a unique solution to the problem via equation (12) since both source and doublet strength on such surfaces cannot be determined by one boundary condition. However a (nearly) arbitrary boundary condition can be assigned to the other side (reference 22). In particular assigning

to ϕ the same value as on the fluid side implies $\mu = 0$ in view of equation (15) and leads to pure source surface modeling. Here, however, a doublet lifting surface is required inside the wing and a doublet lift carry-over surface is required inside the body. (Models using doublet singularities on the thick wing and body surfaces are also possible (reference 22) but have not yet been implemented).

Summarizing the mathematical description of the boundary value problem described in section 4.1, the following equations determine singularity strength:

$$\hat{n} \cdot \vec{W} = 0 \qquad \text{on wing and body, } \mu = 0 \text{ on body, } \sigma = 0 \text{ on thin wing}$$

$$\sigma = 0, \Delta p_2 = 0 \qquad \text{on free sheet and near wake}$$

$$\Delta\vec{\zeta} \cdot \hat{\ell} = 0 \qquad \text{on wing edges (Kutta condition)} \qquad (24)$$

$$\sigma = 0, \text{ continuation of } \mu \text{ on far wake, fed sheet, body wake, carry-over sheet}$$

Free and fed sheet geometry are then determined by

$$\hat{n} \cdot \vec{W}_A = 0 \qquad \text{free sheet}$$

$$\hat{\ell} \otimes \Delta\vec{F} = 0 \qquad \text{fed sheet} \qquad (25)$$

4.4 Numerical Procedure

Solution of the boundary value problem of section 4.3 via equation (12) is accomplished with the basic panel method of reference 23. The method proceeds by dividing the boundary surface into networks. A network is defined as a smooth portion of the boundary which has subsequently been divided into panels and on which source and/or doublet splines have been defined accompanied by properly posed boundary conditions. The networks are assumed to be logically independent in that each network contributes as many equations as unknowns to the overall boundary value problem; hence networks can be added or dropped without total reformulation of the problem. Essential features of the computational scheme are summarized below.

- Geometry input for a network consists of a rectangular array of corner point coordinates. The portion of the surface lying between four adjacent corner points is approximated by an analytically defined panel.

- Discrete values of singularity strength are assigned to certain standard points on each network. These values are interpolated by source and doublet splines which on each panel are assumed to be defined by linear and quadratic distributions respectively.

- Certain standard points on each network are assigned as control points at which boundary conditions are applied. These points include panel center points as well as edge abutment points in the case of doublet networks. The latter serve to impose standard aerodynamic edge conditions automatically (for example, the Kutta condition, zero potential jump at thin edges, and continuity of singularity strength across abutting networks).

- The induced potential and velocity integrals of equation (12) (influence coefficients) are all evaluated in closed form, although standard far field expansions are employed when the control point is sufficiently distant from the influencing panel.

Figure 3 displays the location of discrete singularity parameters and control points for various network types. These locations are selected to achieve singularity spline stability with respect to the type of boundary conditions applied at the control points (reference 24). Additional details may be found in appendix E. Figure 4 shows a typical thin-wing/body configuration paneling and Figure 5 shows the same configuration disassembled into networks. Control points located at the junction of two doublet networks (or at the junction of one network with empty space) are assigned to match singularity strength across the junction. If only one control point exists, doublet value is matched. If there are two opposing control points the component of vorticity along the junction is also matched. Control points at panel centers have the boundary conditions prescribed in section 4.3.

In Figure 6 the free and fed sheet kinematics are illustrated. The fed sheet size and position in each x-cut are changed by varying the scale parameters λ and ν, the parameter λ scaling the whole vortex system. The free sheet shape is changed by varying the panel orientation angles θ_i, keeping the relative lengths ℓ_i fixed. Note that the vortex system geometry has as many degrees of freedom as constraint equations (25).

Let all geometry degrees of freedom be denoted by the vector Θ and all singularity parameters be denoted by Λ. The equation set (24) can now be denoted by

$$F(\Lambda, \Theta) = 0 \tag{26}$$

and the equation set (25) by

$$G(\Lambda, \Theta) = 0 \tag{27}$$

These equations are solved iteratively by Newton's method with controlled step size, i.e.,

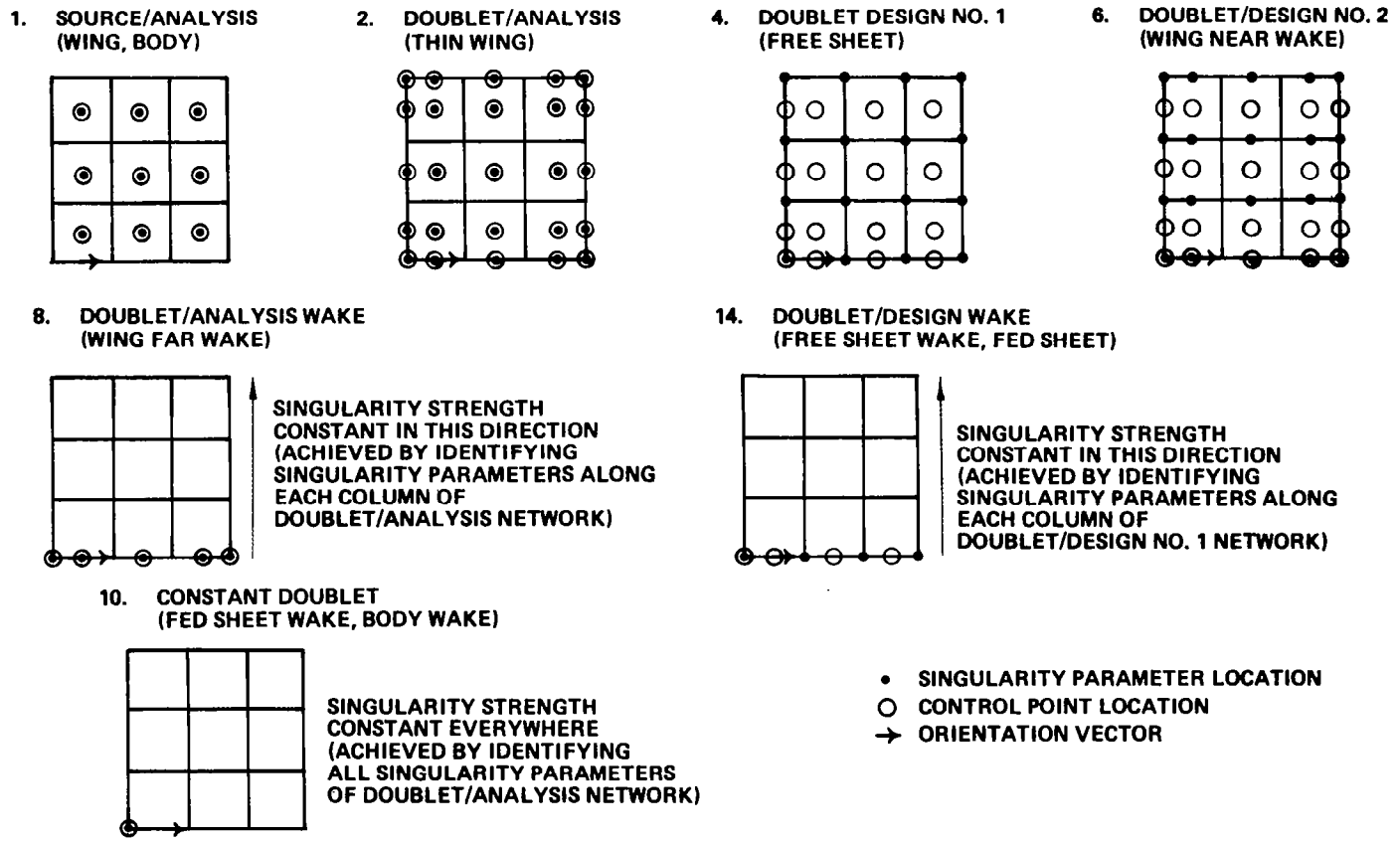

FIGURE 3 LOCATION OF DISCRETE SINGULARITY PARAMETERS AND CONTROL POINTS FOR VARIOUS NETWORK TYPES

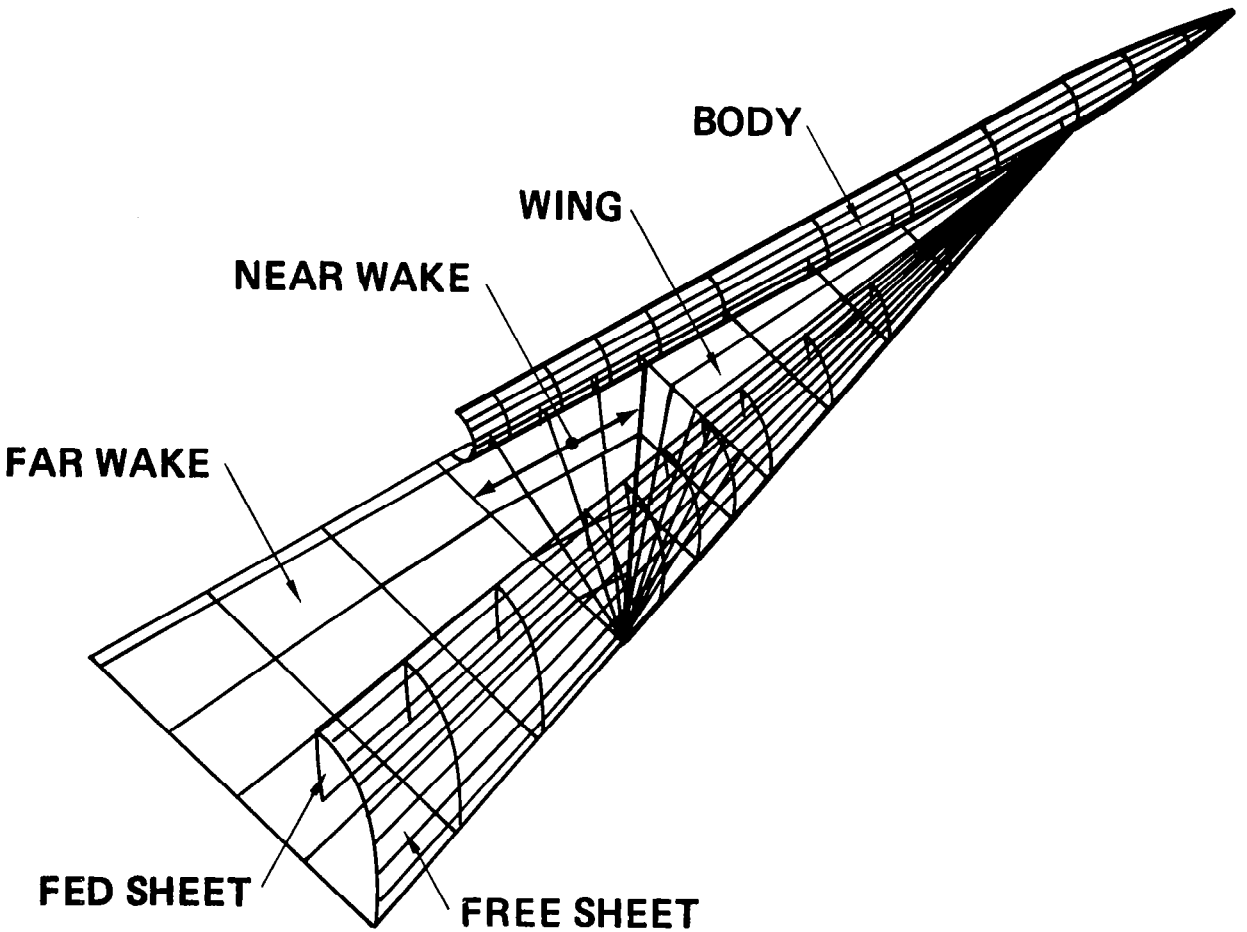

FIGURE 4 PANEL MODEL

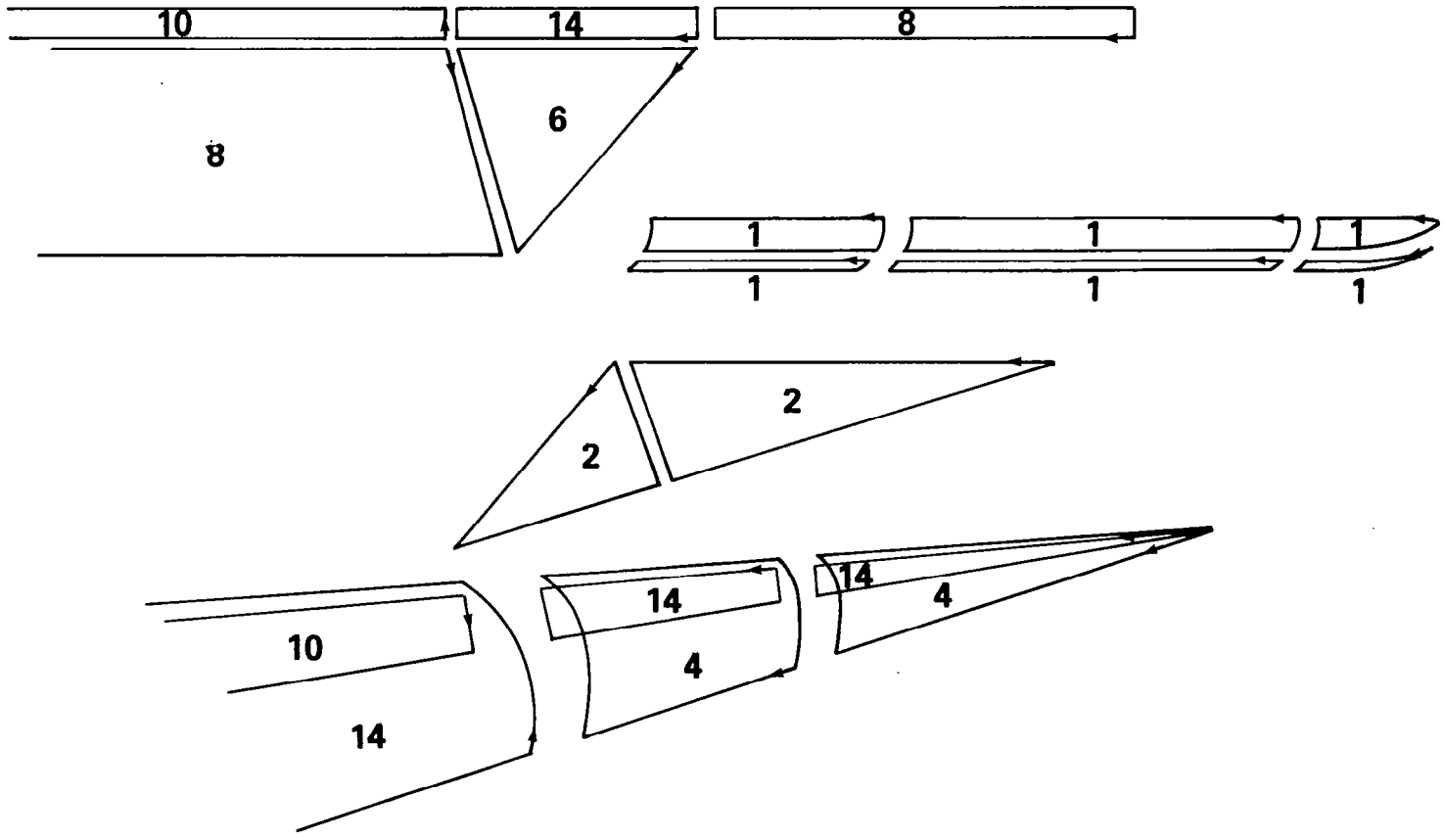

FIGURE 5 NETWORKS COMPRISING PANEL MODEL

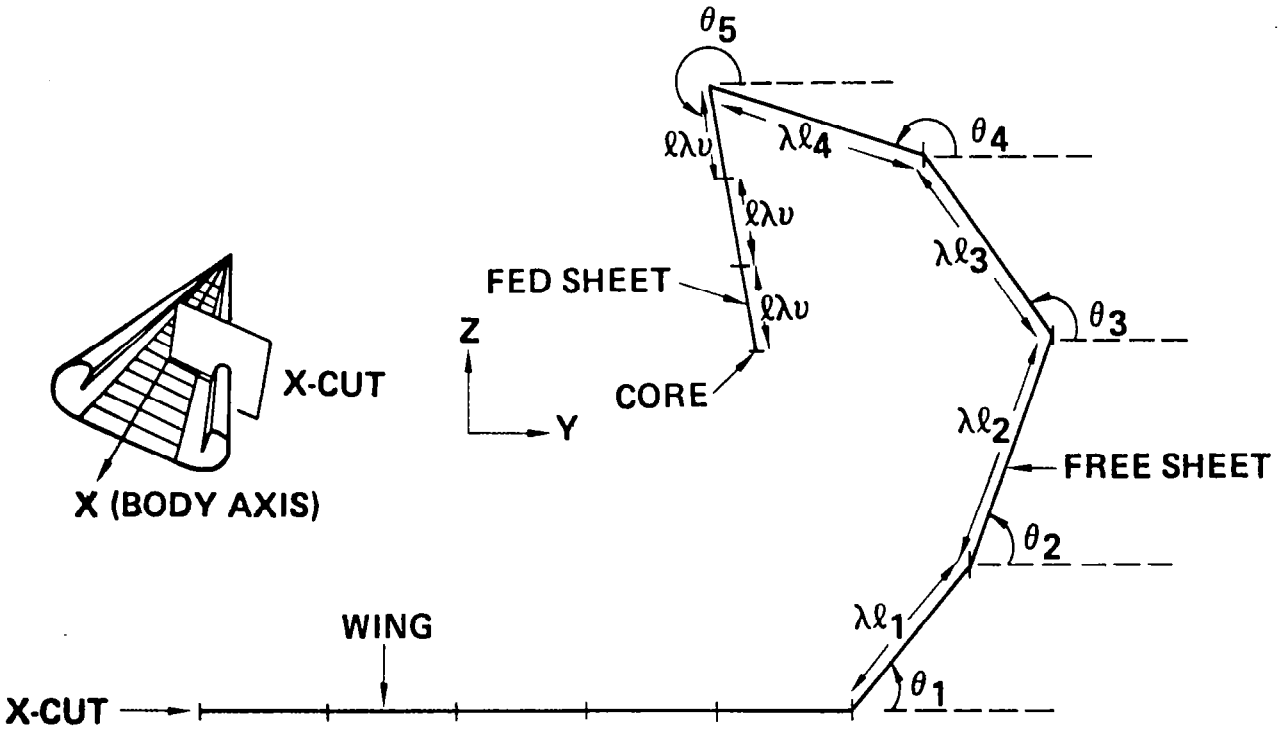

FREE PARAMETERS: $\theta_1, \theta_2, \theta_3, \theta_4, \lambda, \upsilon$

FIXED PARAMETERS: $\ell_1, \ell_2, \ell_3, \ell_4, \theta_5, \ell$

FIGURE 6 FREE/FED SHEET KINEMATICS

$$\begin{pmatrix} \frac{\partial F}{\partial \Lambda} & \frac{\partial F}{\partial \Theta} \\ \frac{\partial G}{\partial \Lambda} & \frac{\partial G}{\partial \Theta} \end{pmatrix} \begin{pmatrix} \Delta\Lambda \\ \Delta\Theta \end{pmatrix} = -\rho \begin{pmatrix} F \\ G \end{pmatrix} \tag{28}$$

where ρ represents symbolically the step size scaling parameter δ (see Appendix G). δ is a positive number less than 1 and is chosen small enough to ensure a decrease in the norms of F and G. Note that the Jacobian matrix on the left requires differentiation of the panel influence coefficients with respect to changes in geometry. Details of this differentiation will be given in the appendices.

5.0 RECENT ADVANCES

5.1 Improved Panel Numerics

Equation (13) shows that a discontinuity in doublet strength produces a line vortex of strength equal to the discontinuity. The velocity flow field induced by such a vortex has a singularity proportional to the vortex strength and inversely proportional to the distance from the vortex. Moreover the sensitivity to a change in vortex position (appearing in the Jacobian of equation (28)) has a singularity inversely proportional to the square of the distance to the vortex. It is clear that if a control point is sufficiently close to such a vortex, the linearization implicit in equation (28) will be valid for small $\Delta\Theta$ only, prolonging convergence. Fortunately the vortex core in the present model tends to stay a large (relative to its strength) distance away from wing and free sheet control points. However, our original panel discretization introduced unintentional line vortices which were of small strength, but which could be relatively close to wing and free sheet control points. These line vortices arose for two reasons. First, flat panels were generally used for efficiency reasons. These panels were the plane quadrilaterals formed by projecting the straight line segments joining the four corner points onto the plane passing through the midpoints of these line segments. This meant that gaps in geometry would be present at edges of panels belonging to networks where the corner points did not all lie in a plane, leading to ring vortices around each panel. Secondly our locally quadratic doublet distribution on each panel was defined by fitting a quadratic function to singularity parameters in an immediate neighborhood. Since each panel used different singularity parameters, continuity of doublet strength across panel edges could not be enforced, and this again led to line vortices. Even on fixed portions of the geometry these vortices created problems because the boundary condition at a panel center control point close to a discontinuity in doublet strength would occasionally attempt to suppress the singularity produced by this discontinuity, i.e., interact with the doublet spline to create greater continuity, rather than control finite flow in the appropriate manner.

In order to alleviate this problem the hyperboloidal panels of Morino (reference 25) have been implemented along with a continuous doublet spline. The hyperboloidal panel H interpolating four corner points $\vec{Q}_1$, $\vec{Q}_2$, $\vec{Q}_3$, $\vec{Q}_4$ is defined as the point set

$$H = \left\{ \vec{Q}(s,t) : \vec{Q}(s,t) = \vec{Q}_o + \vec{Q}_s s + \vec{Q}_t t + \vec{Q}_{st} st;\ s\epsilon[-1,1],\ t\epsilon[-1,1] \right\} \qquad (29)$$

where

$$\vec{Q}_o = \tfrac{1}{4}(\vec{Q}_1+\vec{Q}_2+\vec{Q}_3+\vec{Q}_4) \qquad \vec{Q}_s = \tfrac{1}{4}(\vec{Q}_1-\vec{Q}_2-\vec{Q}_3+\vec{Q}_4)$$
$$\vec{Q}_t = \tfrac{1}{4}(\vec{Q}_1+\vec{Q}_2-\vec{Q}_3-\vec{Q}_4) \qquad \vec{Q}_{st} = \tfrac{1}{4}(\vec{Q}_1-\vec{Q}_2+\vec{Q}_3-\vec{Q}_4)$$

The panel H is depicted in Figure 7.

Note that H contains the straight line segments joining the edge midpoints $\vec{Q}_5$, $\vec{Q}_6$, $\vec{Q}_7$ and $\vec{Q}_8$, the same as the flat panel, and hence H is also only a first order accurate approximation to the true surface. However H also contains the straight lines joining the corner points $\vec{Q}_1$, $\vec{Q}_2$, $\vec{Q}_3$, $\vec{Q}_4$ and so it abuts adjacent panels exactly leaving no gaps.

Doublet strength on H is defined parametrically in terms of nine doublet values μ_i at the points $\vec{Q}_i$ by the formula

$$\mu(s,t) = \mu_1[\tfrac{1}{4}st(1+s)(1+t)] + \mu_2[-\tfrac{1}{4}st(1-s)(1+t)] + \mu_3[\tfrac{1}{4}st(1-s)(1-t)] \quad (30)$$

$$+\mu_4[-\tfrac{1}{4}st(1+s)(1-t)] + \mu_5[\tfrac{1}{2}t(1+t)(1-s^2)] + \mu_6[-\tfrac{1}{2}s(1-s)(1-t^2)]$$

$$+\mu_7[-\tfrac{1}{2}t(1-t)(1-s^2)] + \mu_8[\tfrac{1}{2}s(1+s)(1-t^2)] + \mu_9[(1-s^2)(1-t^2)]$$

Note that along each of the line segments displayed in Figure 7 $\mu(s,t)$ is quadratic and is determined solely by the (three) values of doublet strength at the midpoint and endpoints of the segment. The nine doublet values μ_i of equation (30) are not all independent. On any given network the set of independent parameters determining the doublet spline on that network are the doublet values at the locations shown in figure 3, and in general these values do not include all the μ_i of all the panels. Hence the nine doublet values μ_i must be expressed in terms of the truly independent doublet singularity parameters. For this purpose an enriched set of network grid points (Figure 8) is defined which includes the original corner points, the panel edge midpoints and center points and therefore all the $\vec{Q}_i$ of all the panels. At each of these points doublet strength is obtained by fitting a quadratic function to a sufficient number of neighboring singularity parameters by the method of weighted least squares. For stability the closest singularity parameters are weighted heavily, in particular doublet strength at an enriched grid point coinciding with a singularity parameter point is simply set equal to the value of that parameter. For enriched grid points along network edges the corresponding doublet values are allowed to depend only on singularity parameters located on that edge, and for this purpose a least squares fit based on arc-length along the edge is used.

It is clear from the above construction that doublet strength will be continuous across panel edges in the interior of each network. At network junctions doublet strength can also be made continuous so long as the corner points and edge singularity parameter locations coincide. This is the case in figure 4 except for the wing/free sheet junction. (Modification of some of the edge singularity parameter locations for both doublet/design networks could eventually lead to precise continuity everywhere).

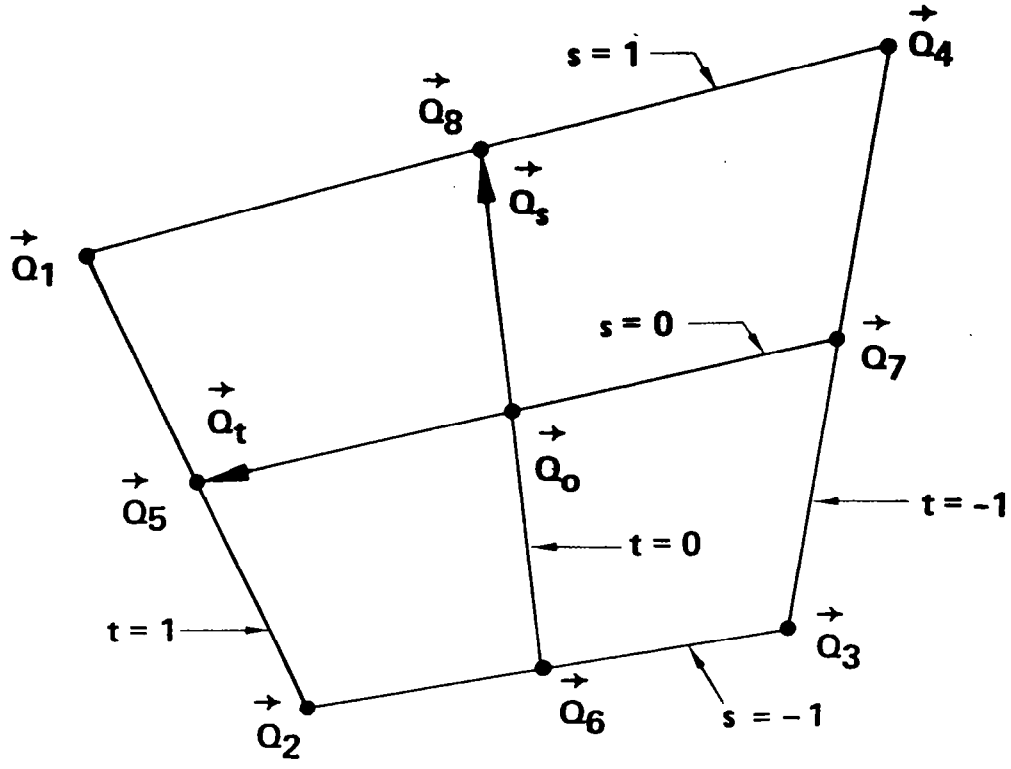

FIGURE 7 HYPERBOLOIDAL PANEL

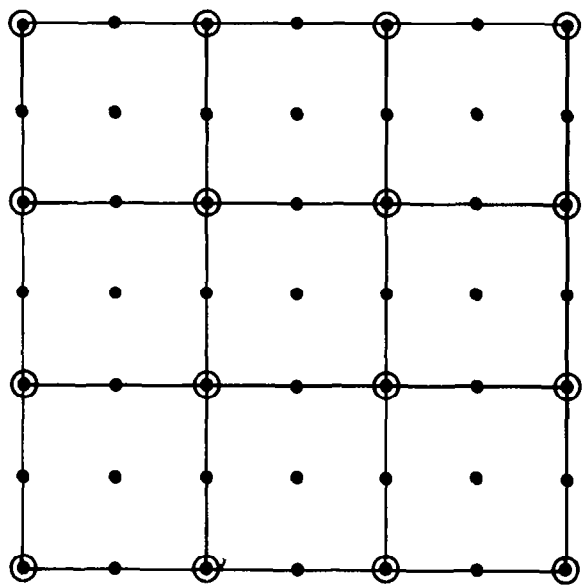

• ENRICHED GRID POINTS
○ ORIGINAL GRID POINTS

FIGURE 8 ENRICHED GRID

Calculation of the influence coefficients for the above formulation is accomplished using equation (13), where the last term on the right may now be discarded entirely except for the fed sheet terminated edge. Evaluation of the remaining integrals is facilitated by an expansion which is similar to the curved panel expansion of reference 23, but which does not require the small curvature assumption. Rewriting the second integral on the right of equation (13) in terms of the parameters s and t we obtain

$$\iint_H \vec{\zeta}(\vec{Q}) \otimes \vec{\nabla}_Q \left(\frac{1}{4\pi R}\right) dS_Q = \frac{\beta^2}{4\pi} \int_{-1}^{1}\int_{-1}^{1} \frac{1}{R^3}\left[\frac{\partial \mu}{\partial s}(\vec{a}_t \otimes \vec{a}_{to}) - \frac{\partial \mu}{\partial t}(\vec{a}_s \otimes \vec{a}_{so})\right] dsdt \tag{31}$$

where

$$\vec{R} = \vec{R}_o - \vec{Q}_s s - \vec{Q}_t t - \vec{Q}_{st} st$$

$$\vec{R}_o = \vec{P} - \vec{Q}$$

$$\vec{a}_s = \vec{Q}_s + \vec{Q}_{st} t$$

$$\vec{a}_t = \vec{Q}_t + \vec{Q}_{st} s$$

$$\vec{a}_{so} = \vec{R}_o - \vec{Q}_t t$$

$$\vec{a}_{to} = \vec{R}_o - \vec{Q}_s s$$

The term in square brackets on the right is simply a polynomial, but the integration cannot be performed in closed form since R is a quartic polynomial in s and t. However R can be approximated as follows. Let (s*,t*) minimize R on $[-1,1] \otimes [-1,1]$, so that Q(s*,t*) is a closest point on H to P in the compressible norm. Let $\vec{R}^*(s,t)$ be the quadratic part of $\vec{R}$ at the point (s*,t*), i.e.,

$$\vec{R}^*(s,t) = (\vec{R}_o - \vec{Q}_s s^* - \vec{Q}_t t^* - \vec{Q}_{st} s^* t^*) - \vec{Q}_s(s-s^*) - \vec{Q}_t(t-t^*) \tag{32}$$

Then $\left(\frac{R^*}{R}\right)^3$ is continuous in s and t and may be approximated to any accuracy by a polynomial T(s,t). Upon substitution of the approximation

$$\frac{1}{R^3} \approx \frac{T(s,t)}{R^{*3}} \tag{33}$$

into the right side of equation (31) the integration may be performed in closed form.

Evaluation of the surface vortex integral using the above procedure is quite accurate but rather expensive. Hence a somewhat simpler approximation was developed for use in the intermediate field, i.e., when the field point is a modest distance away from the panel but not sufficiently distant that a far field expansion converges. For this approximation the flat panel is used again along with the quadratic doublet distribution (based on surface coordinates (ξ , η)):

$$\mu(\xi,\eta) = \mu_0 + \mu_\xi \xi + \mu_\eta \eta + \tfrac{1}{2}\mu_{\xi\xi}\xi^2 + \mu_{\xi\eta}\xi\eta + \tfrac{1}{2}\mu_{\eta\eta}\eta^2 \qquad (34)$$

Here the coefficients are obtained by expanding equation (30) in a Taylor's series about the panel center. (Note that the doublet strength obtained from equation (34) then agrees identically with that of equation (30) along the lines s = 0 and t = 0). It was found that this approximation agreed well with the more exact calculation above - even for the field point at the panel center, hence it was decided to use it exclusively in the near field. While it would then seem that we are back to the flat panel/quadratic doublet distribution at least for the purpose of calculating influence coefficients it is important to realize that the underlying panel shape and doublet distribution are given by equations (29) and (30) respectively. With the old method it was impossible to ignore the line vortex term on the right side of equation (13) since the doublet strength could not be deduced from knowledge of the vorticity vector alone. Additional details on the hyperboloidal panels can be found in appendices A, B, C and D.

5.2 Least Squares Geometry Update Procedures

In Figure 9, a streamwise paneled delta wing with unwrapped free and fed sheets is shown. The control point on the first wing panel is displayed. The control points on the first row of panels on the free and fed sheets are also displayed along with their projection onto the wing. Since the first wing control point is so far from the apex, flow through the wing near the apex is not prevented and consequently the free and fed sheet control points in the first row encounter a somewhat different environment than those in subsequent rows. To satisfy the boundary condition at these control points the whole vortex system near the apex is required to move substantially inboard causing errors in wing pressures at the first wing control point. Obviously with such a paneling one cannot be too concerned with flow details at the apex anyway. In the past however, the flow anomaly there destroyed convergence everywhere even though the flow is better behaved farther aft on the wing.

The problem was two-fold. First, all equations of the set (25) were required to be satisfied exactly. Because huge local anomalies in vortex sheet shape were required, the singularities themselves got heavily involved in solving equation (25) with consequential loss of stability. Secondly, the update procedure was such that local anomalies in sheet shape could propagate to other areas of the sheet; in other words the procedure itself was not fully stable. The basic reason has to do with the fact that for both the flat and hyperboloidal panels, the surface

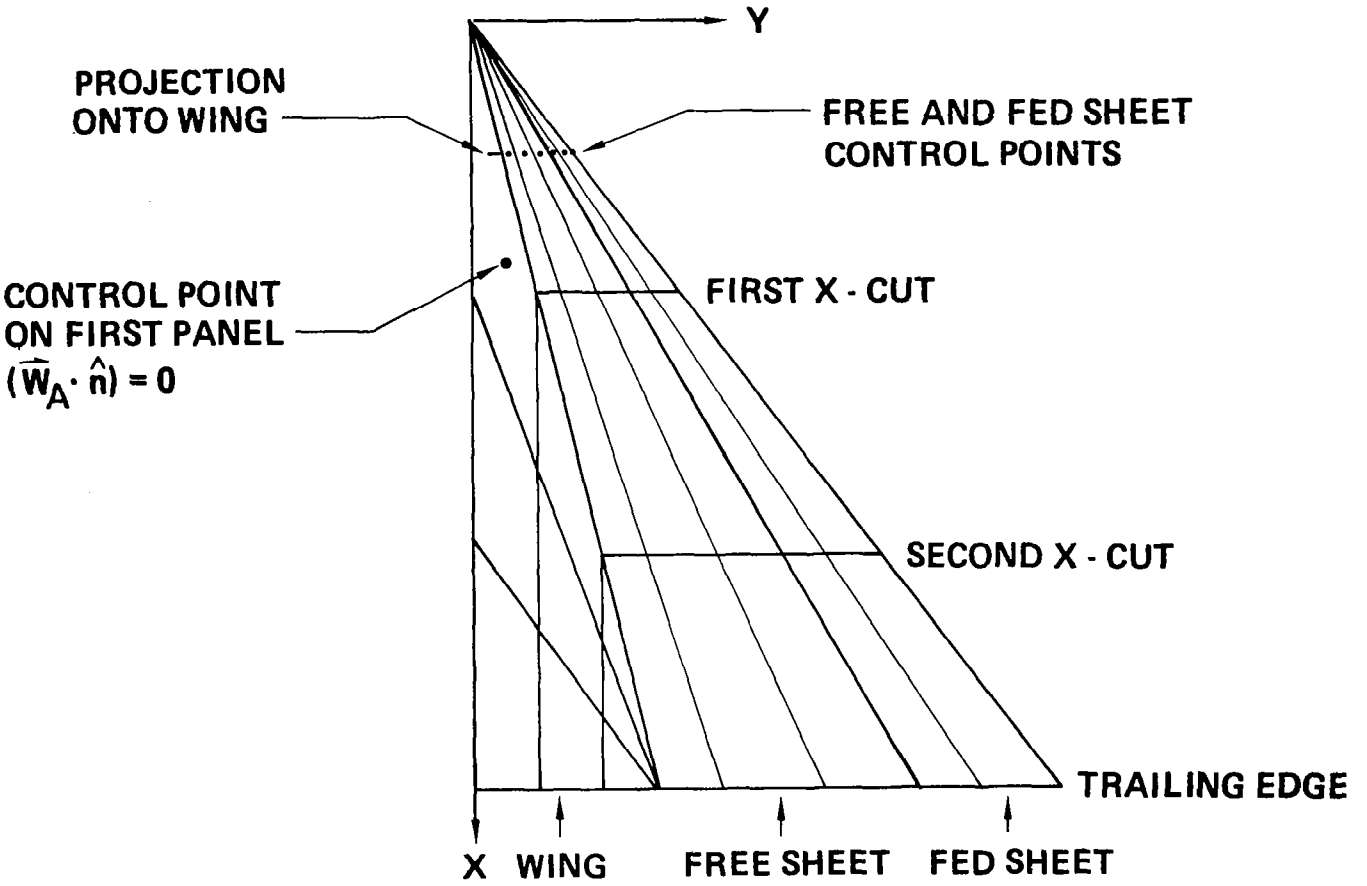

FIGURE 9 STREAMWISE PANELED DELTA WING WITH UNWRAPPED FREE AND FED SHEETS

normal at the panel center remains unchanged when the four panel corner points are alternatingly perturbed equal distances above and below the average plane. For illustration purposes assume the free sheet lies in a plane as shown in Figure 10. The average mass flux vectors at the panel centers are depicted with arrows and are assumed to lie in the plane as well, except for the mass flux vector at the center of the first panel which because of a flow anomaly is assumed to be substantially out of plane. Assume that all corner points except for those in the inboard column (which are attached to the wing) may be perturbed in a direction normal to the surface (i.e., plane) and also assume that the mass flux vector $\vec{W}$ at each panel center is little altered by such a perturbation. The boundary condition $(\vec{W} \cdot \hat{n}) = 0$ is already satisfied on all panels except the first, where a perturbation of corner point 3 by a large distance h is required to modify the panel center normal so that $(\vec{W} \cdot \hat{n}) = 0$. A perturbation of corner point 4 by -h is required to maintain the boundary condition on panel 2, and so on down the line. Thus the effect of the flow anomaly on panel 1 is propagated to the whole free sheet with the consequence that all the quadrilateral panels become considerably twisted.

Probably the simplest method of damping with instability whenever it arises is to limit excessive panel twist. A measure of panel twist is the function

$$K = \frac{\vec{n} \cdot \vec{Q}_{st}}{(\vec{n} \cdot \vec{n})^{3/4}} \tag{35}$$

where $\vec{n} = \vec{Q}_s \otimes \vec{Q}_t$. The condition that all free sheet panels be untwisted (flat) is

$$K(\Theta) = 0 \tag{36}$$

using the notation of equations (26) and (27). Equation (36) combined with equations (26) and (27) creates an overdetermined system of equations for Λ and Θ. View equation (26) as an equation which defines Λ as function of Θ, i.e.,

$$F(\Lambda, \Theta) = 0 \Rightarrow \Lambda = f(\Theta) \tag{37}$$

Substituting equation (37) into equation (27) results in having two competing equation sets for determining Θ, i.e.,

$$G(f(\Theta), \Theta) = 0 \quad \text{and} \quad K(\Theta) = 0 \tag{38}$$

This system is solved in a least square sense after suitable normalization to account for dimensional differences as well as desired weighting. Obviously the penalty equation (36) should not be weighted too heavily since a free sheet made up entirely of untwisted panels cannot in general be a good approximation to a stream surface. Fortunately a small weight is all that is required. The instabilities produced by a local flow anomaly are severe enough that a very small penalty on panel twist forces

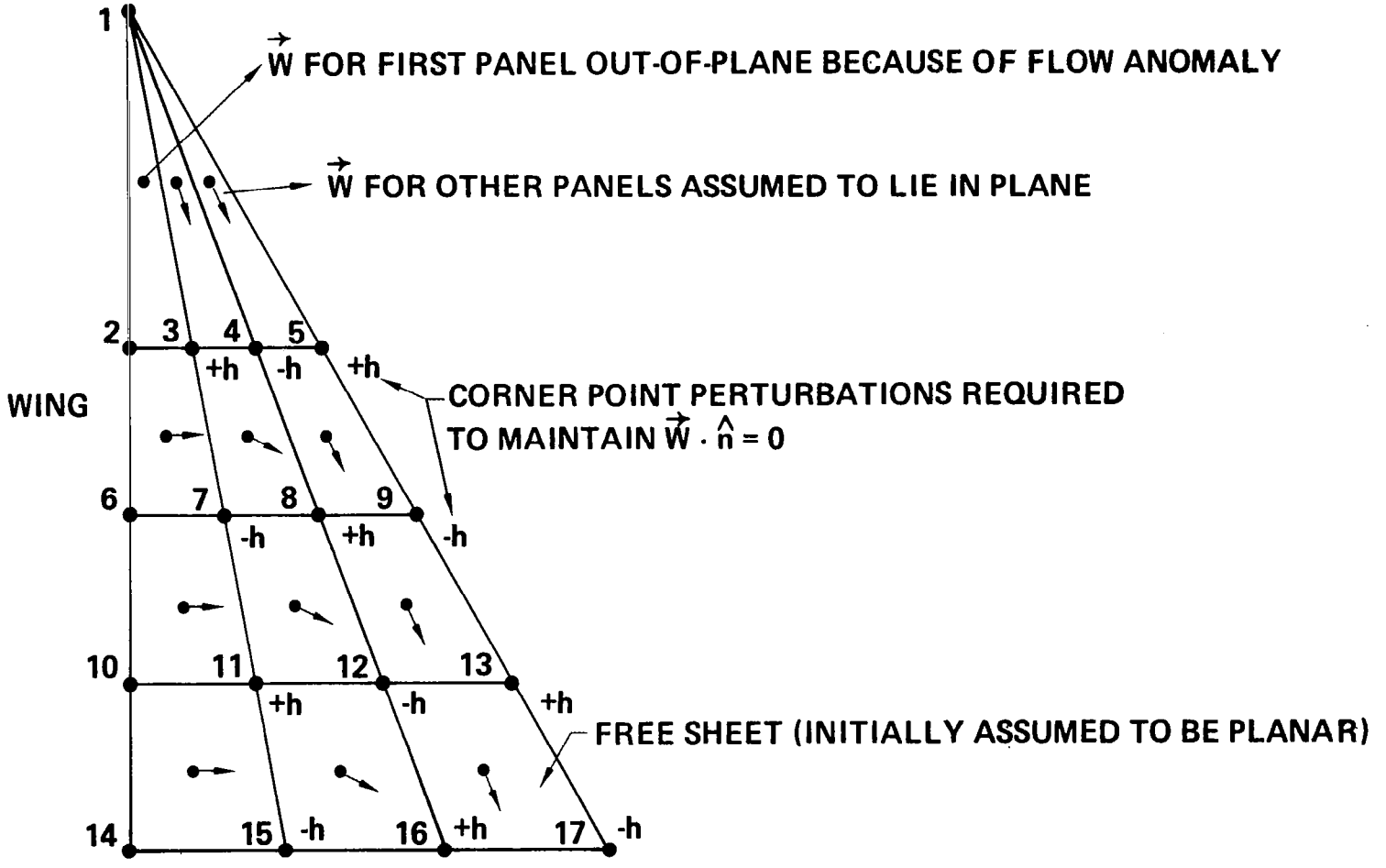

FIGURE 10 GEOMETRY UPDATE INSTABILITY

relaxation of the boundary condition causing the local anomaly.

The procedure for solving the overdetermined equation set is iterative as before. At the beginning of an iteration equation (26) is solved for Λ as a function of the current Θ using Newton's method with controlled step size, i.e.,

$$\frac{\partial F}{\partial \Lambda} \quad \Delta\Lambda = -\rho F \tag{39}$$

where ρ represents symbolically a step size scaling parameter which is a positive number less than 1 and is chosen small enough to ensure a decrease in the norm of F (see equations G.9 and G.11 of Appendix G). Upon obtaining convergence a new estimate for Θ is calculated by solving the equation

$$\begin{pmatrix} \frac{\partial G}{\partial \Lambda} & \frac{\partial f}{\partial \Theta} + \frac{\partial G}{\partial \Theta} \\ & \frac{\partial K}{\partial \Theta} \end{pmatrix} \begin{pmatrix} \Delta \Theta \end{pmatrix} = -\rho \begin{pmatrix} G \\ K \end{pmatrix} \tag{40}$$

in a least square sense, where the Jacobian on the left is evaluated at the point $\Lambda = f(\Theta)$ as determined from (39) and $\frac{\partial f}{\partial \Theta}$ is calculated from

$$\frac{\partial F}{\partial \Lambda} \quad \frac{\partial f}{\partial \Theta} + \frac{\partial F}{\partial \Theta} = 0 \tag{41}$$

It is assumed here that G and K have been normalized appropriately. Again, ρ represents a step size scaling parameter which is a positive number less than 1 and is chosen small enough to ensure a decrease in the norms of G and K (see Appendix G).

6.0 NUMERICAL VERIFICATION

In this section cases generated by the computer program implementing the current method are presented. The purpose of these cases is to display those numerical characteristics of the method which are important for establishing confidence in the computed results.

6.1 Effect of Wing Panel Density

In Figure 11, the effect of wing panel density on vortex system geometry, wing pressures, and forces and moments is shown. The primary effect is associated with spanwise density. In Figure 11a two conically paneled wings having 6 and 12 panels spanwise are illustrated. In both panelings the spacing is non-uniform with a concentration of panels where they are obviously most required, namely outboard under the vortex. The effect of an increase in density is to move the vortex system slightly outboard as shown in Figure 11b, and the consequence is somewhat higher pressures on the upper surface outboard of the vortex core as shown in Figure 11c. The lift coefficient is correspondingly higher (see also Figure 19b). Greater spanwise densities have been run but the incremental effect is negligible compared with that shown in Figure 11.

6.2 Effect of Wing Panel Layout

In Figure 12 computed results for the two panel layouts usually employed on delta wings, i.e., streamwise and conical are compared. Both layouts have 64 panels. The least square procedure described in section 5.2 was required to obtain convergence for the streamwise paneling. Wing pressures and force and moment coefficients are displayed in Figure 12b. Pressures for the streamwise paneling have been interpolated to the control point locations of the conical paneling for comparison purposes. The two cases were run about a year apart and in the intevening time a study on initial sheet shape was made, hence the free sheets have somewhat different panel spacing. However comparisons of pressure and force data still show excellent agreement.

6.3 Effect of Vortex Sheet Rollup

The cornerstone of the current method is, of course, Smith's device for terminating the free sheet rollup, namely the use of a fed sheet whose position and size are determined by the same overall force condition that would be applicable to an infinitely rolled up free sheet. The point at which the free sheet rollup should be terminated by a fed sheet depends upon the sensitivity of wing pressures to further rollup. This matter has been investigated in detail by Smith (ref. 6) under the assumption of conical flow, and the standard amount of rollup employed by the current method is based on his results. To verify the application to fully three-dimensional flow, delta wings of aspect ratio .25, 1.0 and 2.0 have been analyzed with an additional 180° of rollup. Results at AR = 0.25 are shown in Figure 13 and indicate a slight increase in lift (4 percent) with increased rollup. The effect of rollup is much less at the higher

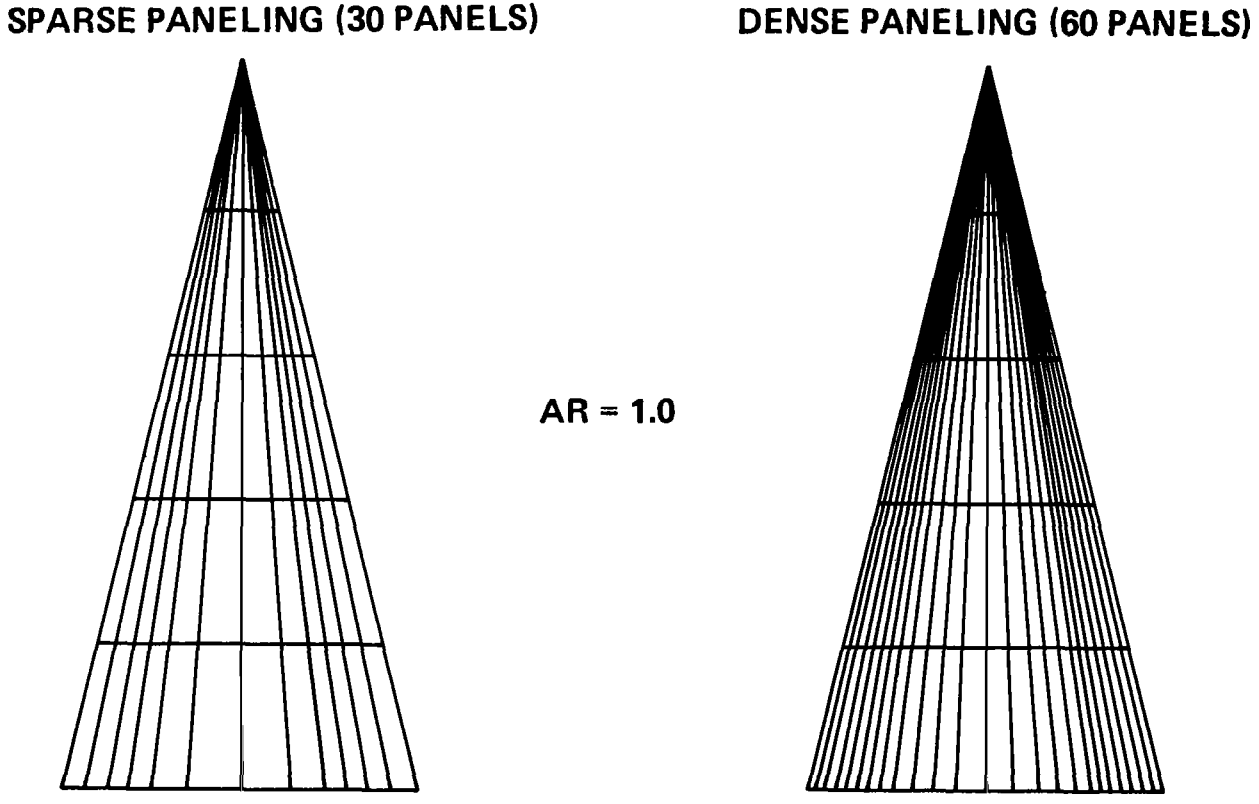

a. WING PANELING

FIGURE 11 EFFECT OF WING PANEL DENSITY

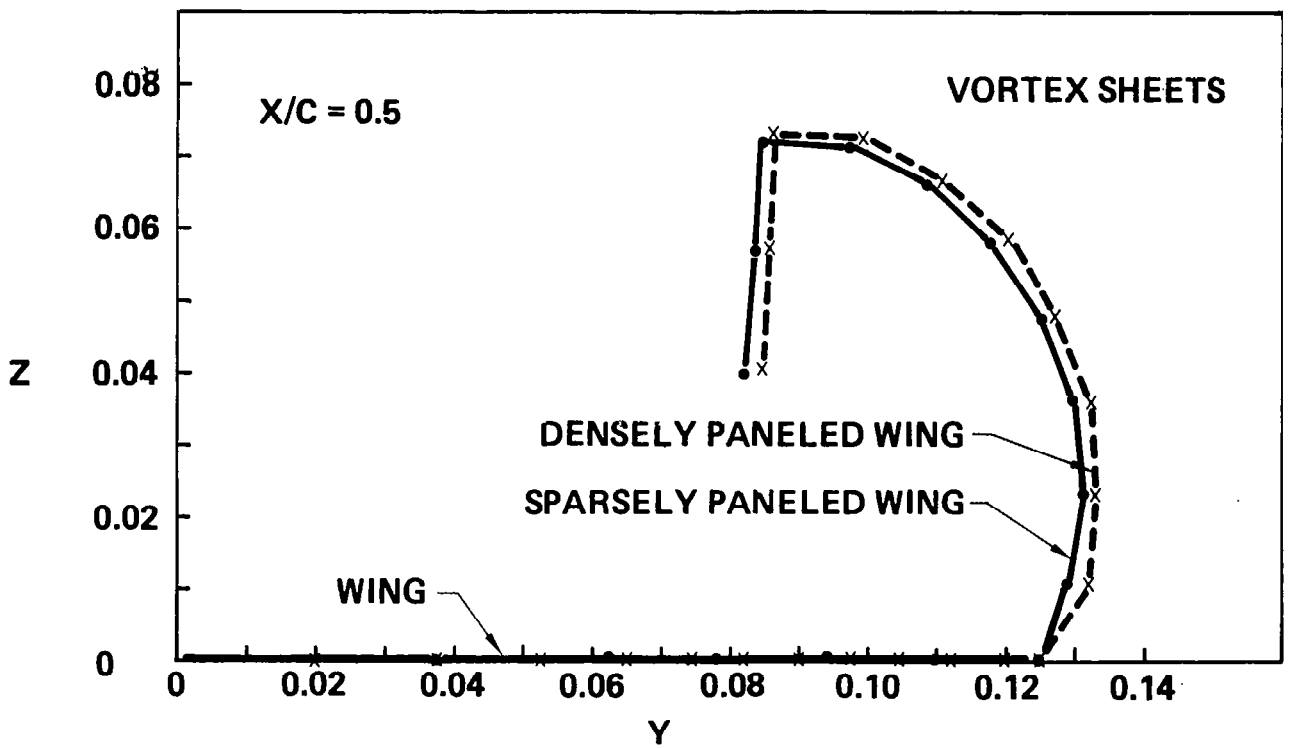

b. VORTEX SYSTEM GEOMETRY

FIGURE 11 CONTINUED

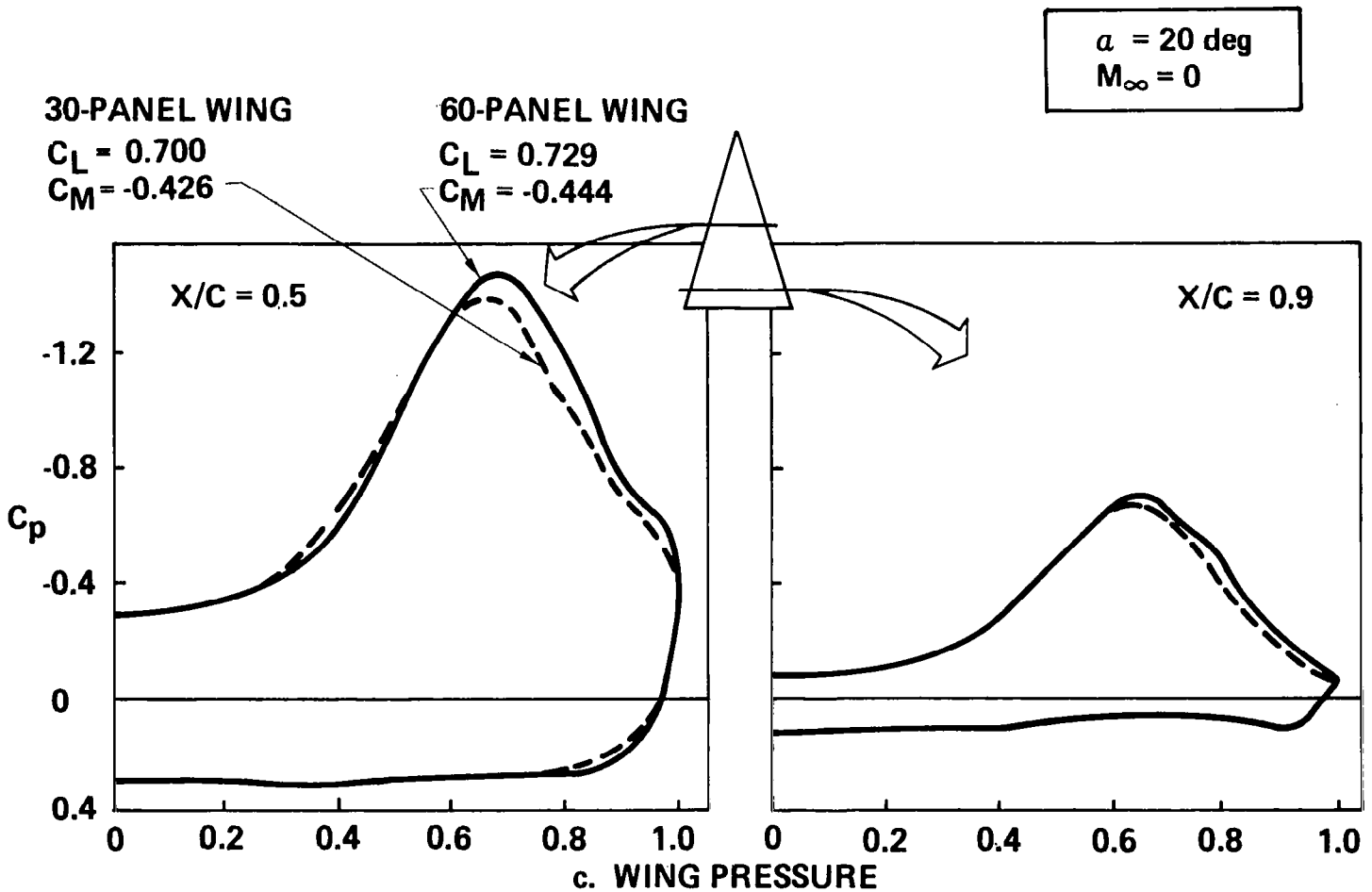

FIGURE 11 CONCLUDED

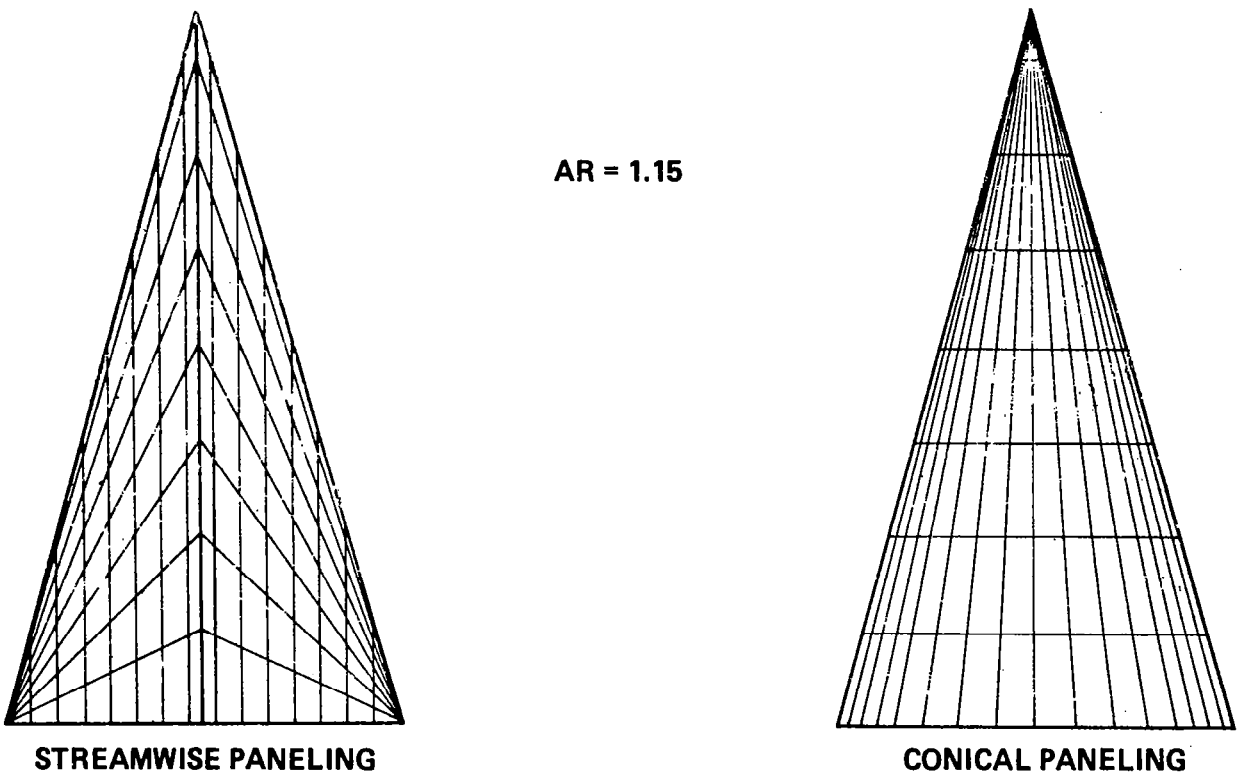

a. WING PANELING

FIGURE 12 EFFECT OF WING PANEL LAYOUT

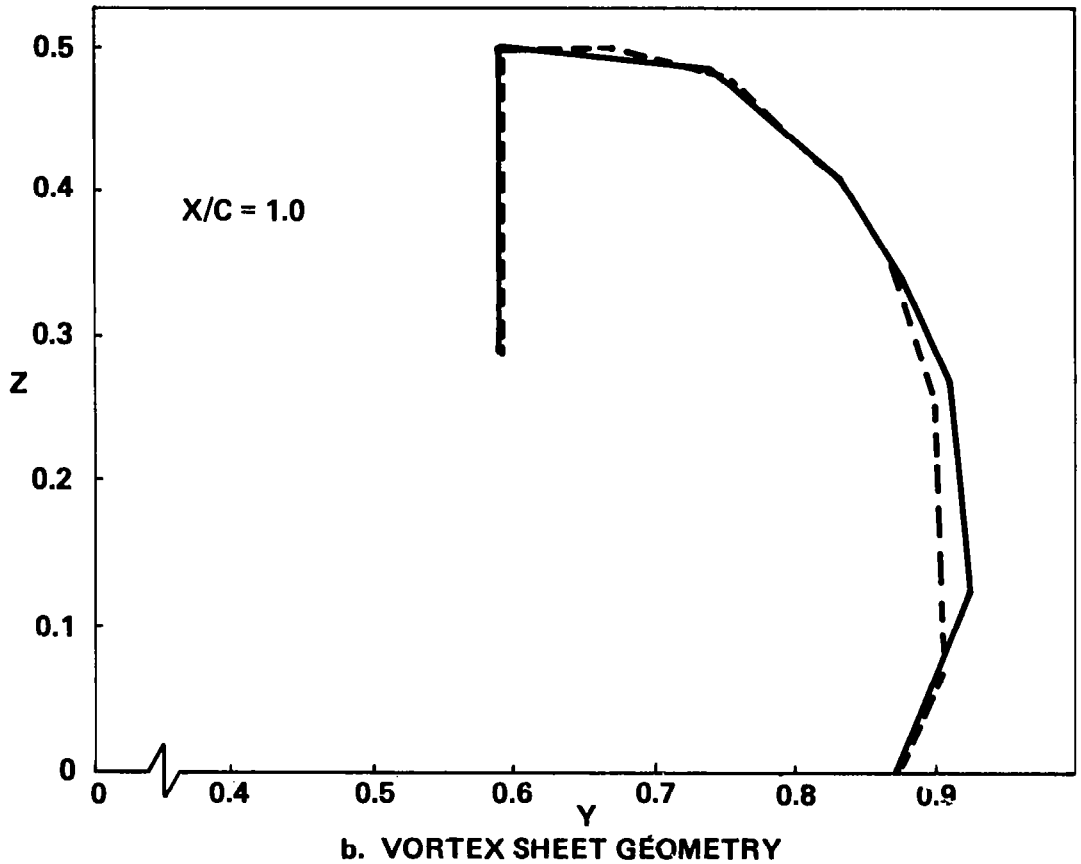

b. VORTEX SHEET GEOMETRY

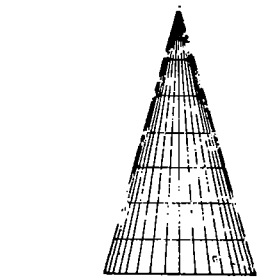

CONICAL PANELING

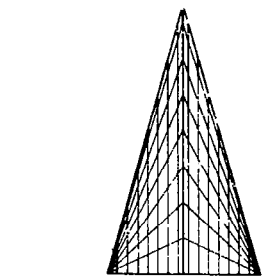

STREAMWISE PANELING

FIGURE 12 CONTINUED

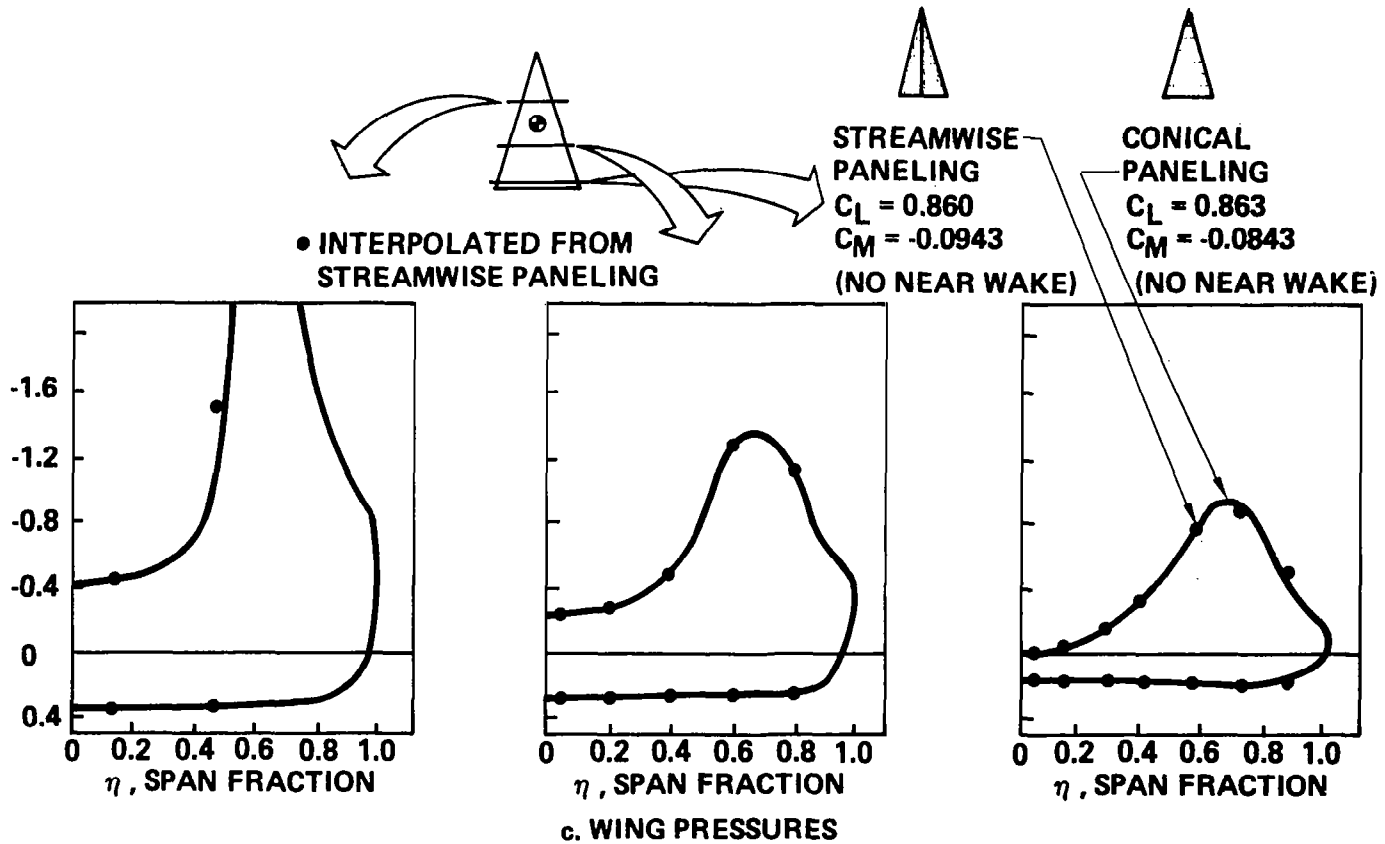

c. WING PRESSURES

FIGURE 12 CONCLUDED

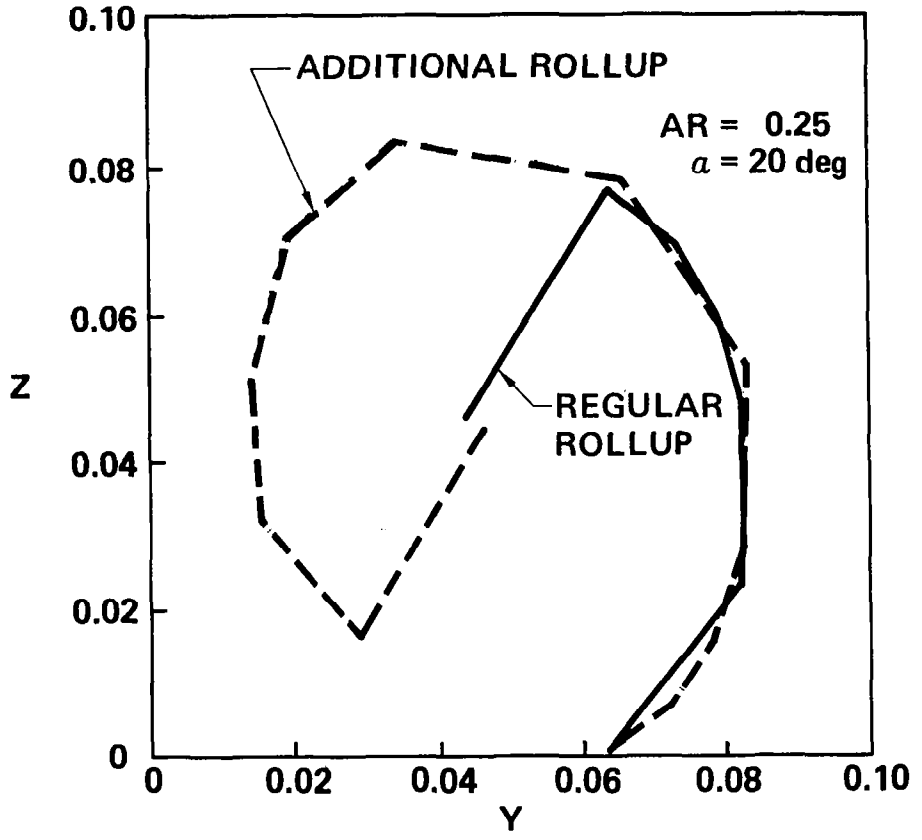

a. VORTEX SHEET GEOMETRY

FIGURE 13 AR = 0.25 DELTA WING WITH ADDITIONAL FREE SHEET ROLLUP

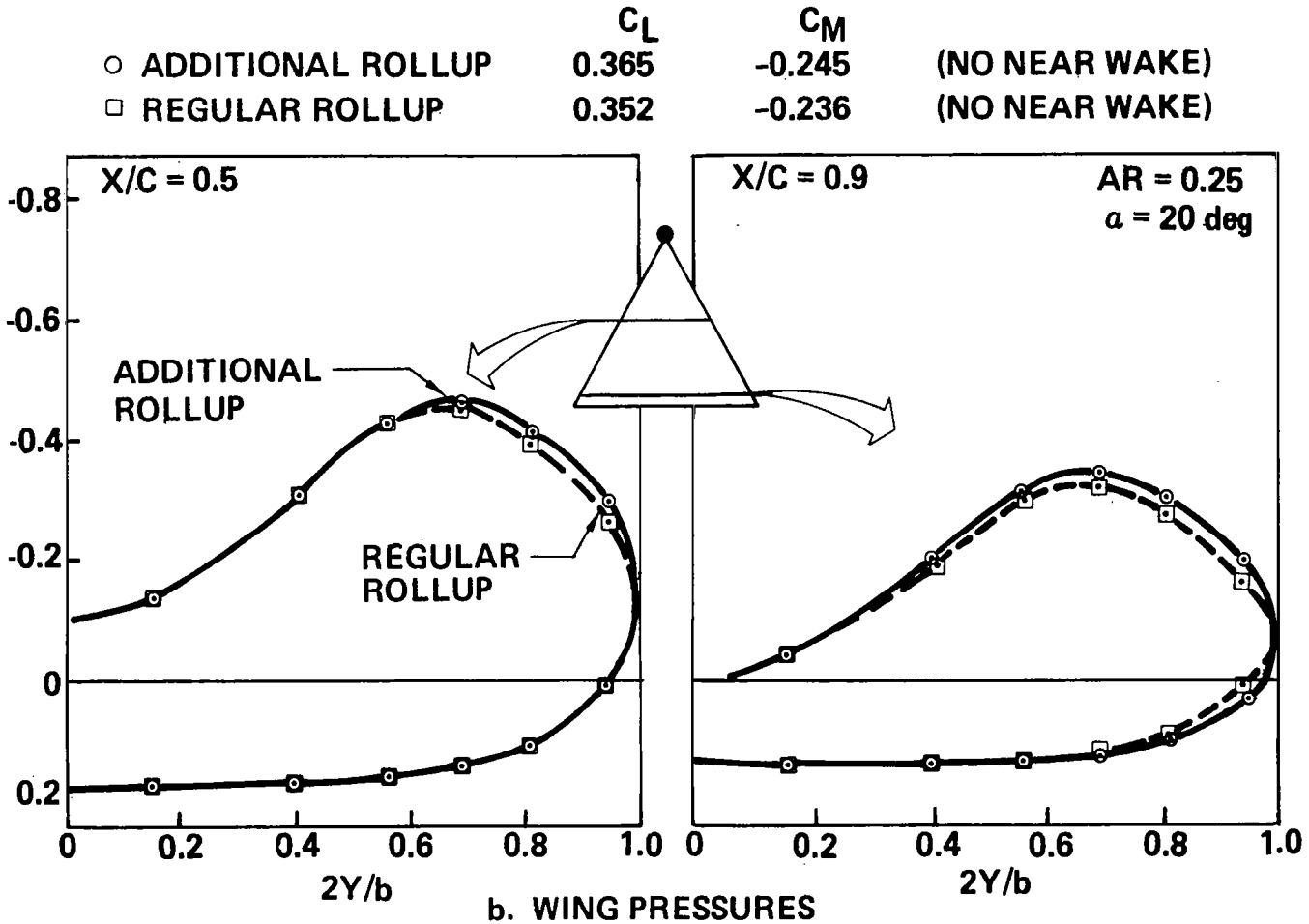

b. WING PRESSURES

FIGURE 13 CONCLUDED

aspect ratios (1 percent at AR = 1.0 and less than 0.5 percent at AR = 2.0). Results for AR = 2.0 are shown in Figure 14. The conclusion is that the standard rollup is generally adequate for all models. The slight improvements available at low aspect ratios do not seem to warrant the added complexity and expense of additional rollup.

6.4 Effect of Vortex System Kinematics

The current standard vortex system kinematics shown in Figure 6 is, of course, only one of many possibilities. A good alternative is the kinematics of Smith (ref. 6) shown in Figure 15. Here, in contrast to the standard kinematics, angles are fixed and lengths are chosen as free parameters. Smith's kinematics has also been coded into the computer program implementing the current method with results typified in Figure 16. Comparisons have been made for small and large free sheet rollups, for core locations inboard and in the vicinity of the leading edge, and for wings of small and large aspect ratio, all with similarly close results. If any difference has been noticed, it is that Smith's kinematics seems to converge somewhat faster than the current standard kinematics with corresponding savings in run cost.

6.5. Kutta Condition

In section 4.3 the manner in which the current method enforces the Kutta condition at a wing edge was described. It was pointed out that the equation formally assigned as the Kutta condition is actually a restriction on singularity strength rather than the flow, namely that the component of vorticity parallel to the wing edge be continuous onto the vortex sheet. This condition when combined with the standard flow boundary conditions assigned to the interior of the wing and free sheet then creates those properties at the edge commonly associated with the Kutta condition, i.e., finite flow, zero pressure jump, etc. It was also pointed out that finite flow requires continuity of all components of the vorticity vector across the edge, which can only happen when the wing and free sheet adjoin smoothly. This fact seems somewhat inconsistent with our converged vortex system geometry (e.g. Figure 11b) which usually displays a large discontinuity in surface shape at the wing-sheet junction. However the discontinuity in surface slope is qualitatively no different than any other on the vortex system and can be reduced (and in the limit eliminated) by dense paneling. In Figure 17 the effects of finer vortex sheet paneling at the wing junction are shown. Note that the discontinuity in surface slope at the junction is considerably reduced. To reduce the discontinuity in surface slope in the neighborhood of the junction to the point where the surface would appear smooth to plotting accuracy would require extremely fine paneling at enormous expense. Fortunately such paneling is not required unless precise details of the flow in the neighborhood of the junction are required for reasons other than establishing the Kutta condition. This is because the global effects of the Kutta condition are already accounted for by our particular implementation. Note from figure 16b that dense free sheet paneling near the junction has little effect on lift and moment coefficients, vortex core position and strength, and pressure distributions except at the junction.

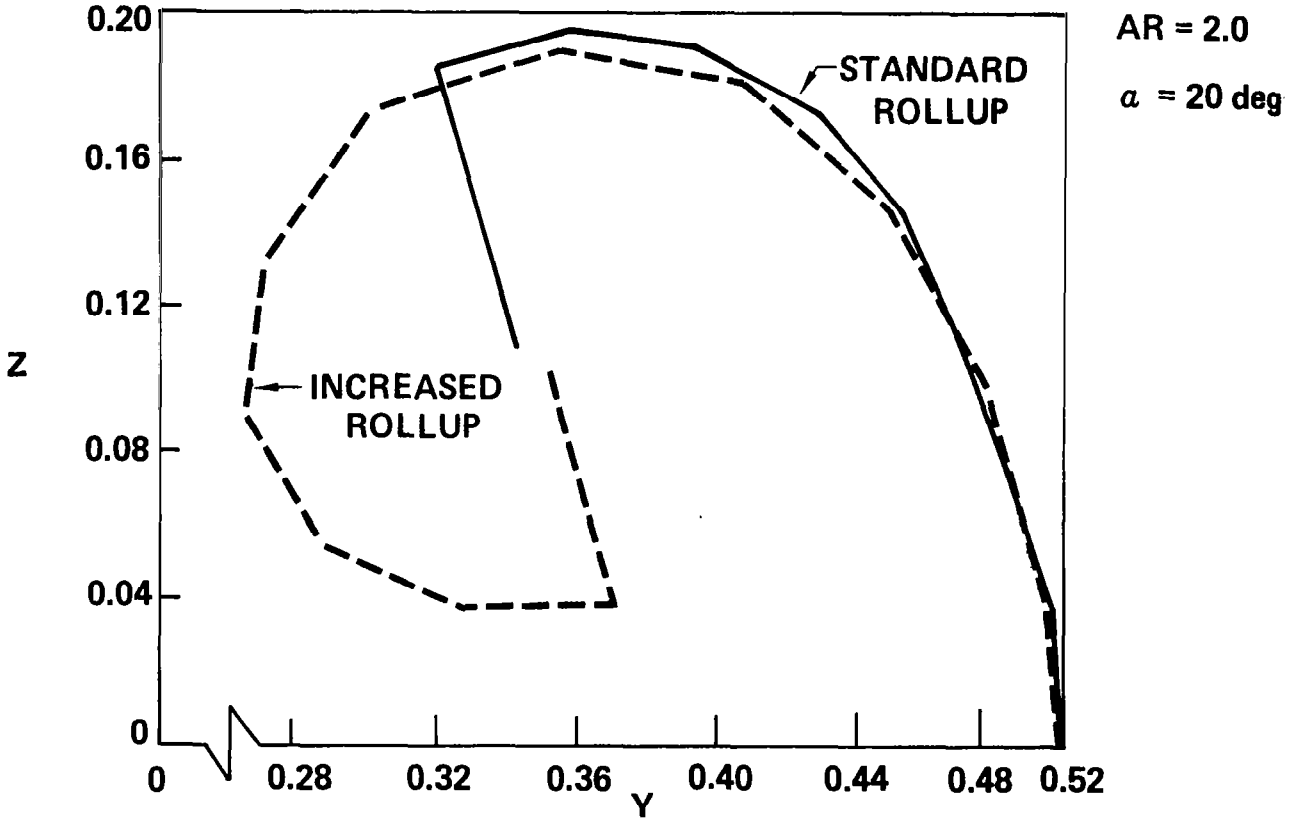

a. VORTEX SYSTEM GEOMETRY

FIGURE 14 AR = 2.0 DELTA WING WITH ADDITIONAL FREE SHEET ROLLUP

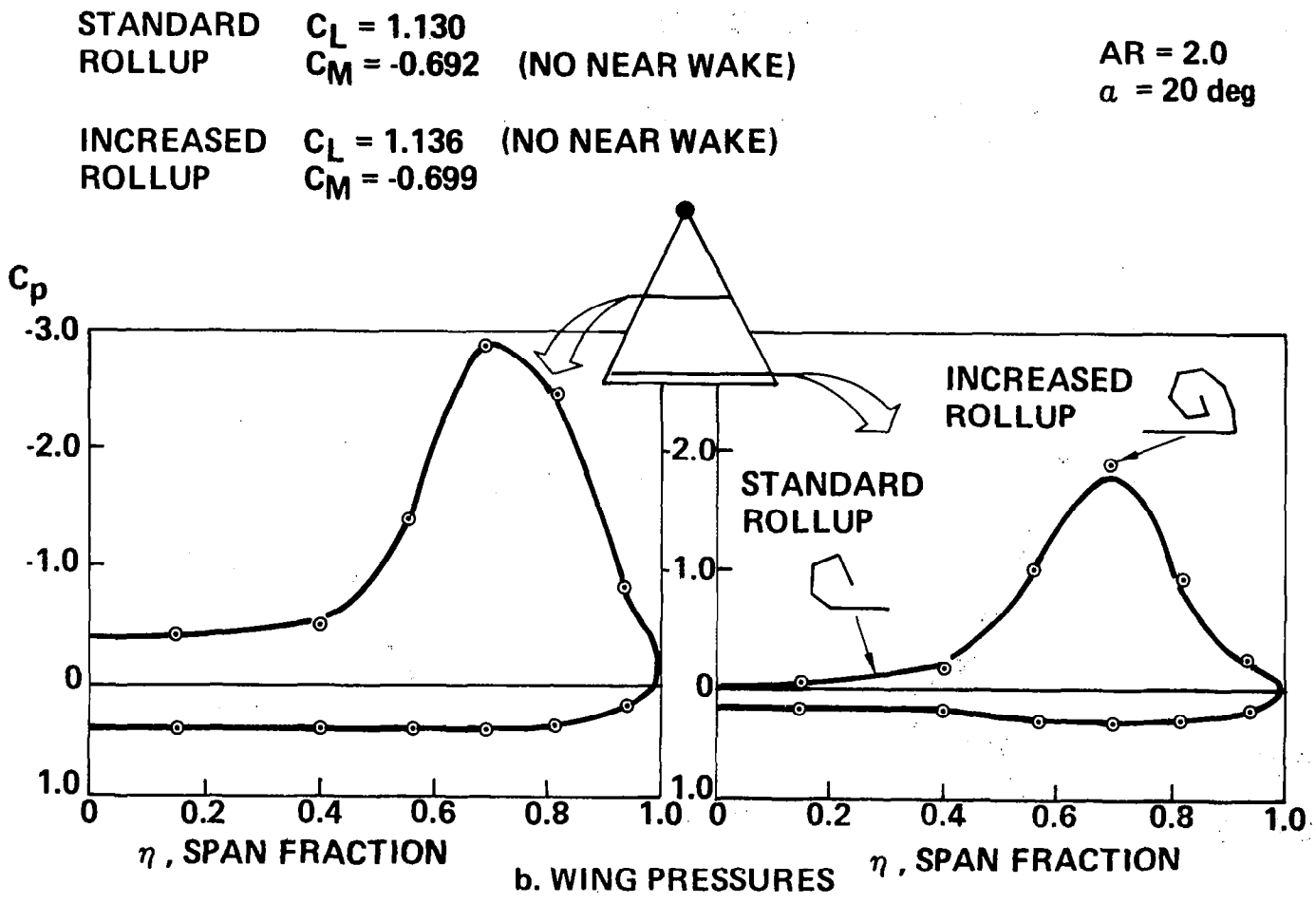

FIGURE 14 CONCLUDED

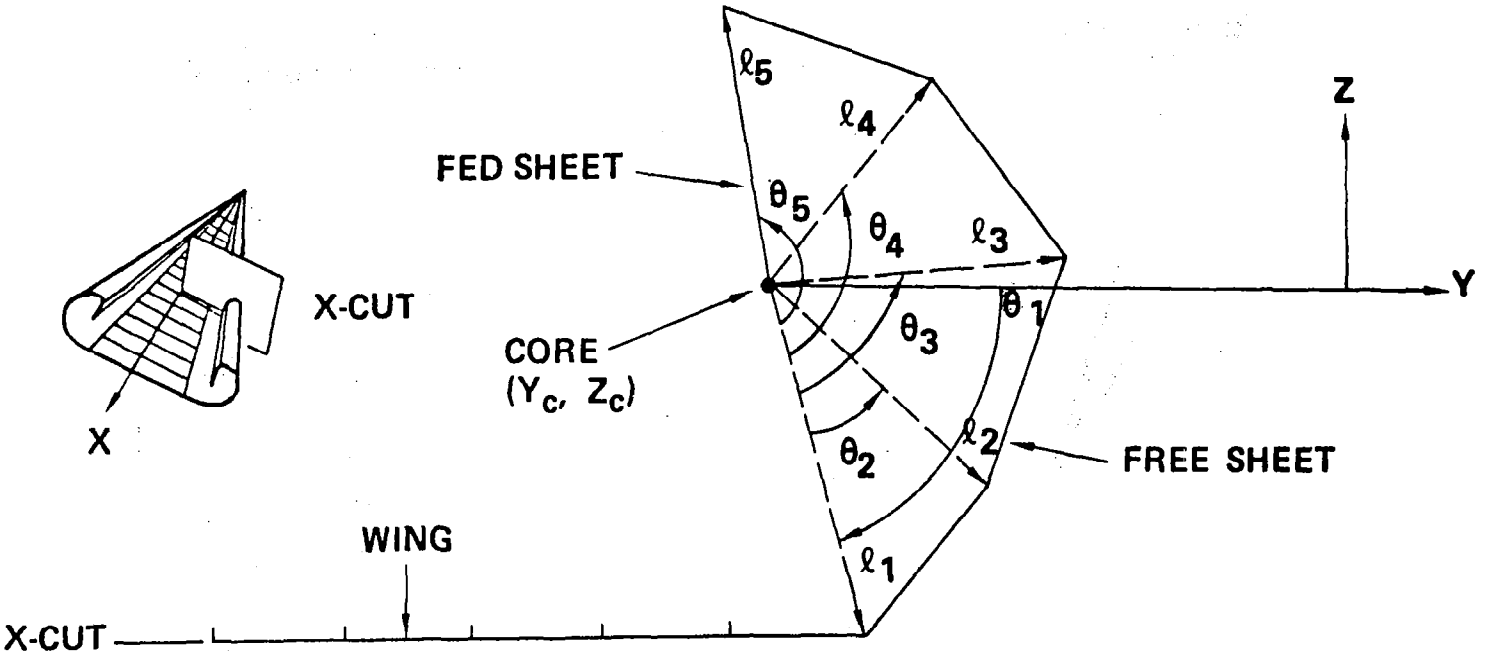

FREE PARAMETERS: ℓ_2, ℓ_3, ℓ_4, ℓ_5, Y_c, Z_c

FIXED PARAMETERS: θ_2, θ_3, θ_4, θ_5

FIGURE 15 SMITH'S FREE/FED SHEET KINEMATICS

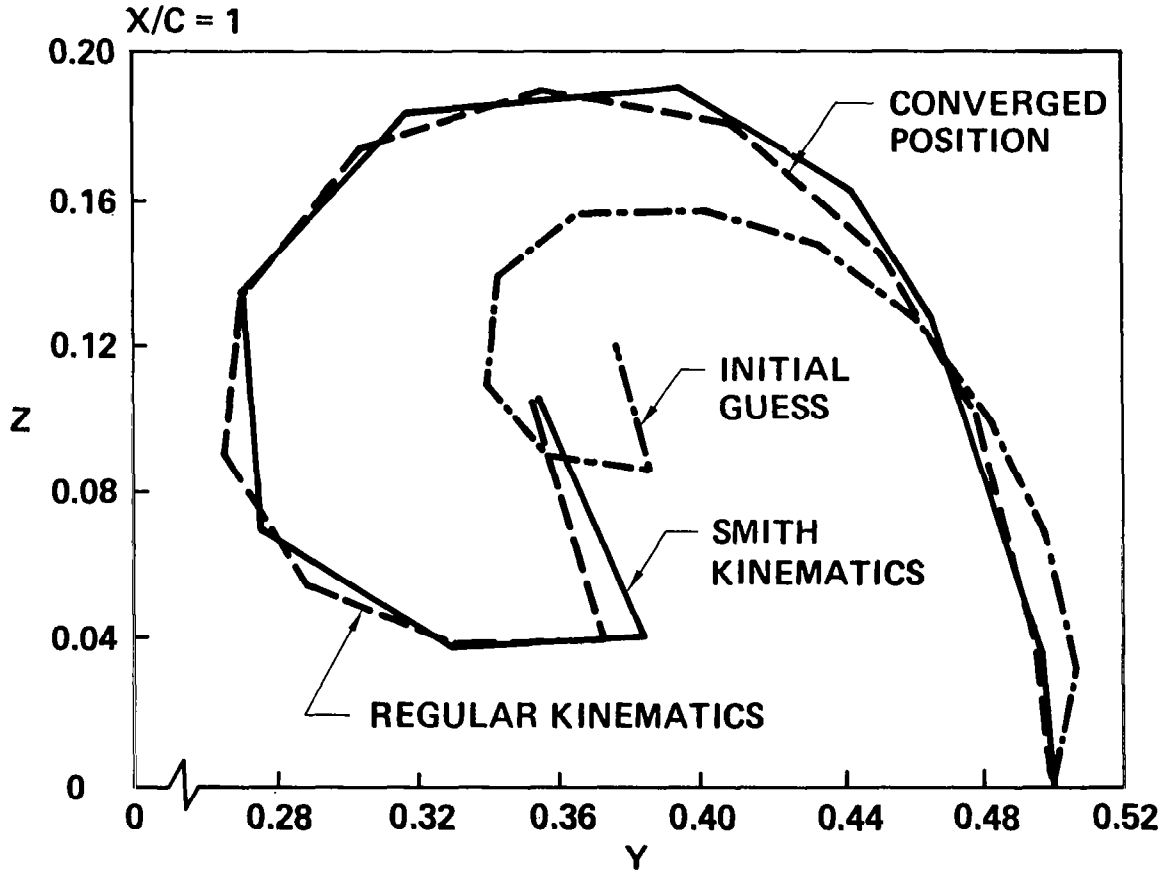

a. VORTEX SYSTEM GEOMETRY

FIGURE 16 EFFECT OF VORTEX SYSTEM KINEMATICAL ASSUMPTIONS

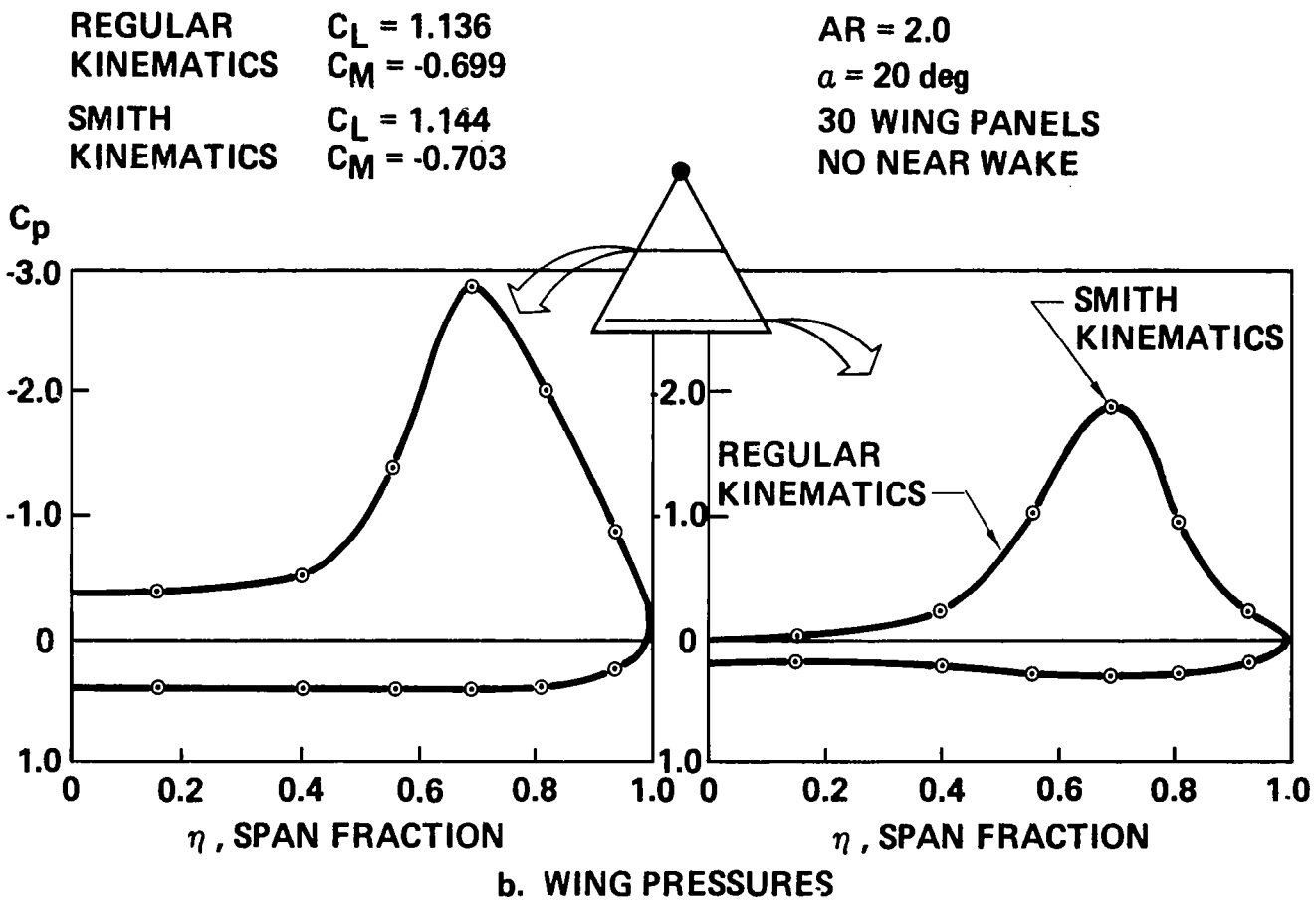

b. WING PRESSURES

FIGURE 16 CONCLUDED

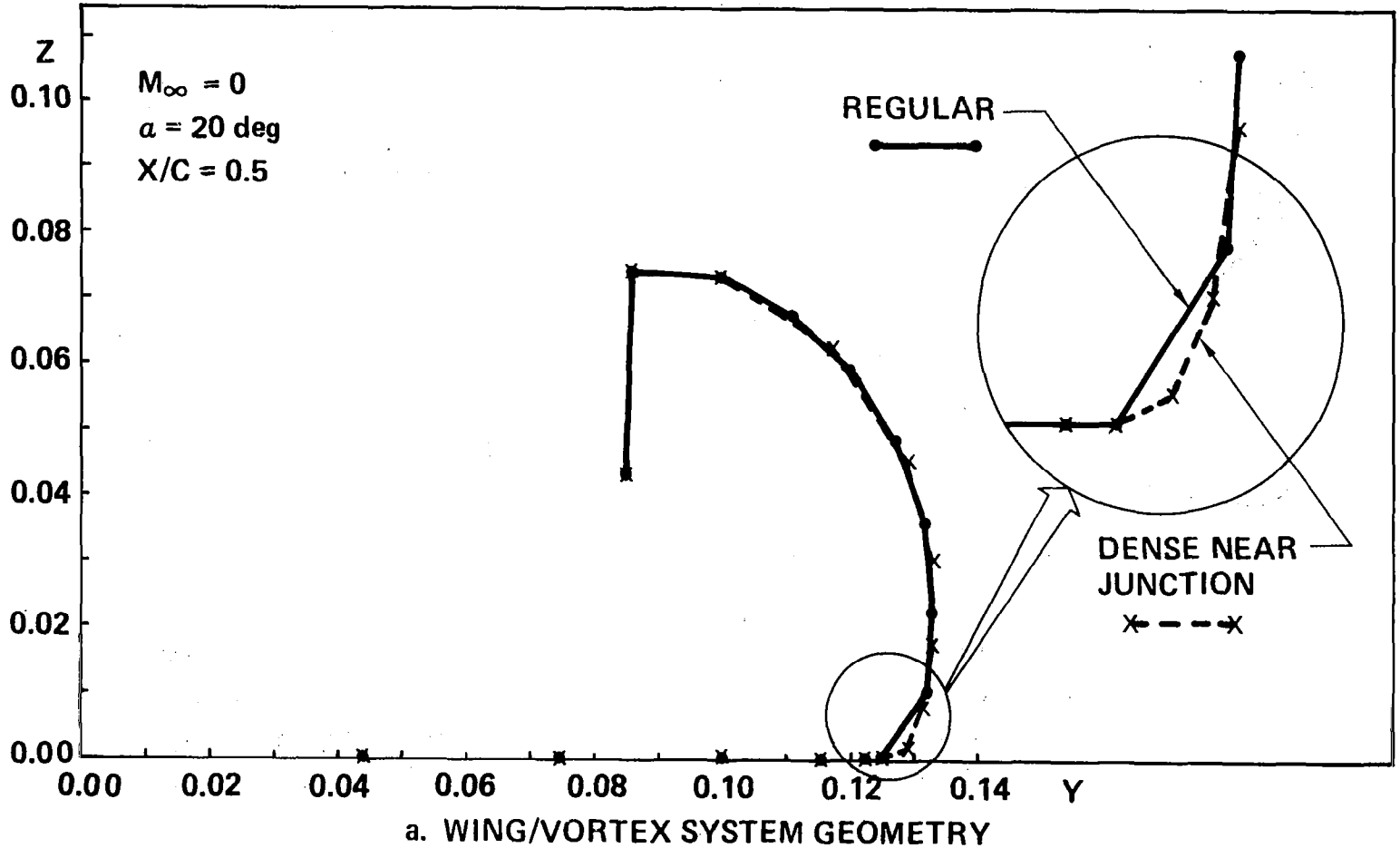

a. WING/VORTEX SYSTEM GEOMETRY

FIGURE 17. KUTTA CONDITION

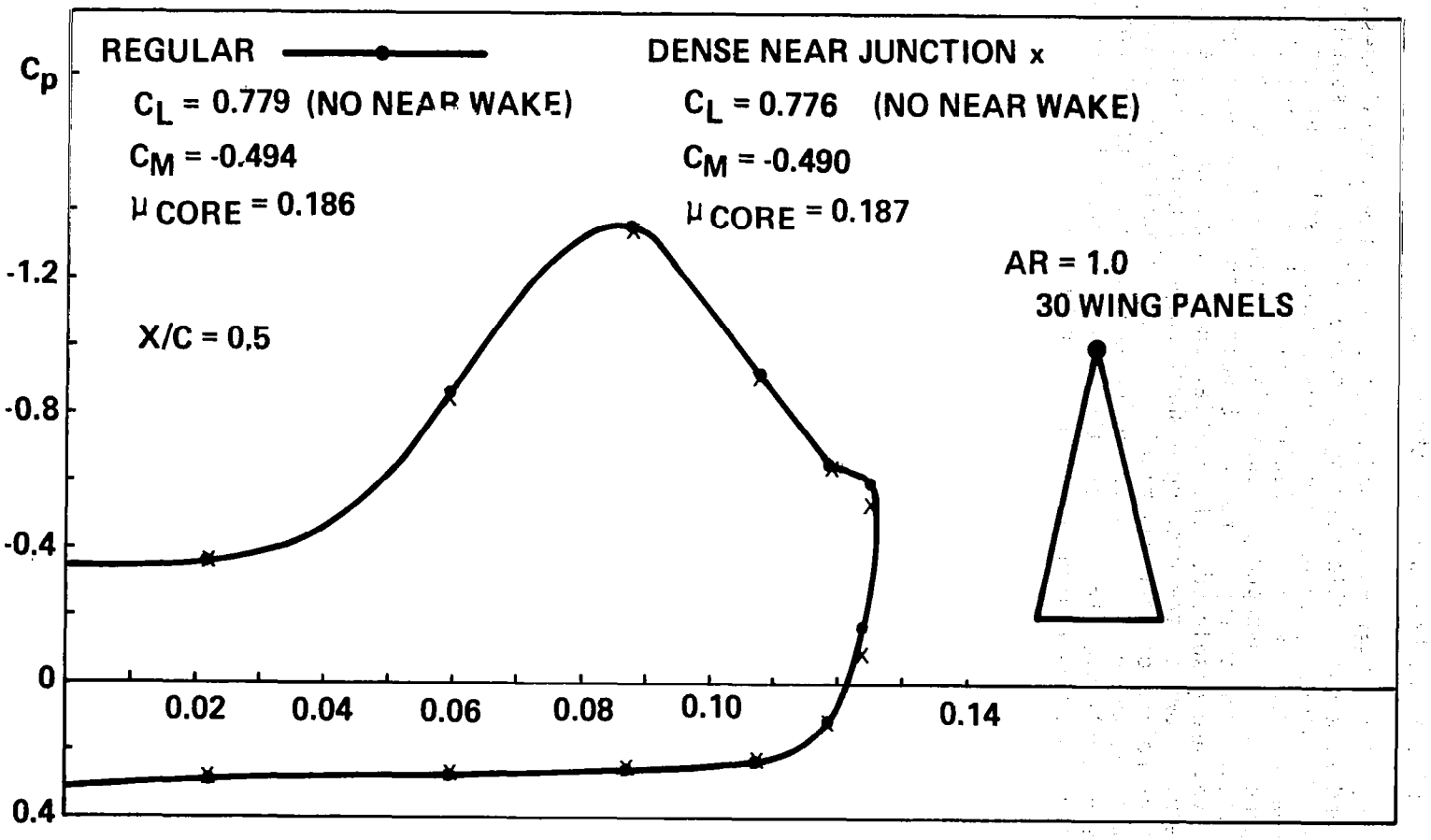

b. WING PRESSURE

FIGURE 17 CONCLUDED

6.6 Effect of Initial Free and Fed Sheet Shape

Aside from free sheet rollup and panel density the initial guess of sheet shape and size has little bearing on converged results (assuming, of course, the boundary value problem has a unique solution) although convergence itself will be affected. Figure 18 illustrates this point. In Figure 18b a converged pressure distribution and force and moment coefficients for an aspect ratio .25 delta wing at 20^{o} angle of attack and no yaw are displayed. The initial sheet shape is considerably asymmetric, however the converged sheet shape is quite symmetric given the fact that rollup on left and right sides are slightly different. More importantly, the pressure distribution and force and moment coefficients are very nearly symmetric. Note the close agreement in values with the solution employing a plane of symmetry in Figure 13.

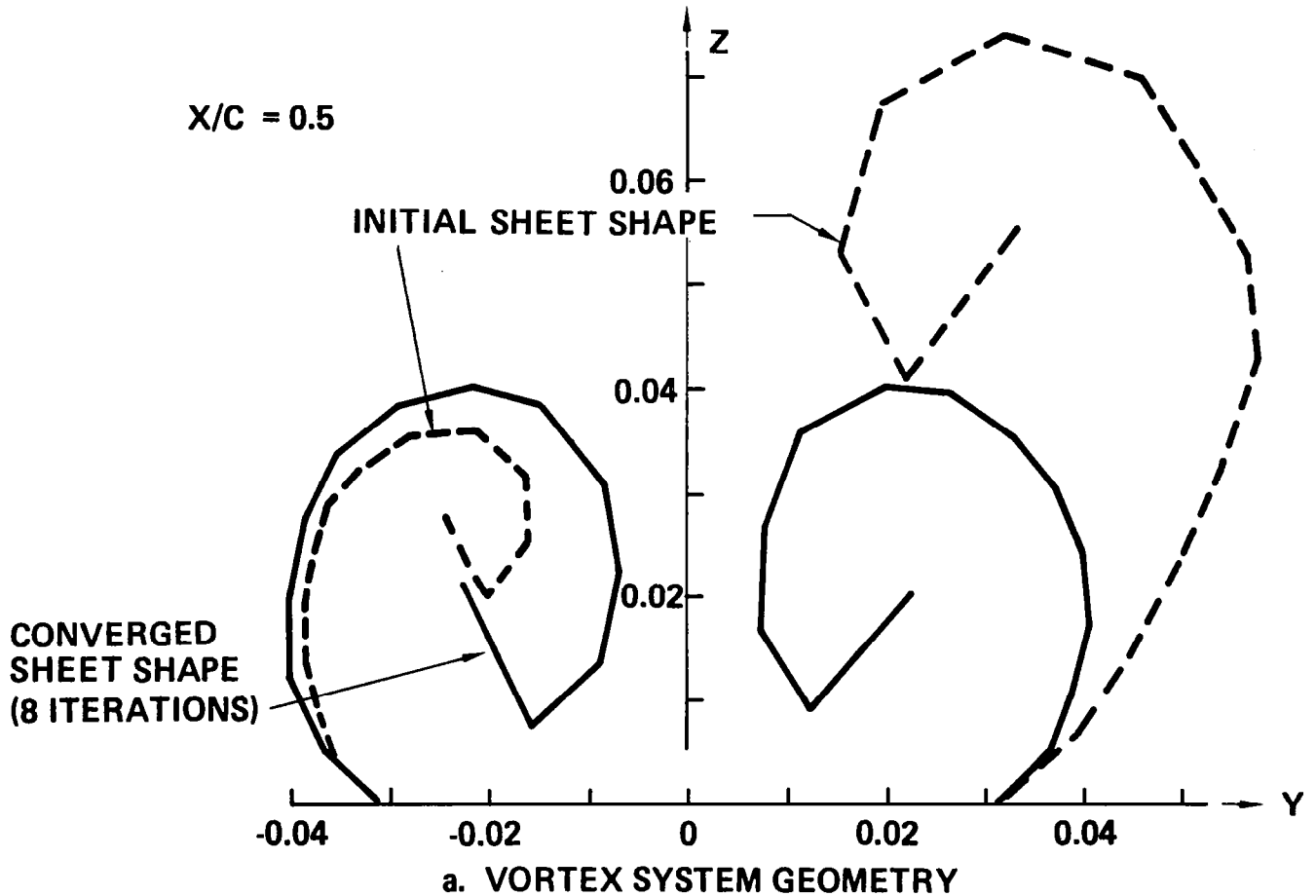

FIGURE 18 ASYMMETRIC INITIAL SHEET SHAPE

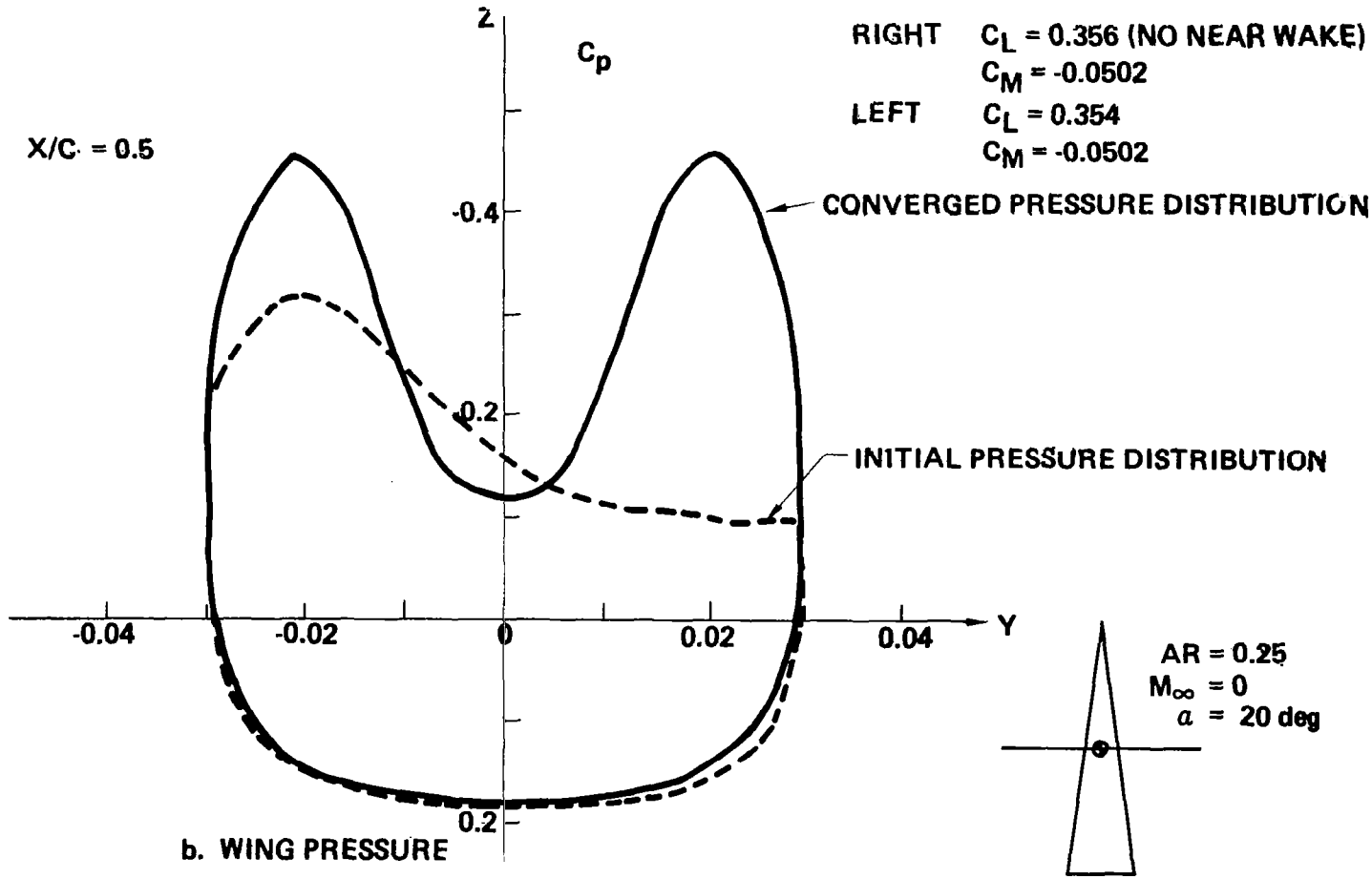

b. WING PRESSURE

FIGURE 18 CONCLUDED

7.0 COMPARISONS WITH EXPERIMENT AND OTHER THEORIES

In this section we present computed results for the purpose of examining the validity of the theoretical model described in section 2.1. Many such results have been reported previously in References 15, 18, 26. Results presented here will be those that are primarily new in nature, although some previously presented results will be repeated for the sake of completeness. Particular note should be taken of reference 26 in which the capabilities of the method in analyzing cambered wings are illustrated.

7.1 Delta Wings

7.1.1 Lift Coefficients as a Function of Aspect Ratio

In section 2.2 the problem associated with the method overpredicting lift coefficient at high aspect ratio, and how this problem was eliminated by use of the more accurate near wake (type 6, Figure 3) at the wing trailing edge was discussed. Resolution of the problem is shown in Figure 19. The dashed line in Figure 19b shows the lift coefficients calculated using a far wake (type 8) only. (Results using 60 wing panels would be somewhat higher at the high aspect ratios). Insertion of near wake (shown in Figure 19a) yields lift coefficients which are in substantially better agreement with the suction analogy and experiment (refs. 2, 27, 28, 29, 30) at the higher aspect ratios. These lift coefficients are based on a near wake of 0.5 root wing chord in length divided into three rows of panels. (Note that the free/fed sheet vortex system must extend to the end of the near wake.) In order to study the sensitivity of the wing pressures to near wake length, two additional near wakes were tested. One was 1.5 root chords long and made up of 5 rows of panels (Fig. 19a). The other was 0.1 root chords and made up of 2 rows of panels. Wing pressures for all three wakes were practically identical indicating, as stated in section 4.3, that the primary function of this wake is to establish the proper wing trailing edge Kutta condition.

The question of lack of agreement between the suction analogy, experiment and the current method at very low (0.5,) or high (.1.5) aspect ratios still remains. Examination of the results shows that for a very low (0.25) aspect ratio the experimental data lies nearly half way between the results of the current method (low) and suction analogy (high). However analysis of the experimental (reference 29) data reveals that at the 20° angle of attack shown, an asymetrical vortex has developed in the real flow. This is indicated by the rolling moment at zero yaw that developed at angles of attack greater than about 16°. The theoretical models assume symmetrical vortices. J. M. Luckring (NASA LRC) has computed solutions at several angles of attack using the current method. His results presented in Figure 20 show excellent agreement between the method and experimental data at the lower angles of attack. Beginning with the 15° angle of attack the results start to deviate from the experimental data. Since this is approximately where the leading edge vortices become asymmetrical while the theory vortices remain symmetric, it is conceivable that this phenomenon could somehow be responsible for the deviation.

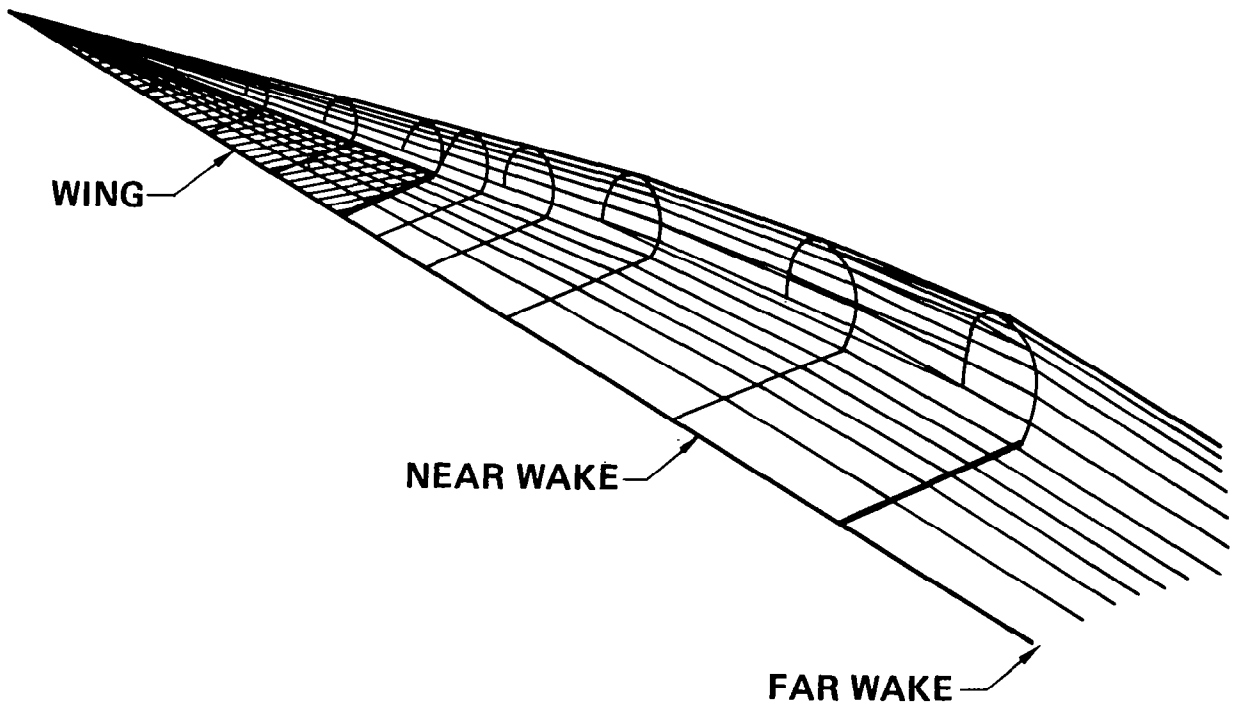

a. WING, VORTEX SYSTEM, AND WAKE GEOMETRY

FIGURE 19 DELTA WINGS WITH NEAR WAKE

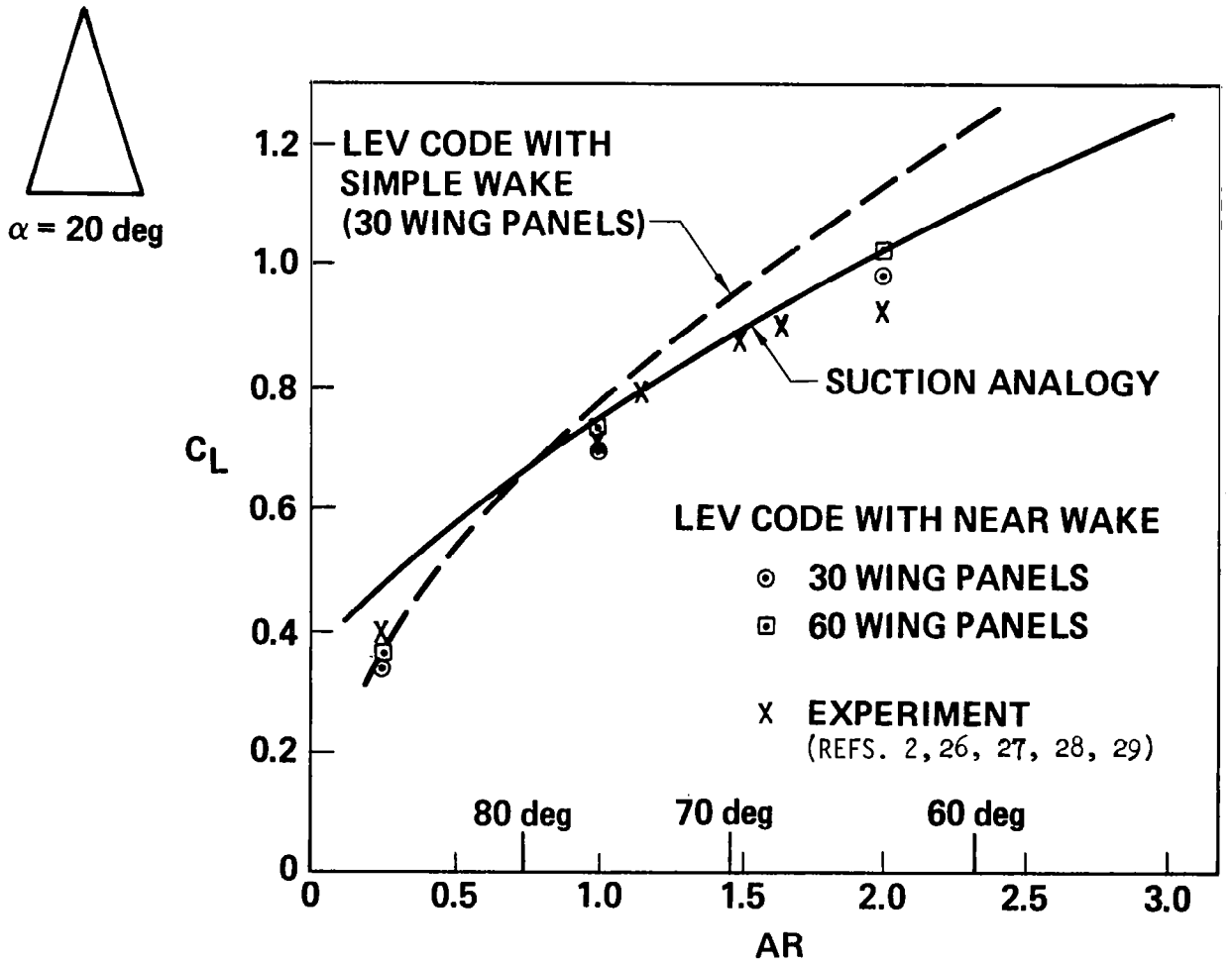

b. VARIATION OF LIFT WITH ASPECT RATIO

FIGURE 19 CONCLUDED

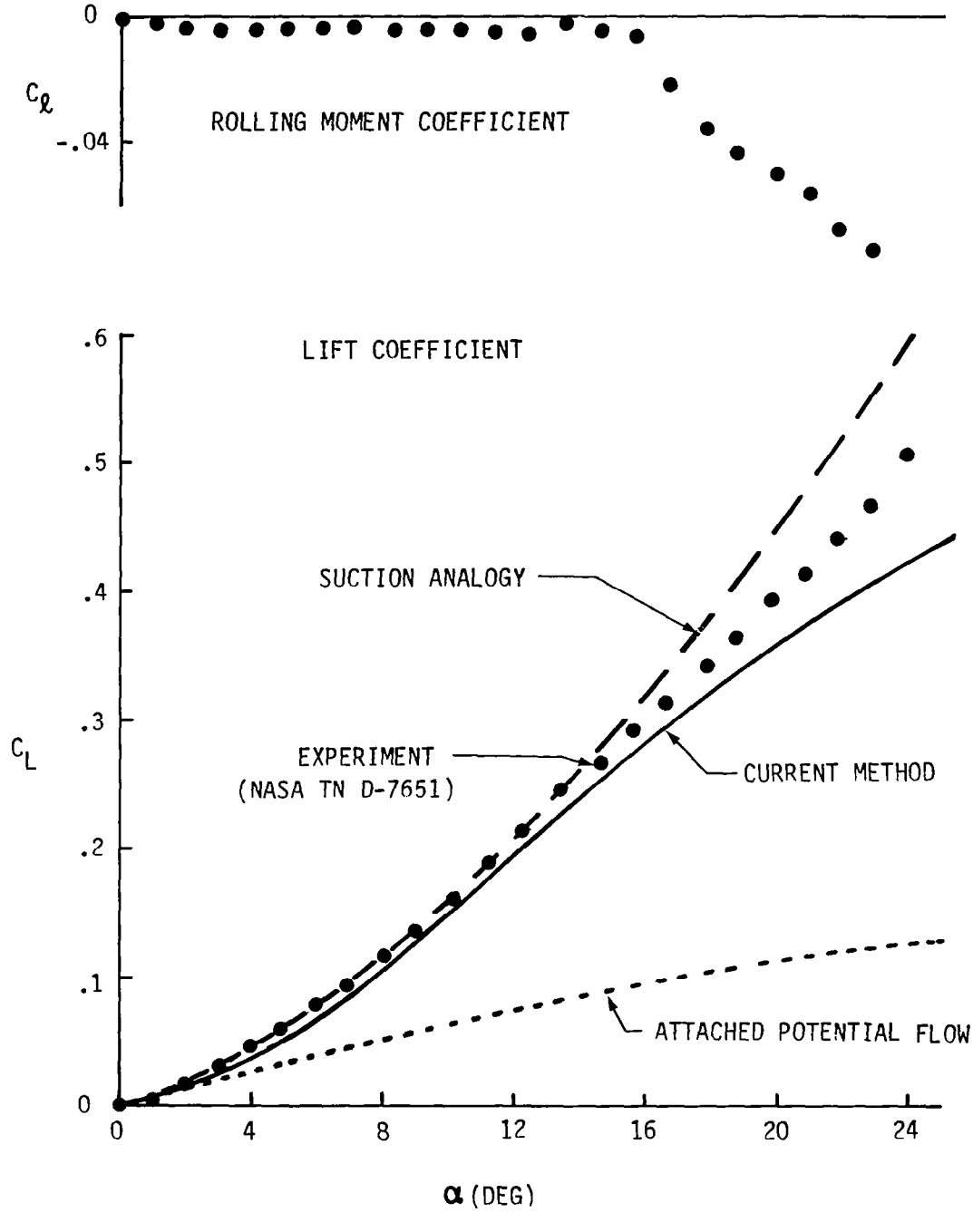

FIGURE 20 AERODYNAMIC CHARACTERISTICS OF ASPECT RATIO 0.25 WING

Suction analogy results are also shown in Figure 20. These results also deviate from experiment at the higher angles of attack but in the opposite manner. E. C. Polhamus (NASA LRC) has suggested that the suction analogy may be high for these cases because the analogy assumes complete reattachment of the leading edge vortex and therefore complete recovery of the suction force. As previously shown in Figure 13 for low aspect ratio deltas at high angles of attack, the size of the free sheet which represents the vortex shear surface has become so large that it may be preventing complete reattachment and therefore complete suction recovery.

At the higher aspect ratios, the current method is in good agreement with the suction analogy but both methods predict higher lift coefficients than shown by the data. Examination of the experimental results shows a loss in lift at the higher angles of attack due to vortex bursting. Since neither the current method nor the suction analogy can account for this phenonema exact correlation with experimental data is not possible.

7.1.2 Pressure Distributions

One of the most important features of the method is its ability to compute surface pressure distributions. This capability sets it apart from most other leading edge vortex methods. A comparison of detailed pressure distributions are shown in Figures 21 and 22. These results were calculated with the earlier version of the method (reference 14). Lifting pressures, shown in Figure 21, on an aspect ratio 1.0 wing are compared with the experimental data of Peckham (reference 2). Although only 25 wing panels were used on one half of the configuration, the completely three-dimensional non-conical load distribution was predicted well including the location of the vortex induced pressure peak and the decrease of the load toward the trailing edge. Figure 21 illustrates the method compared to the experiment of Marsden (Reference 32) for an aspect ratio 1.4559 delta wing at an angle of attack of 14^{o}. The general agreement between the predicted and the measured pressures is quite good. The experimental results clearly show the effect of the secondary vortex separation, which takes place on the upper surface just slightly outboard of the main vortex. The presence of the secondary vortex raises the suctions near the leading edge and lowers the suction peak due to the primary vortex. The theoretical method does not model secondary vortex separation and, consequently, produces a slightly different shape for the pressure peaks. This type of discrepancy will be found in most test-theory comparisons.

The method is also capable of calculating pressures on a wing at yaw as well as at angle of attack. Such calculations require that the complete wing be paneled and that no symmetry conditions be imposed. Figure 23 shows a comparison of calculated lifting pressures with the experimental data of Harvey (Reference 32) on a delta wing with 80 leading edge sweep. The theoretical results clearly predict the asymmetric character of the lifting pressure distribution. The descrepancy due to the presence of the secondary vortex is quite evident in this comparison. Additional

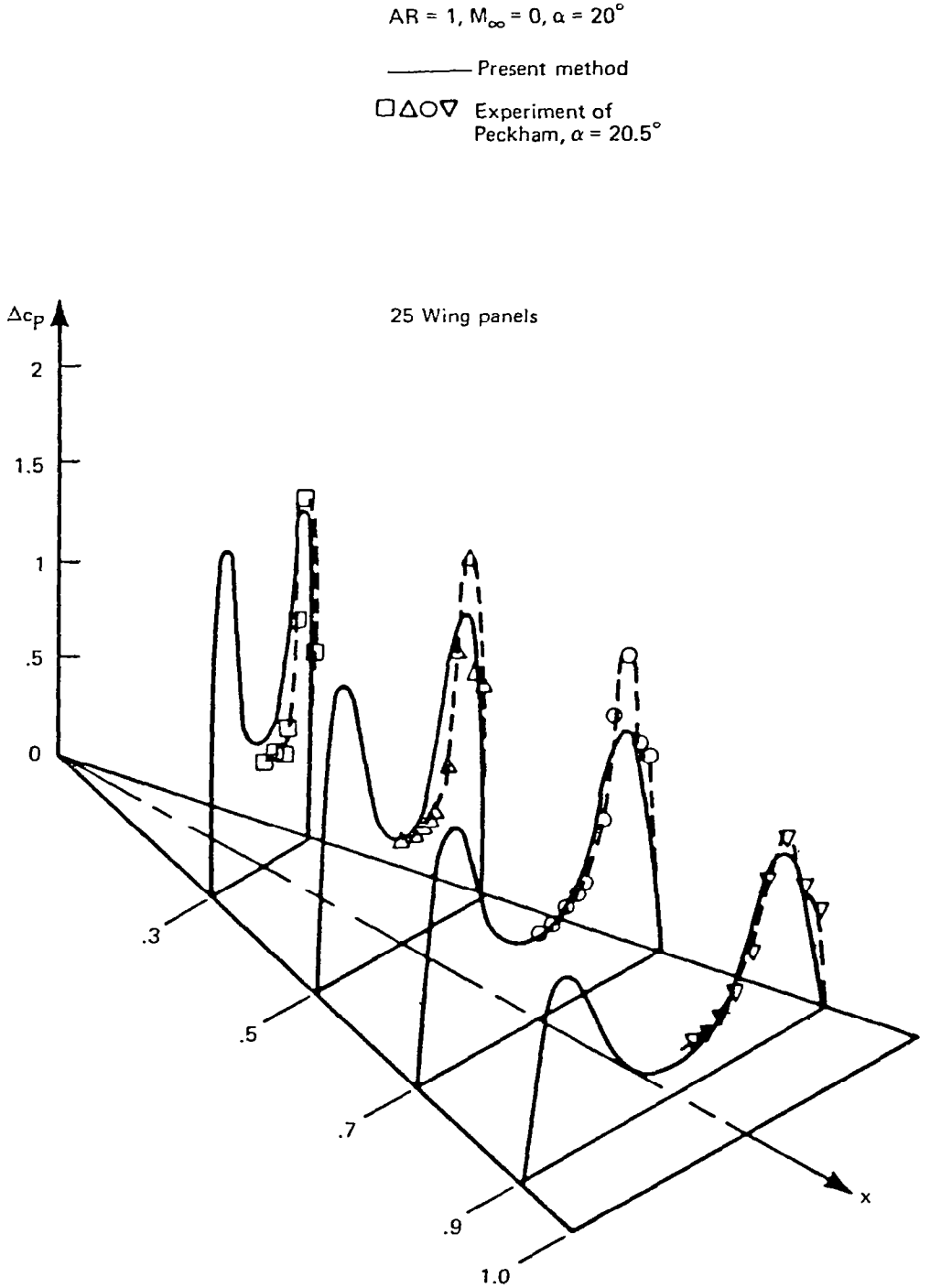

FIGURE 21 LOAD DISTRIBUTION OF DELTA WING, α = 20.0°

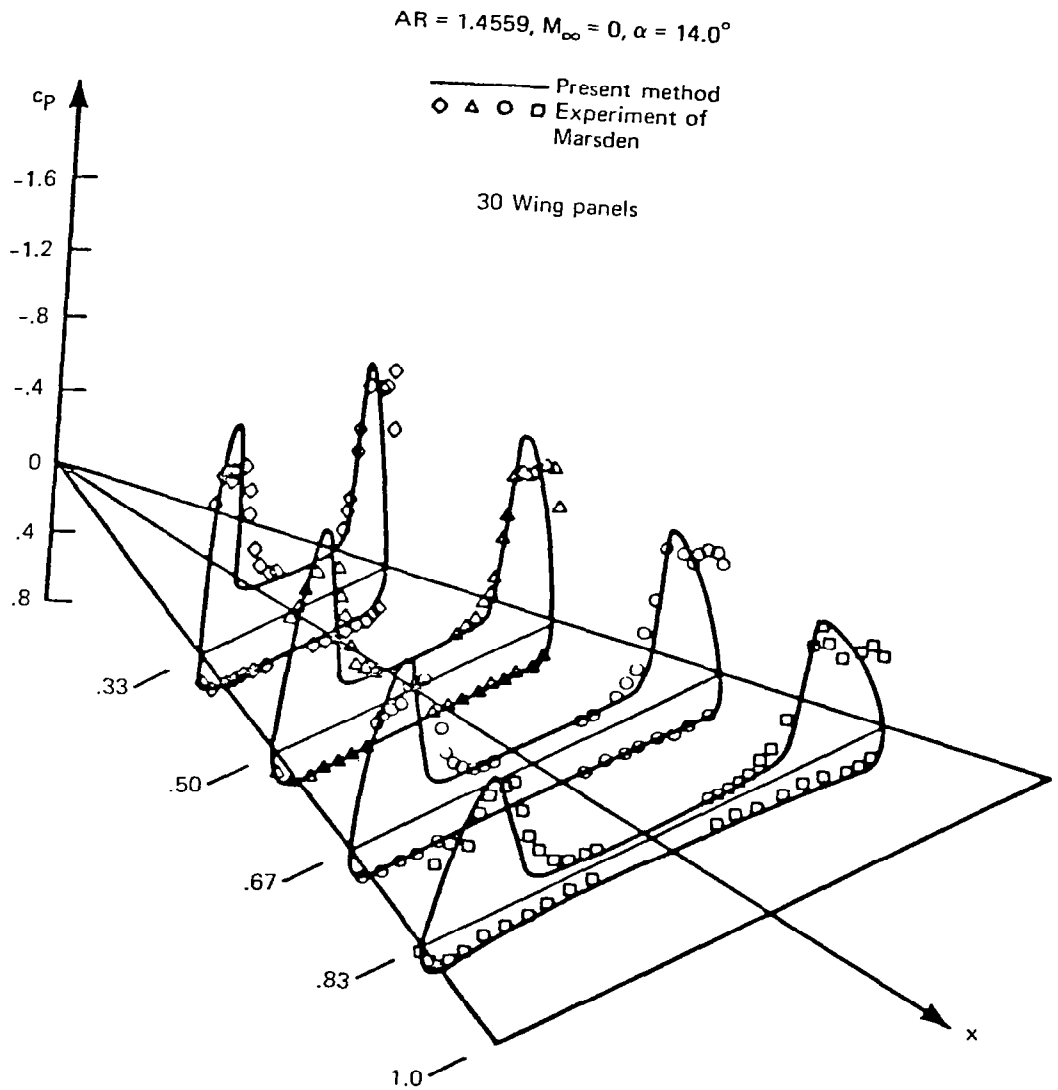

FIGURE 22 SURFACE PRESSURE DISTRIBUTION OF DELTA WING, $\alpha = 14.0^{o}$

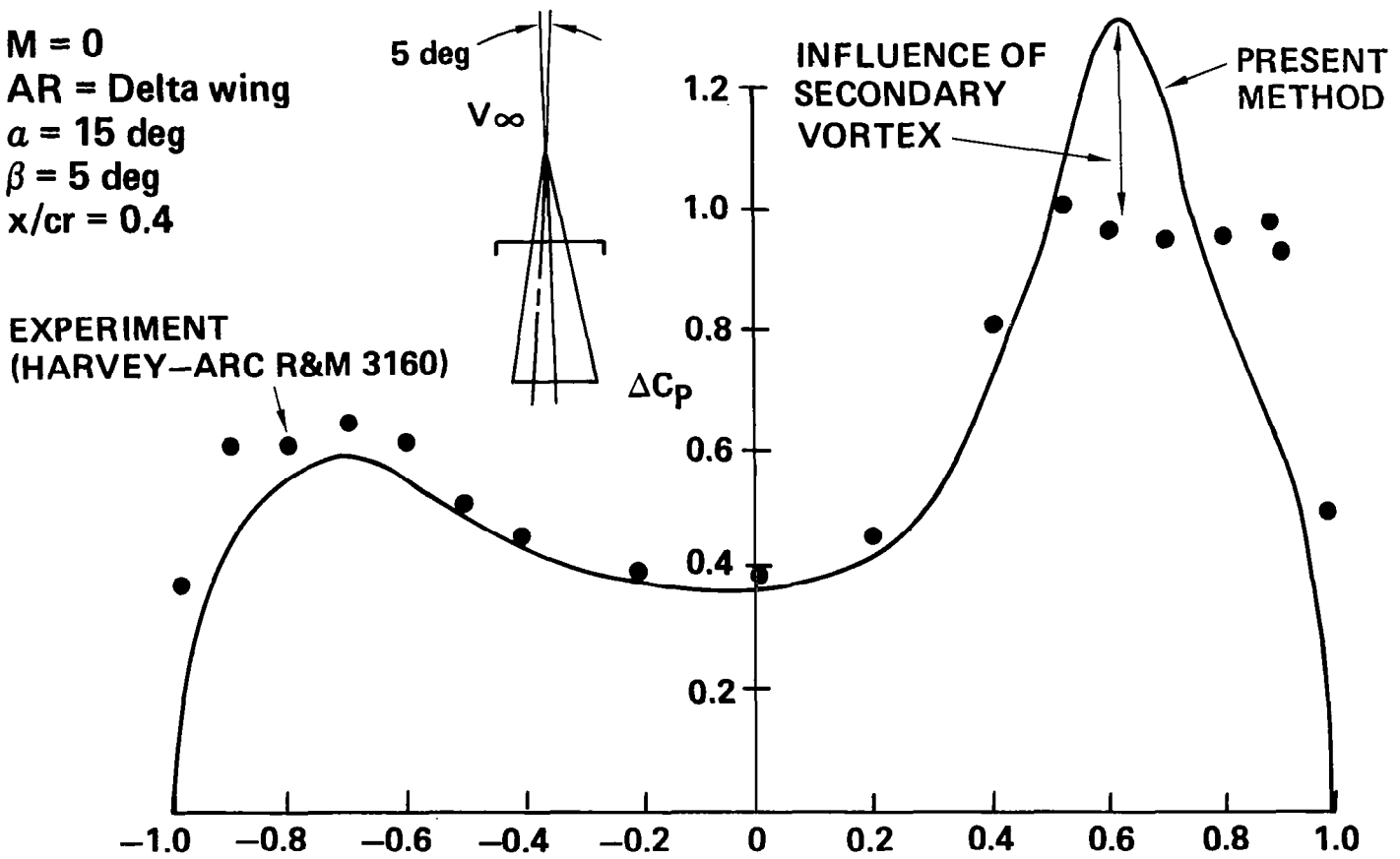

FIGURE 23 YAWED DELTA WING

comparisons were made for increasing yaw angles until one of the leading edges became parallel to the freestream. Agreement with test data comparable to that seen in Figure 23 was found in every case.

In order to validate the accuracy of the new code in reflecting aerodynamic differences due to camber changes, two wings first analyzed by Kuhlman (Ref. 18) were reanalyzed. These were delta wings of identical planform tested by Wentz (Ref. 27). The wing had an aspect ratio of 1.15 and 74° sweep. One wing was flat while the other had conical camber. These wings are illustrated in Figure 24. For the calculations, the wings were considered to have zero thickness. Calculated and measured pressure distributions are compared for both wings in Figure 25. While the differences in the measured pressure distributions due to the camber on the upper surface is small, the greater differences in the experimental data between the flat and cambered wing are also reflected in the theoretical results.

The code must further accurately predict drag increments between different camber wings. Drag polars are presented for the flat and cambered wings in Figure 26. Both calculated and measured results are shown. This comparison shows the drag differences to be predicted reasonably well by the improved code. At $C_L = 1.2$ the predicted drag reduction for the cambered wing is 5.7 percent compared to 7 percent given by Wentz for the measured data.

7.1.3 Wake Vorticity Rollup

An interesting property of the solution produced by the current method was discovered with the use of the near wake. In real flow over a delta wing with a leading edge vortex, the wake behind the wing will roll up into a vortex rotating counter to that of the leading edge vortex. The phenomenon has been known for some years and was clearly evident in the experimental measurements presented at a recent AGARD symposium on high angle of attack flows by Hummel (ref. 33). Examination of the doublet strength in the near wake and connecting free sheet clearly reflects this behavior. Doublet strength is plotted versus span fraction on the wake and unrolled free sheet for several cuts behind the delta wing in Figure 27. Near the trailing edge the doublet strength gradually rises toward the wing tip indicating an outward spanwise vorticity flow in a direction counter to that of the vortex core denoted by the sudden drop of doublet strength. (Note that the vorticity is the gradient of the doublet strength). Moving away from the trailing edge the variation of doublet strength becomes flatter except for the jumps behind the tip and vortex core. This indicates the concentration of vorticity into two counter rotating vortices just as in the real flow. Presumably it would be possible to replace the whole wake by such counter rotating vortices at about 0.5 root chords behind the wing in order to determine the effect on downstream components of a more complex configuration.

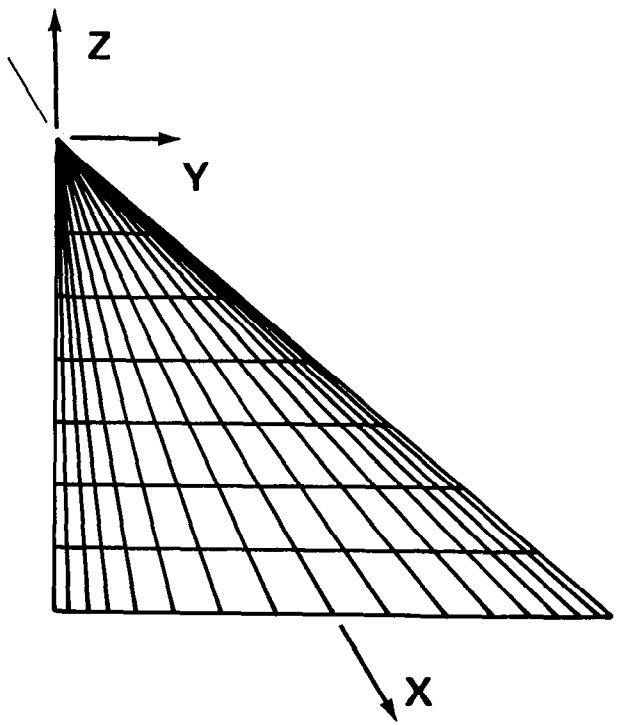

FLAT DELTA WING

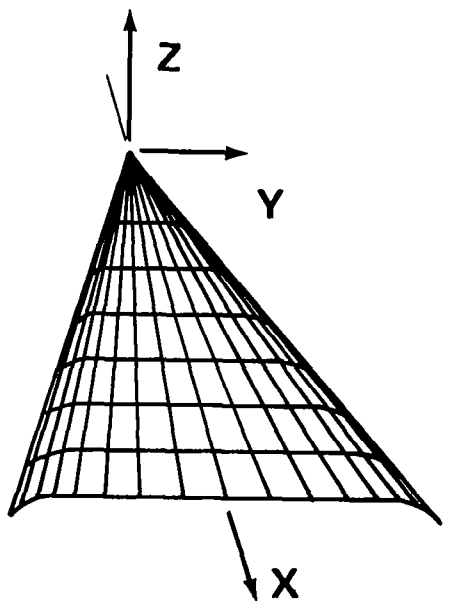

CONICAL CAMBER WING

FIGURE 24 ASPECT RATIO 1.15 DELTA WING

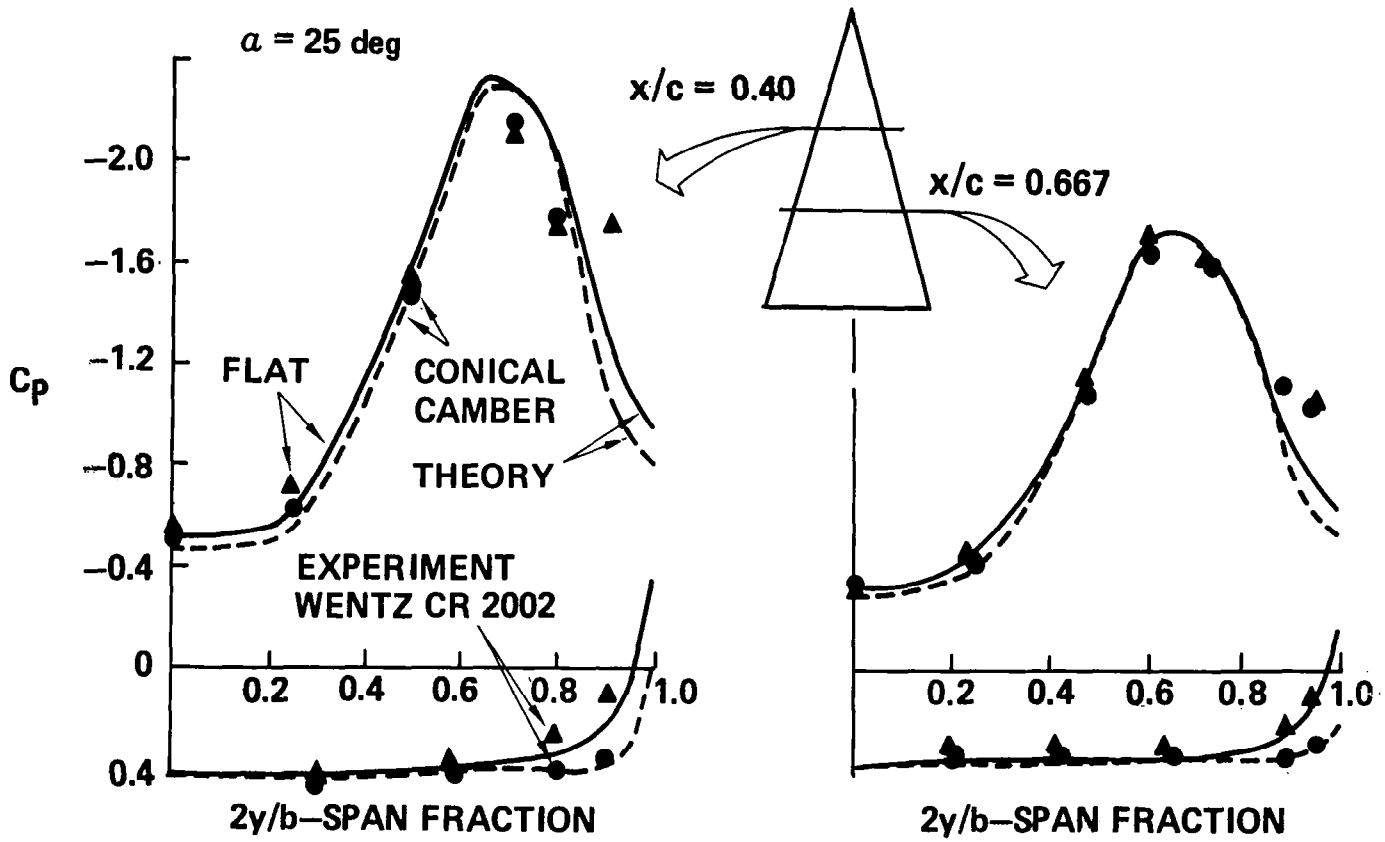

FIGURE 25 WING SURFACE PRESSURE DISTRIBUTION

DRAG POLAR COMPARISON

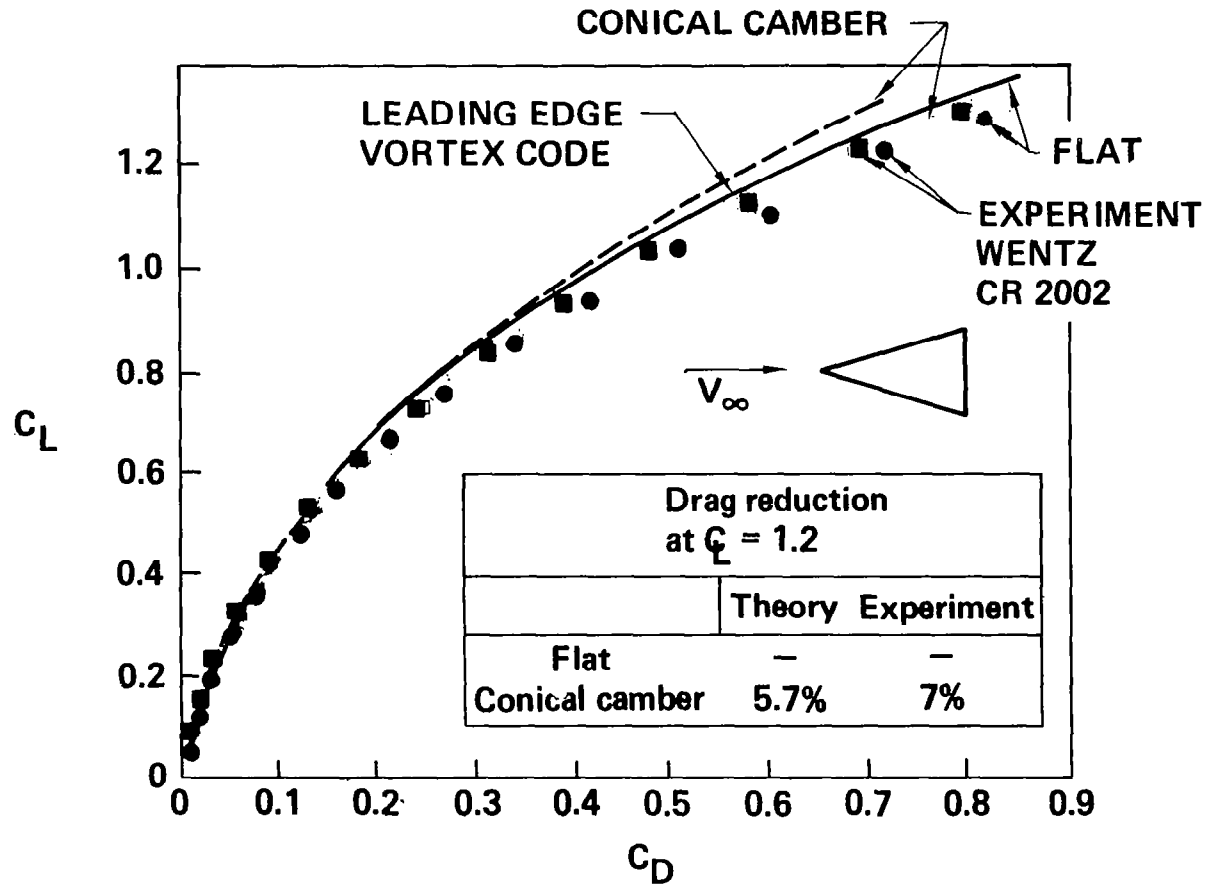

FIGURE 26 DRAG POLAR COMPARISON

DOUBLET STRENGTH IN THE NEAR WAKE

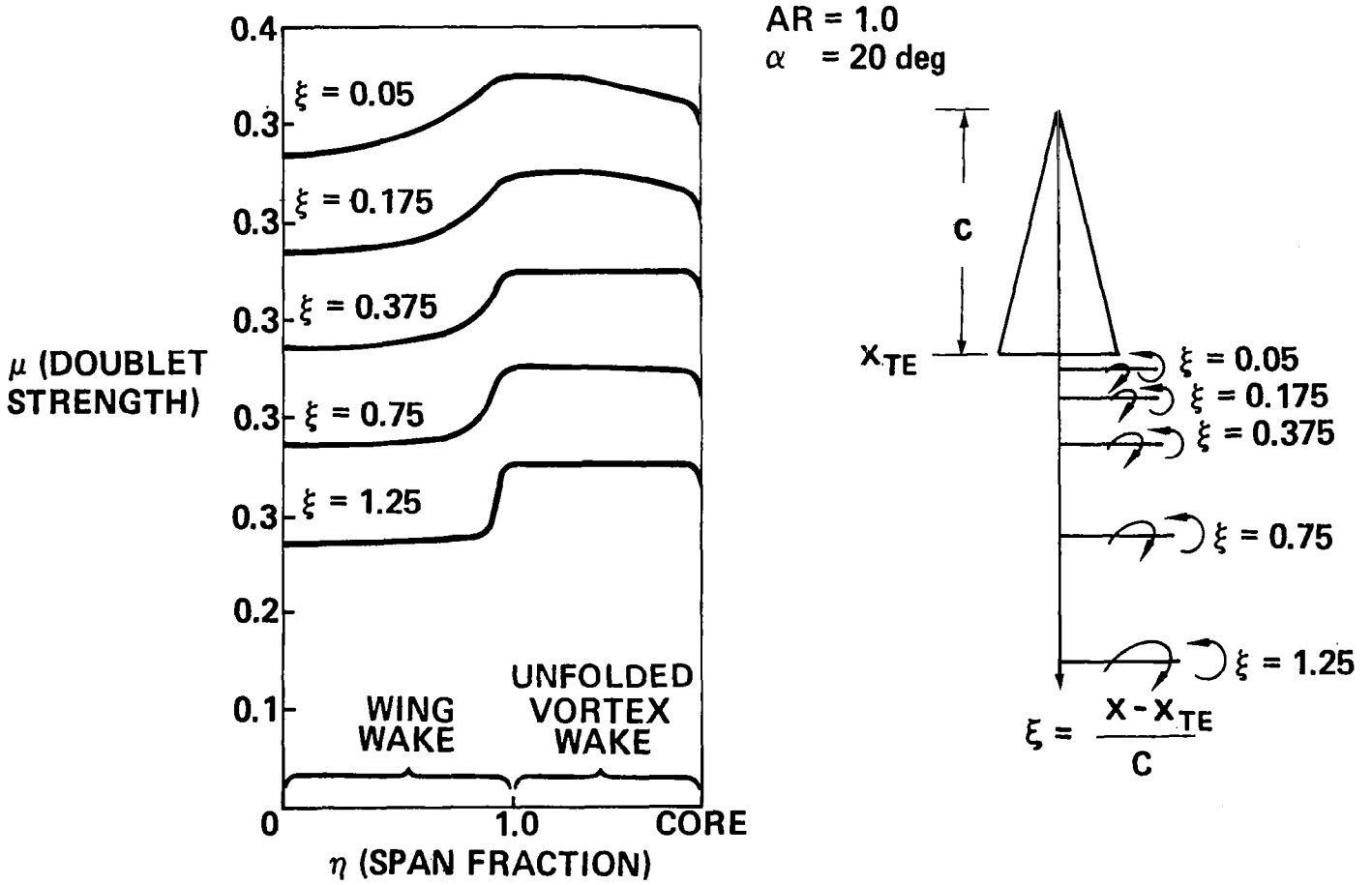

FIGURE 27 DOUBLET STRENGTH IN THE NEAR WAKE

7.2 Rectangular Wings

In Figure 28a converged geometry for an aspect ratio 0.5 rectangular wing with separated flow around the side edges is illustrated. Corresponding pressure distributions (ΔCp) are plotted in Figure 28b along with similar distributions for the same wing in an unseparated condition (which were generated by simply removing the vortex networks). Force and moment coefficients for rectangular wings of varying aspect ratio are shown in Figure 28c and comparisons with the suction analogy and experiment (reference 35) are good. Convergence for these cases required use of the least squares technique described in section 5.2.

Spanwise core locations at the trailing edge vary from 84 percent semispan at AR = 0.2 to 94 percent semispan at AR = 1.0 compared with around 70 percent semispan for delta wings. Core vertical displacements at the trailing edge vary from 13 percent chord at AR = 0.2 to 18 percent chord at AR = 1.0. This compares with 4 percent root chord at = 0.2 to 9 percent root chord at AR = 1.0 for delta wings. Trailing edge vortex core strengths for the rectangular wings are 12 percent higher at AR = 1.0 and 54 percent higher at AR = 0.2 than those of delta wings. The net result is that the spanwise flow at the trailing edge is markedly lower for rectangular wings, making use of near wake unnecessary for them.

7.3 Arrow Wings

Solutions for an arrow wing configuration have previously been calculated using the old code, reference 15. These results which are still considered valid are shown here for completeness. The experimental data is for an arrow wing-body configuration by Manro, references 35 and 36. An attempt with the old code to analyze the complete wing-body showed unacceptable slow convergence. Instead the configuration was modeled as a simple wing as shown in the inset on Figure 29. A near wake (type 6, Figure 3) was used to insure the proper Kutta condition at the trailing edge. The comparison with experimental data for the flat wing configuration shows generally good agreement considering the crudeness of the theoretical model.

An analysis was also made of the configuration with a trailing edge flap deflection. The lifting pressure comparisons are shown in Figure 30 which also includes results from an attached flow solution. While some discrepancies do exist, the LEV code results are in substantially better agreement with the experimental data than are those of the attached flow theory. Part of the descrepancy is obviously due to the presence of a secondary vortex. Near the wing tip, the simplification of the wing planform to a pointed tip instead of the actual clipped tip may also account for the poor test-theory correlation in that region.

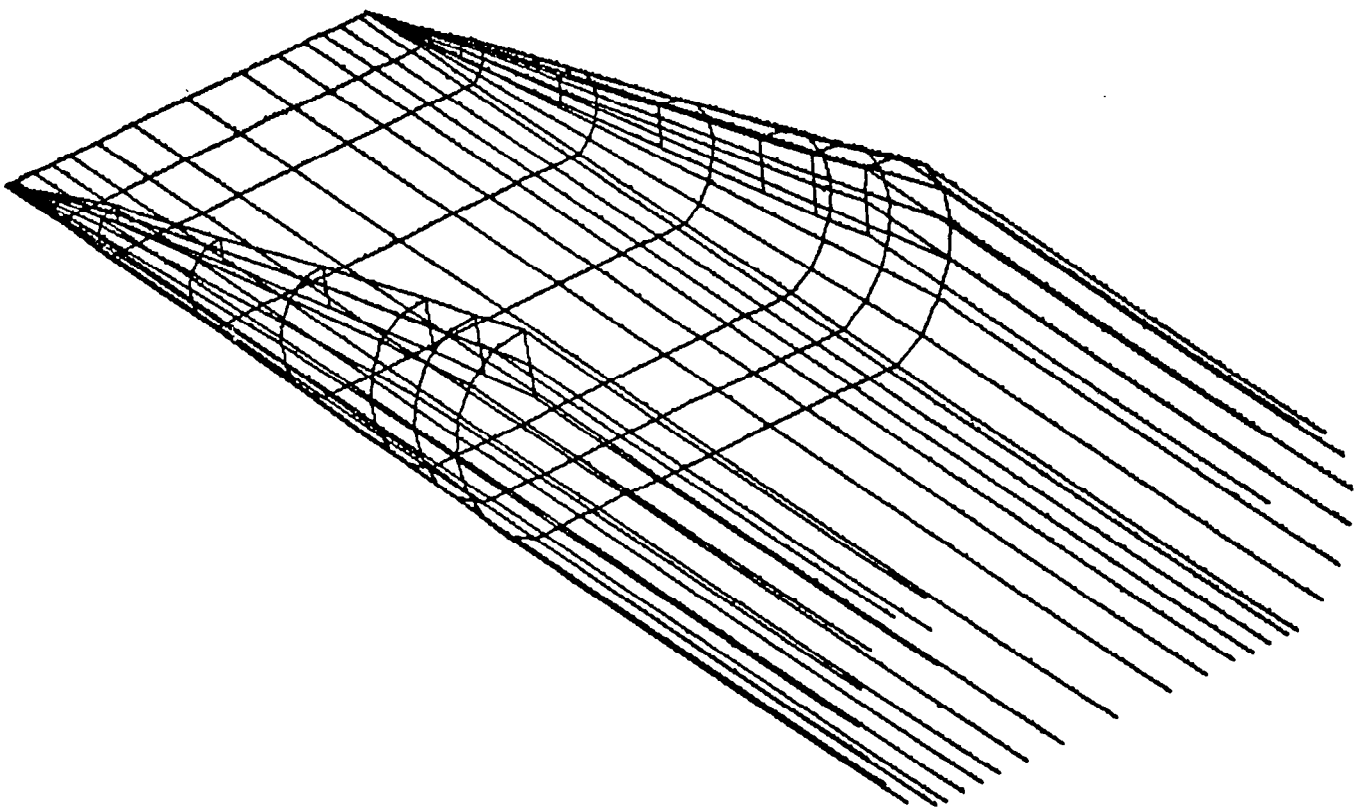

a. WING AND VORTEX SYSTEM GEOMETRY

FIGURE 28 RECTANGULAR WING WITH SIDE-EDGE SEPARATION

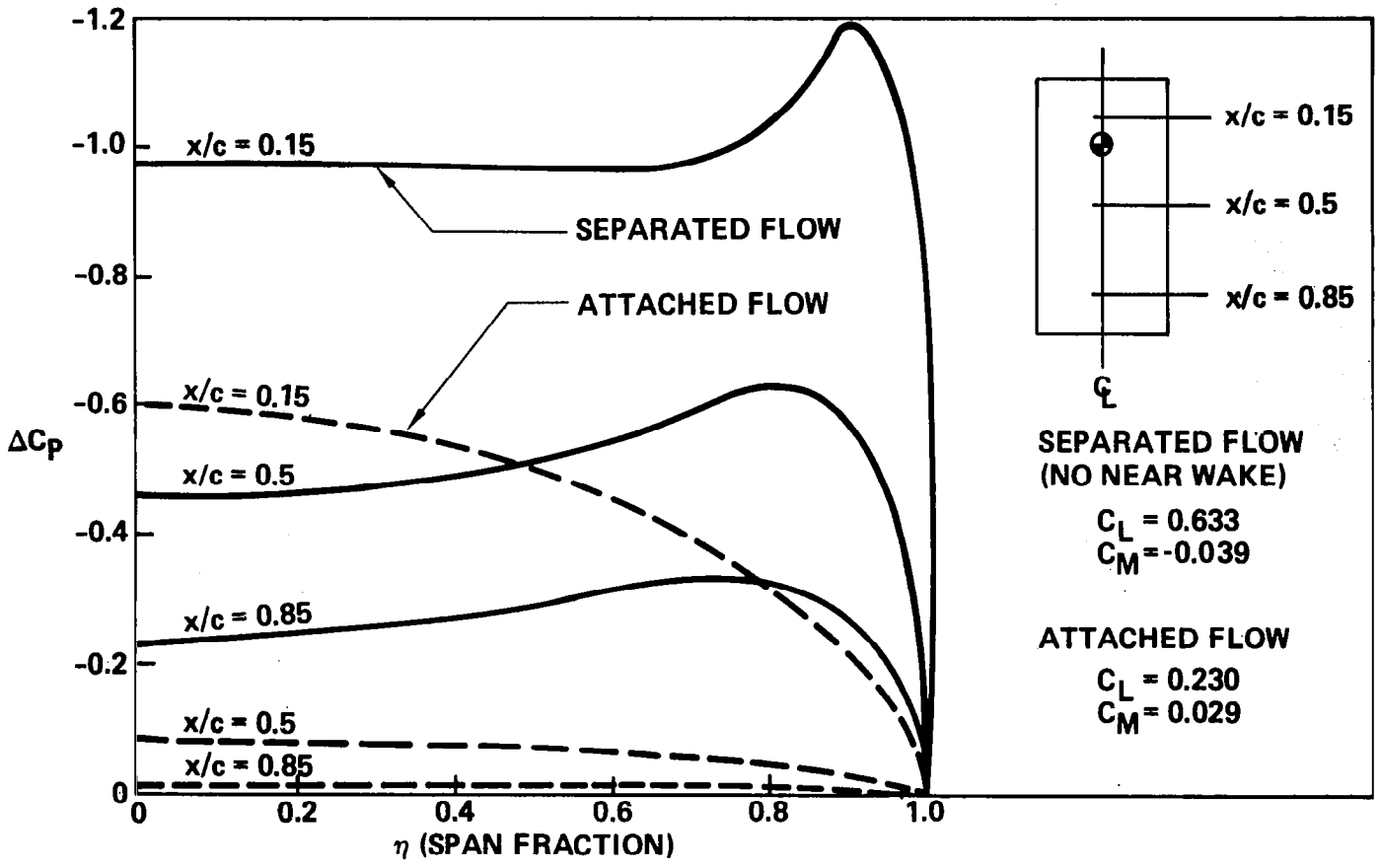

b. WING PRESSURE DISTRIBUTIONS (ΔC_p) AT AR = 0.5

FIGURE 28 CONTINUED

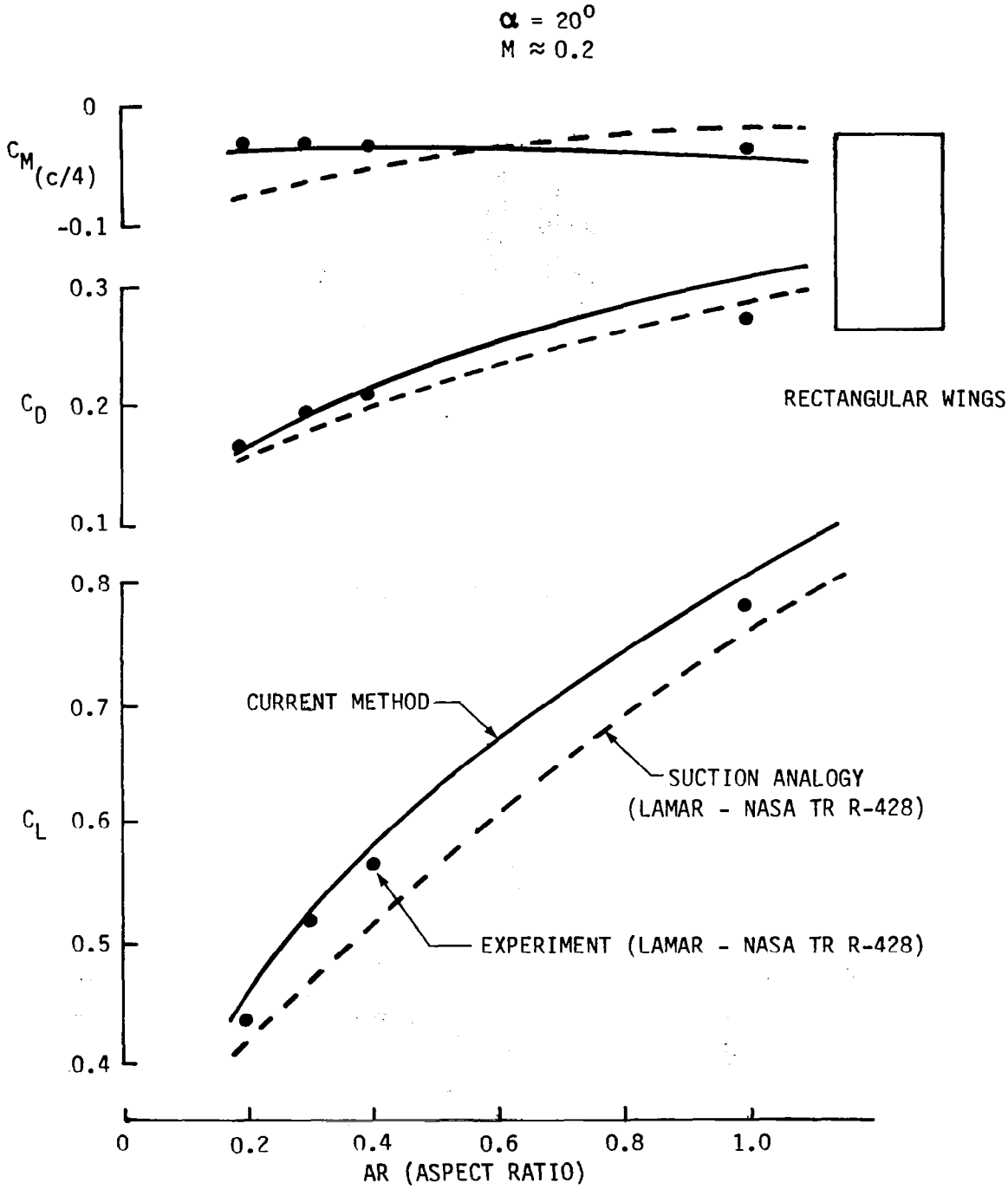

C. FORCE AND MOMENT COEFFICIENTS

FIGURE 28 CONCLUDED

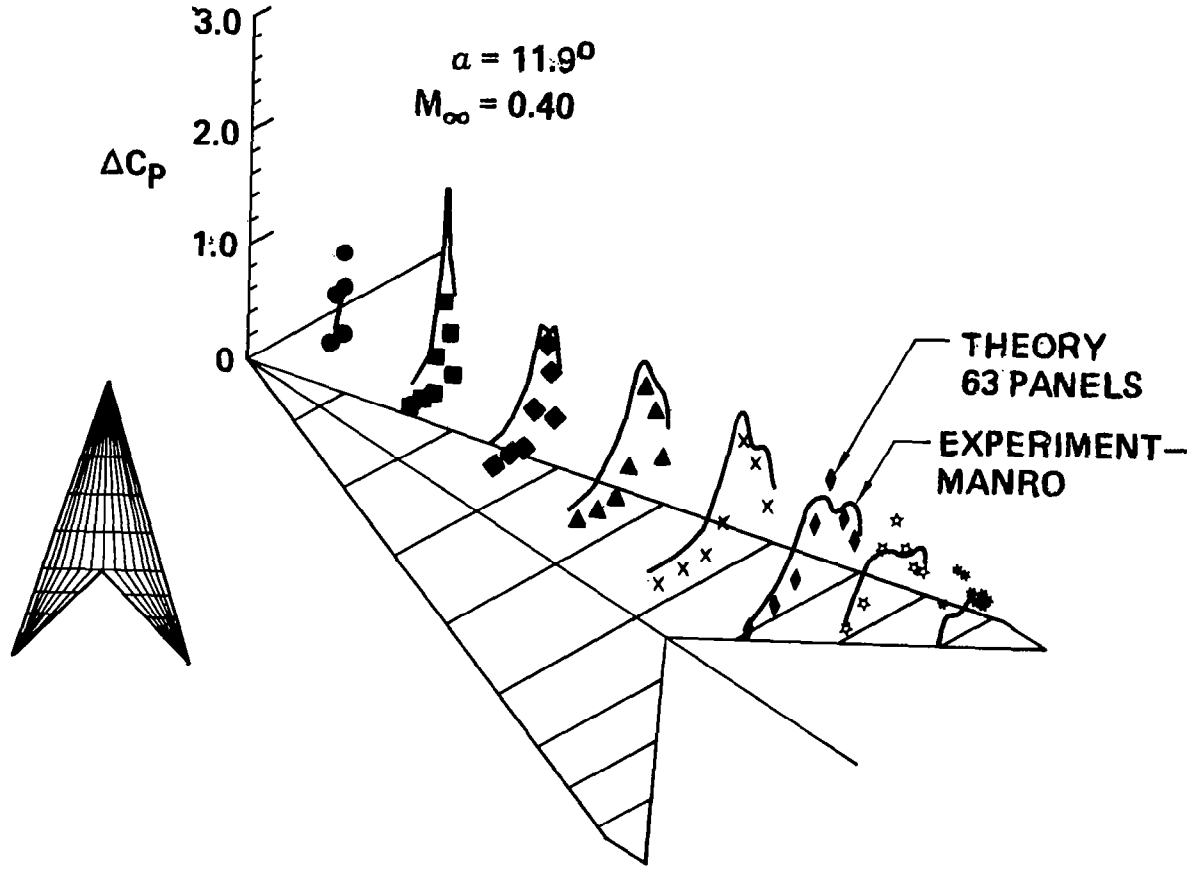

FIGURE 29 LIFTING PRESSURE DISTRIBUTION ON FLAT ARROW WING

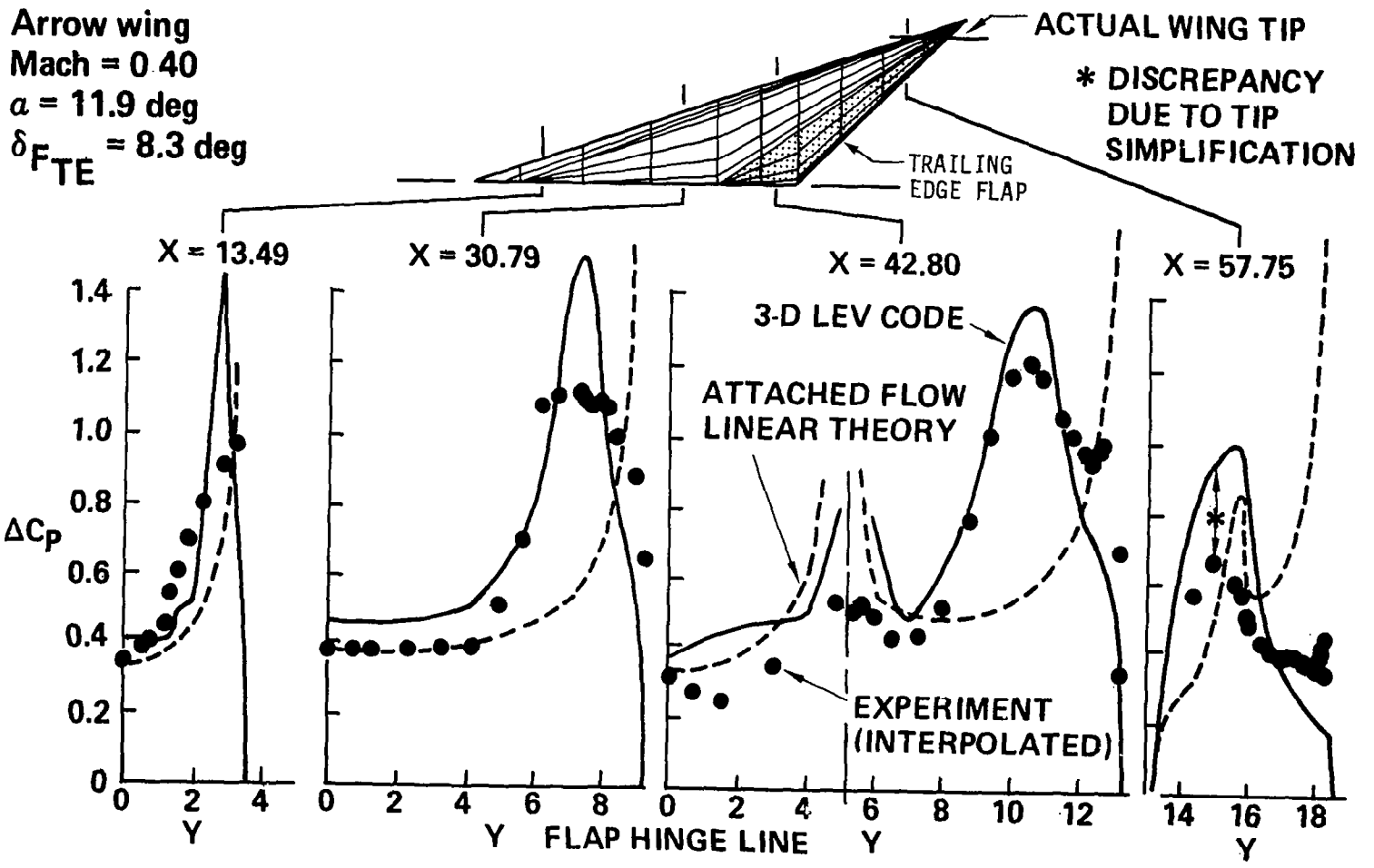

FIGURE 30 ARROW WING WITH TRAILING EDGE FLAP

8.0 CONCLUDING REMARKS

The advances described in this report clearly improve the usefulness of the current method in the study of separated vortex flow. In addition, the numerical examples set forth in section 6 give reasonable assurance that the data computed by the method faithfully reflects the underlying flow model. For those cases in which the real flow deviates significantly from the single well-formed vortex assumed in the flow model, the method will generally fail to converge. Finally, the results accumulated to date show that the flow model itself is representative of the physics in a wide variety of cases.

However, much work is still needed to improve the method to the point at which it exhibits reliability comparable to that of an attached potential method. Despite the advances made, difficulties may still occasionally be encountered with seemingly well posed problems.

Boeing Aerospace Company
P. O. Box 3999
Seattle, Washington 98124
July 1979

Appendix A

Hyperboloidal Panel Geometry

Definition

Let $\vec{Q}_1$, $\vec{Q}_2$, $\vec{Q}_3$ and $\vec{Q}_4$ be four panel corner points as shown in Figure A.1. The hyperboloidal panel H interpolating these points is defined as the point set

$$H = \left\{ \vec{Q}(s,t) \;\middle|\; \vec{Q}(s,t) = \vec{Q}_o + \vec{Q}_s s + \vec{Q}_t t + \vec{Q}_{st} st \;;\; s \in [-1,1],\; t \in [-1,1] \right\} \qquad (A.1)$$

where

$$\vec{Q}_o = 1/4\ (\vec{Q}_1 + \vec{Q}_2 + \vec{Q}_3 + \vec{Q}_4)$$
$$\vec{Q}_s = 1/4\ (\vec{Q}_1 - \vec{Q}_2 - \vec{Q}_3 + \vec{Q}_4)$$
$$\vec{Q}_t = 1/4\ (\vec{Q}_1 + \vec{Q}_2 - \vec{Q}_3 - \vec{Q}_4)$$
$$\vec{Q}_{st} = 1/4\ (\vec{Q}_1 - \vec{Q}_2 + \vec{Q}_3 - \vec{Q}_4)$$

General Characteristics

The fact that H interpolates the corner points is easily demonstrated by noting that $\vec{Q}(1,1) = \vec{Q}_1$, $\vec{Q}(-1,1) = \vec{Q}_2$, $\vec{Q}(-1,-1) = \vec{Q}_3$ and $\vec{Q}(1,-1) = \vec{Q}_4$. Moreover the boundary of H simply consists of the straight lines joining the corner points, a fact that can be checked by noting that for fixed $s = s_o$, $\vec{Q}(s_o,t)$ is linear in t and hence is a straight line segment. Similarly for fixed $t = t_o$. It is clear then that there will be no gaps between panels.

$\vec{Q}_o$ is the average of the corner points and lies on H since $\vec{Q}(0,0) = \vec{Q}_o$. $\vec{Q}_s$ is the vector from $\vec{Q}_o$ to the midpoint of the line segment joining $\vec{Q}_1$ to $\vec{Q}_4$ and $\vec{Q}_t$ is the vector from $\vec{Q}_o$ to the midpoint of the line segment joining $\vec{Q}_1$ to $\vec{Q}_2$. The line segments $\vec{Q}(0,t) = \vec{Q}_o + \vec{Q}_t t$, $t \in [-1,1]$ $\vec{Q}(s,0) = \vec{Q}_o + \vec{Q}_s s$, $s \in [-1,1]$ belonging to H are then simply the line segments joining the midpoints of opposite sides.

H is flat if and only if $\vec{Q}_{st}$ lies in the plane of $\vec{Q}_s$ and $\vec{Q}_t$, i.e., the near plane. If in particular $\vec{Q}_{st} = \vec{Q}_s$ then H is a triangle with $\vec{Q}_3 = \vec{Q}_4$. Similarly $\vec{Q}_{st} = \vec{Q}_t \iff \vec{Q}_2 = \vec{Q}_3$, $\vec{Q}_{st} = -\vec{Q}_s \iff \vec{Q}_1 = \vec{Q}_2$ and $\vec{Q}_{st} = -\vec{Q}_t \iff \vec{Q}_1 = \vec{Q}_4$. If $\vec{Q}_{st} = 0$ then H is a plane parallelogram, and vice versa.

Normal

Let us define

$$a_s = \frac{\partial \vec{Q}(s,t)}{\partial s} = \vec{Q}_s + \vec{Q}_{st} t = \frac{1}{2} \left[\vec{Q}(1,t) - \vec{Q}(-1,t) \right] \qquad (A.2)$$

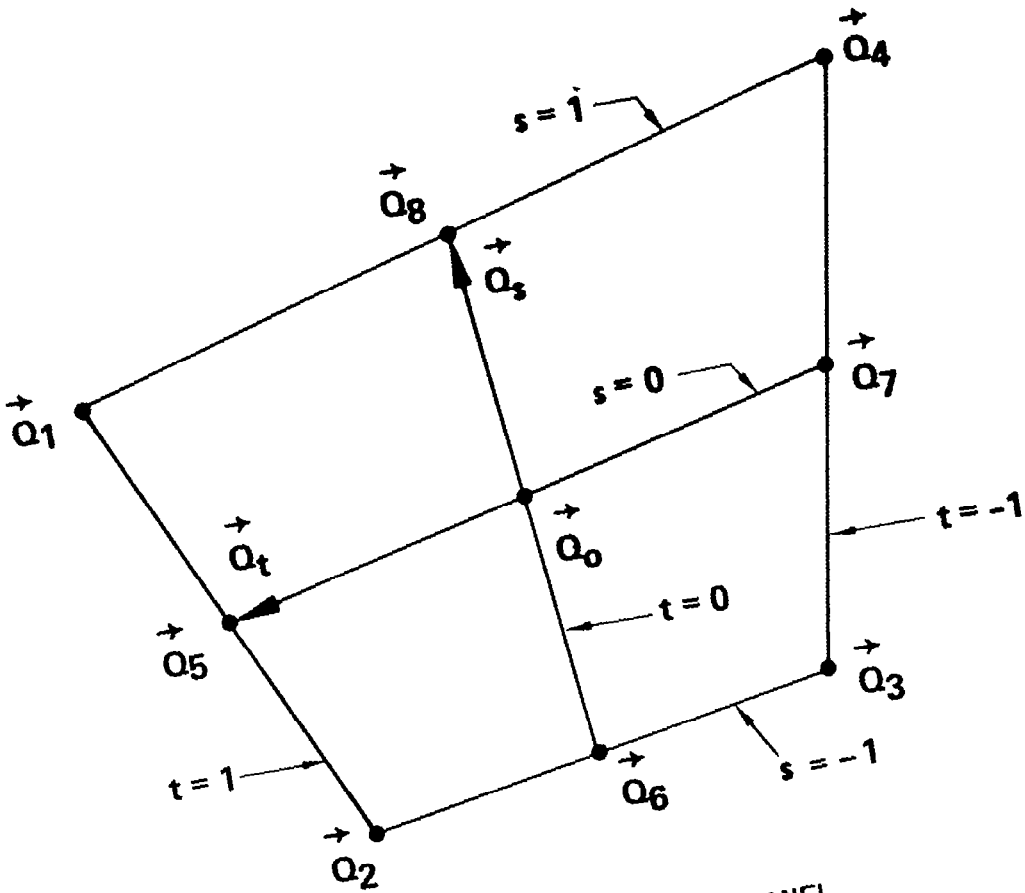

FIGURE A.1 HYPERBOLOIDAL PANEL

and

$$a_t = \frac{\partial \vec{Q}(s,t)}{\partial t} = \vec{Q}_t + \vec{Q}_{st}s = \frac{1}{2}\left[\vec{Q}(s,1) - \vec{Q}(s,-1)\right] \quad (A.3)$$

and

$$\vec{n} = \vec{a}_s \otimes \vec{a}_t = \vec{Q}_s \otimes \vec{Q}_t + \vec{Q}_s \otimes \vec{Q}_{st}s + \vec{Q}_{st} \otimes \vec{Q}_t t \quad (A.4)$$

$$= \vec{Q}_s \otimes \vec{Q}_t + (\vec{Q}_s s - \vec{Q}_t t) \otimes \vec{Q}_{st}$$

and

$$\hat{n} = \frac{\vec{n}}{|\vec{n}|} = \frac{\vec{a}_s \otimes \vec{a}_t}{|\vec{a}_s \otimes \vec{a}_t|} \quad (A.5)$$

Then $\hat{n} = \hat{n}(s,t)$ is the unit upper surface normal to H at (s,t). We note that $\hat{n}(0,0) = \vec{Q}_s \otimes \vec{Q}_t \,/\, \vec{Q}_s \otimes \vec{Q}_t$ is simply the unit normal to the near plane.

Area Element

The area element dA on H is given by

$$dA = |\vec{n}|\ dsdt = |\vec{a}_s \otimes \vec{a}_t|\ dsdt \quad (A.6)$$

Note then that

$$\hat{n}dA = \vec{n}dsdt = \vec{a}_s \otimes \vec{a}_t\ dsdt \quad (A.7)$$

Surface Derivatives

Let f(s,t) be defined on H, and let $\vec{\nabla}$ be the gradient operator in global coordinates. Then

$$\hat{n} \otimes \nabla f = \frac{1}{|\vec{a}_s \otimes \vec{a}_t|}\left[\vec{a}_t \frac{\partial f}{\partial s} - \vec{a}_s \frac{\partial f}{\partial t}\right] \quad (A.8)$$

and

$$\hat{n} \otimes \nabla f dA = \left[\vec{a}_t \frac{\partial f}{\partial s} - \vec{a}_s \frac{\partial f}{\partial t}\right] dsdt \quad (A.9)$$

Variational Properties

In this section we compute derivatives of various quantities with respect to panel deformations, i.e., changes in $\vec{Q}_1$, $\vec{Q}_2$, $\vec{Q}_3$ or $\vec{Q}_4$. Let $\vec{Q}_4$ be one of these points. Then

$$\frac{\partial \vec{Q}(s,t)}{\partial \vec{Q}_i} = I \left(\varepsilon_{oi} + \varepsilon_{si}\, s + \varepsilon_{ti} t + \varepsilon_{sti} st \right) \qquad (A.10)$$

where I is the 3x3 identify matrix and

$$\varepsilon_{01} = \frac{1}{4} \qquad \varepsilon_{02} = \frac{1}{4} \qquad \varepsilon_{03} = \frac{1}{4} \qquad \varepsilon_{04} = \frac{1}{4}$$

$$\varepsilon_{s1} = \frac{1}{4} \qquad \varepsilon_{s2} = -\frac{1}{4} \qquad \varepsilon_{s3} = -\frac{1}{4} \qquad \varepsilon_{s4} = \frac{1}{4}$$

$$\varepsilon_{t1} = \frac{1}{4} \qquad \varepsilon_{t2} = \frac{1}{4} \qquad \varepsilon_{t3} = -\frac{1}{4} \qquad \varepsilon_{t4} = -\frac{1}{4}$$

$$\varepsilon_{st1} = \frac{1}{4} \qquad \varepsilon_{st2} = -\frac{1}{4} \qquad \varepsilon_{st3} = \frac{1}{4} \qquad \varepsilon_{st4} = -\frac{1}{4}$$

Next we have

$$\frac{\partial a_s}{\partial \vec{Q}_i} = I \ (\varepsilon_{si} + \varepsilon_{sti}\ t) \qquad (A.11)$$

and

$$\frac{\partial a_t}{\partial \vec{Q}_i} = I \ (\varepsilon_{ti} + \varepsilon_{sti} s) \qquad (A.12)$$

and

$$\frac{\partial n}{\partial \vec{Q}_i} = \tilde{Q}_s (\varepsilon_{ti} + \varepsilon_{sti} s) - \tilde{Q}_t (\varepsilon_{si} + \varepsilon_{sti} t) + \tilde{Q}_{st} (\varepsilon_{si} s + \varepsilon_{ti} t) \qquad (A.13)$$

where $\tilde{Q}_s$, $\tilde{Q}_t$ and $\tilde{Q}_{st}$ are matrices defined as follows. Let $\vec{v}$ be the vector (v_1, v_2, v_3). Then

$$\tilde{V} = \begin{bmatrix} 0 & -v_3 & v_2 \\ v_3 & 0 & -v_1 \\ -v_2 & v_1 & 0 \end{bmatrix} \qquad (A.14)$$

From other considerations we have

$$\frac{\partial |\vec{n}|}{\partial \vec{Q}_i} = \hat{n}^T \frac{\partial \vec{n}}{\partial \vec{Q}_i} \tag{A.15}$$

and so

$$\frac{\partial \hat{n}}{\partial \vec{Q}_i} = \frac{1}{|\vec{n}|} \left[I - \hat{n}\hat{n}^T \right] \frac{\partial \vec{n}}{\partial \vec{Q}_i} \tag{A.16}$$

Applications to equations (A.6) and (A.7) are obvious, i.e.

$$\frac{\partial}{\partial \vec{Q}_i} dA = \hat{n}^T \frac{\partial \vec{n}}{\partial \vec{Q}_i} dsdt \tag{A.17}$$

$$\frac{\partial}{\partial \vec{Q}_i} (\hat{n} dA) = \frac{\partial \vec{n}}{\partial \vec{Q}_i} dsdt \tag{A.18}$$

Finally we deal with equations (A.8) and (A.9) differentiating (A.8) with respect to $\vec{Q}_4$ using (A.11), (A.12) and (A.15) we get

$$\frac{\partial}{\partial \vec{Q}_i} (\hat{n} \otimes \nabla f) = \left[\frac{\partial f}{\partial s} \left(\frac{1}{|\vec{n}|} \frac{\partial \vec{a}_t}{\partial \vec{Q}_i} - \frac{1}{|\vec{n}|^2} \vec{a}_t \hat{n}^T \frac{\partial \vec{n}}{\partial \vec{Q}_i} \right) - \frac{\partial f}{\partial t} \left(\frac{1}{|\vec{n}|} \frac{\partial \vec{a}_s}{\partial \vec{Q}_i} - \frac{1}{|\vec{n}|^2} \vec{a}_s \hat{n}^T \frac{\partial \vec{n}}{\partial \vec{Q}_i} \right) \right] \tag{A.19}$$

Differentiating (A.9) with respect to $\vec{Q}_i$ we get

$$\frac{\partial}{\partial \vec{Q}_i} (\hat{n} \otimes \vec{\nabla} f dA) = I \left[\frac{\partial f}{\partial s} (\epsilon_{ti} + \epsilon_{s_{ti}} s) - \frac{\partial f}{\partial t} (\epsilon_{si} + \epsilon_{sti} t) \right] dsdt \tag{A.20}$$

Appendix B

Panel Singularity Distributions

Doublet Distribution

We define 9 canonical panel locations as shown in figure B.1. We assume that doublet strength at these points is determined by a $9 \times N_d$ matrix B_d which relates these strengths to a N_d vector of neighboring doublet parameters. Let

$$\vec{\mu} = B_d \vec{S}_d \tag{B.1}$$

where

$$\vec{\mu} = (\mu_1, \mu_2, \mu_3, \mu_4, \mu_5, \mu_6, \mu_7, \mu_8, \mu_9)$$

Then the distribution of doublet strength $\mu(s,t)$ on the panel H is defined by

$$\begin{aligned}\mu(s,t) = \; & \mu_1\left[\tfrac{1}{4}\ st\ (1+s)(1+t)\right] + \mu_2\left[-\tfrac{1}{4}\ st\ (1-s)(1+t)\right] \\ & + \mu_3\left[\tfrac{1}{4} st\ (1-s)(1-t)\right] + \mu_4\left[-\tfrac{1}{4}\ st\ (1+s)(1-t)\right] \\ & + \mu_5\left[\tfrac{1}{2}\ t\ (1+t)(1-s^2)\right] + \mu_6\left[\tfrac{-1}{2}\ s(1-s)(1-t^2)\right] \\ & + \mu_7\ -\tfrac{1}{2}\left[t\ (1-t)(1-s^2)\right] + \mu_8\ \tfrac{1}{2}\left[s(1+s)(1-t^2)\right] \\ & + \mu_9\left[(1-s^2)(1-t^2)\right]\end{aligned} \tag{B.2}$$

From equation (B.2) we obtain

$$\begin{aligned}\frac{\partial \mu(s,t)}{\partial s} = \; & \mu_1\left[\tfrac{1}{4}\ (1+2s)t(1+t)\right] + \mu_2\left[\tfrac{-1}{4}\ (1-2s)t(1+t)\right] + \mu_3\ \tfrac{1}{4}\left[(1-2s)t(1-t)\right] \\ & + \mu_4\left[-\tfrac{1}{4}\ (1+2s)t(1-t)\right] + \mu_5\left[-\ st(1+t)\right] + \mu_6\left[-\tfrac{1}{2}\ (1-2s)(1-t^2)\right] \\ & + \mu_7\left[st(1-t)\right] + \mu_8\left[\tfrac{1}{2}\ (1+2s)(1-t^2)\right] + \mu_9\left[-2s(1-t^2)\right]\end{aligned} \tag{B.3}$$

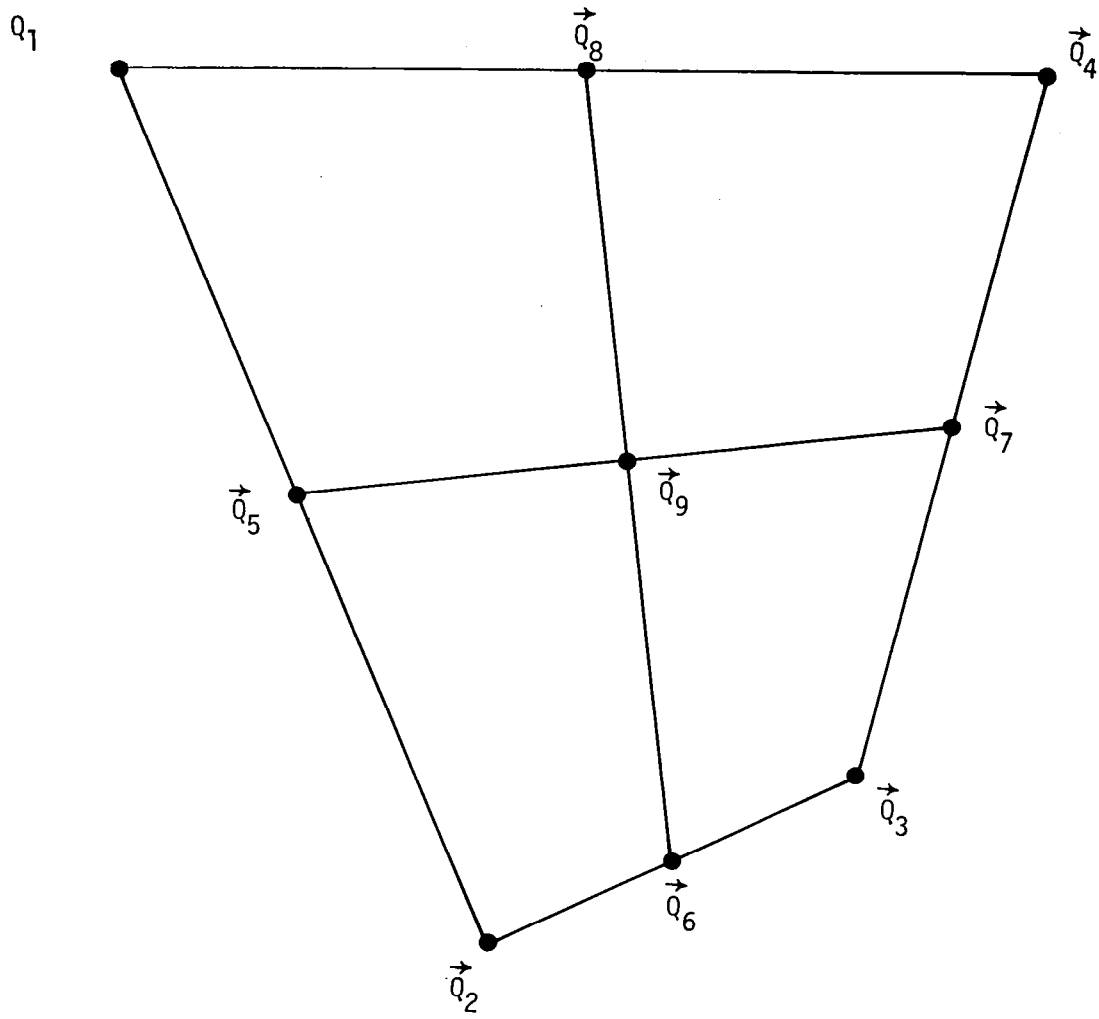

FIGURE B.1 THE 9 CANONICAL PANEL POINTS

and

$$\frac{\partial \mu(s,t)}{\partial t} = \mu_1 \left[\frac{1}{4}(1+2t)s(1+s)\right] + \mu_2 \left[-\frac{1}{4}(1+2t)s(1-s)\right] + \mu_3 \left[\frac{1}{4}(1-2t)s(1-s)\right]$$

$$+ \mu_4 \left[-\frac{1}{4}(1-2t)s(1+s)\right] + \mu_5 \left[\frac{1}{2}(1+2t)(1-s^2)\right] + \mu_6 \left[ts(1-s)\right] \qquad (B.4)$$

$$+ \mu_7 \left[-\frac{1}{2}(1-2t)(1-s^2)\right] + \mu_8 \left[-ts(1+s)\right] + \mu_9 \left[-2t(1-s^2)\right]$$

Let $\vec{q}(s,t)$ be the vector of coefficients of $\vec{\mu}$ in (B.2), then

$$\mu(s,t) = \vec{q}(s,t) \cdot \vec{\mu} \qquad (B.5)$$

$$\frac{\partial \mu}{\partial s}(s,t) = \frac{\partial \vec{q}(s,t)}{\partial s} \cdot \vec{\mu} \qquad (B.6)$$

$$\frac{\partial \mu}{\partial t}(s,t) = \frac{\partial \vec{q}(s,t)}{\partial t} \cdot \vec{\mu} \qquad (B.7)$$

Differentiation of Doublet Distribution

Let $\vec{\lambda}$ be the full vector of singularity parameters. Then $\partial \vec{s}_d / \partial \vec{\lambda}$ is simply a matrix containing almost all zeros except for those columns corresponding to the singularities of $\vec{s}_d$ which have a 1 in the appropriate row. Then

$$\frac{\partial \mu(s,t)}{\partial \vec{\lambda}} = \vec{q}(s,t) B_d \frac{\partial \vec{s}_d}{\partial \vec{\lambda}} \qquad (B.8)$$

$$\frac{\partial \mu(s,t)}{\partial s \, \partial \vec{\lambda}} = \frac{\partial \vec{q}(s,t)}{\partial s} B_d \frac{\partial \vec{s}_d}{\partial \vec{\lambda}} \qquad (B.9)$$

$$\frac{\partial \mu(s,t)}{\partial t \, \partial \vec{\lambda}} = \frac{\partial \vec{q}(s,t)}{\partial t} \; B_d \; \frac{\partial \vec{s}_d}{\partial \vec{\lambda}} \tag{B.10}$$

Assume the variation in $\vec{\mu}$ has been calculated with respect to any given corner point $\vec{Q}_i$. We have

$$\frac{\partial \mu(s,t)}{\partial \vec{Q}_i} = \vec{q}(s,t)^T \; \frac{\partial \vec{\mu}}{\partial \vec{Q}_i} \tag{B.11}$$

$$\frac{\partial^2 \mu(s,t)}{\partial s \, \partial \vec{Q}_i} = \frac{\partial \vec{q}(s,t)^T}{\partial s} \; \frac{\partial \vec{\mu}}{\partial \vec{Q}_i} \tag{B.12}$$

$$\frac{\partial^2 \mu(s,t)}{\partial t \, \partial \vec{Q}_i} = \frac{\partial \vec{q}(s,t)^T}{\partial t} \; \frac{\partial \vec{\mu}}{\partial \vec{Q}_i} \tag{B.13}$$

Source Distribution

We assume that the distribution of source strength on the panel $\sigma(s,t)$ times the area Jacobian $|a_s \otimes a_t|$ is linear, i.e.

$$\sigma(s,t) = \frac{|\vec{n}(0,0)|}{|\vec{n}(s,t)|} (\sigma_o + \sigma_s s + \sigma_t t) \tag{B.14}$$

Let B_s be the matrix which relates the coefficient vector $\vec{\sigma} = (\sigma_o, \sigma_s, \sigma_t)$ to an N_s vector of neighboring source parameters $\vec{S}_s$ so that

$$\vec{\sigma} = B_s \vec{S}_s \tag{B.15}$$

To obtain B_s we construct a local near plane coordinate system at $\vec{Q}_0$ with transformation matrix A_{np} such that

$$A_{np}^{-1} = \left[\vec{Q}_s, \; \vec{Q}_t, \; \frac{\vec{Q}_s \otimes \vec{Q}_t}{\sqrt{|\vec{Q}_s \otimes \vec{Q}_t|}} \right] \tag{B.16}$$

Let $\vec{\pi}_k$ be the locations of neighboring source singularity parameters in this local coordinate system with $\vec{\pi}_k = (\xi_k, \eta_k, \zeta_k)$. Then the coefficients σ_o, σ_s and σ_t are obtained by least squaring the distribution $\sigma(\xi,\eta) = \sigma_o + \sigma_s\xi + \sigma_t\eta$ to the points $\vec{\pi}$ with heavy weight on the point (0,0,0).

In the same manner as for equation (B.11) we have

$$\frac{\partial\sigma(s,t)}{\partial\vec{\lambda}} = \frac{|\bar{n}(0,0)|}{|\bar{n}(s,t)|}\vec{r}(s,t)^T \frac{\partial\vec{\sigma}}{\partial\vec{\lambda}} \qquad (B.17)$$

where

$$r(s,t) = (1,s,t)$$

and

$$\frac{\partial\sigma}{\partial\vec{\lambda}} = B_s \frac{\partial\bar{s}_s}{\partial\vec{\lambda}}$$

Calculation of the Derivative of Doublet Strength with Respect to the Panel Grid Points

From equation B.11, we have

$$\frac{\partial\mu(s,t)}{\partial\vec{Q}_i} = \vec{q}(s,t)\frac{\partial\vec{\mu}}{\partial\vec{P}_i} \qquad (B.18)$$

Where $\vec{\mu}(s,t)$ is the doublet strength at a control point expressed in terms of the parameters s,t of a hyperbolic paraboloid element, q(s,t) is the coefficient vector of $\vec{\mu}$, and $\vec{\mu} = B_d\vec{\lambda}$ with $\vec{\mu} = (\mu_1, \mu_2, \ldots\ldots, \mu_9)$ corresponding to values of doublet strength at the 9 canonical points of H-P panel.

Finite difference approximation will be used to evaluate the derivatives $\partial\vec{\mu}/\partial Q_i$. For each panel of a doublet/design network with its geometry perturbed, an outer spline, giving the dependence of the doublet strength at the 9 canonical points of the panel on the 16 neighboring points with the specified singularity parameters (see scheme to construct the outer spline for doublet/design type I), will be constructed. The 9 doublet strength coefficients ($\vec{\mu} = (\mu_1, \mu_2, \ldots, \mu_9)$) for the panel can be obtained from either multiplying the matrix B by the vector consisting of the values of the 16 singularity parameters or the direct solution $A\vec{\mu} = \lambda$ (i.e. B_d is the generalized inverse of A). Then we perturb the 16 neighboring points one at a time and calculate a new $\vec{\mu}_p$ for each perturbed point. Using $\vec{\mu}$ and the associated $\vec{\mu}_p$ for each perturbed grid point, we compute the finite difference approximation of $\partial\vec{\mu}/\partial Q_i$. For a given panel, the derivatives of the doublet strength with respect to the network grid points can be assembled as a 9x16 matrix,

$$\frac{\partial\mu}{\partial Q_i} = \begin{pmatrix} \frac{\partial\mu_1}{\partial Q_1} & \cdots & \frac{\partial\mu_1}{\partial Q_{16}} \\ \frac{\partial\mu_2}{\partial Q_1} & & \frac{\partial\mu_2}{\partial Q_{16}} \\ \vdots & & \vdots \\ \frac{\partial\mu_9}{\partial Q_1} & \cdots & \frac{\partial\mu_9}{\partial Q_{16}} \end{pmatrix} \qquad (B.19)$$

Appendix C

Control Point Locations

Panel Center Control Points

We assume that all panel center control points are located at $(s,t) = (0,0)$.

Network Edge and Corner Control Points

The hypothetical location of all panel edge and corner control points are also defined in terms of s and t. For a control point located at panel corner $\vec{Q}_1$ for example we have $(s,t) = (1,1)$. For a control point located at edge midpoint $\vec{Q}_5$ we have $(s,t) = (0,1)$. For edge and corner control points with real boundary conditions the actual control point location will not coincide with the hypothetical location but will be withdrawn into the panel slightly. For example if the hypothetical location is $(s,t) = (1,1)$ the actual location will be $(s,t) = (1 - \delta , 1 - \delta)$. Here δ is say 0.1. If the hypothetical location is $(s,t) = (0,1)$ then the actual location will be $(s,t) = (0,1 - \delta)$, etc.

Appendix D

Potential and Velocity Influence Coefficients

Preliminaries

Let C be the compressibility direction unit vector and $\beta^2 = 1 - M_\infty^2$.

Define the matrix A by

$$A = \beta^2 I + (1-\beta^2)\,\hat{C}\hat{C}^T \tag{D.1}$$

and the matrix B by

$$B = I + (\beta^2-1)\,\hat{C}\hat{C}^T = \beta^2 A^{-1} \tag{D.2}$$

Let $\vec{P}$ be a field point and let $\vec{Q}$ be a point on H. Let

$$\vec{R} = \vec{P} - \vec{Q} \tag{D.3}$$

We now define R, the norm of $\vec{R}$, by

$$R = \sqrt{\vec{R}^T A\vec{R}} \tag{D.4}$$

Next define

$$N = \begin{cases} 4 & M_\infty < 1 \\ 2 & M_\infty > 1 \end{cases} \tag{D.5}$$

The source potential ϕ_S induced by a source distribution σ on H is defined by

$$\phi_S = -\frac{1}{4\pi}\iint_H \frac{\sigma}{R}\, dS_Q \tag{D.6}$$

The doublet potential ϕ_d induced by a doublet distribution μ on H is defined by

$$\phi_d = \frac{1}{4\pi} \iint_h \mu(\hat{n}\cdot\overleftarrow{\nabla}_Q) \frac{1}{R} \, dS_Q$$

$$= \frac{\beta^2}{4\pi} \iint_H \frac{\mu \hat{n} \cdot \vec{R}}{R^3} \, dS_Q \qquad (D.7)$$

where

$$\overleftarrow{\nabla}_Q = B \frac{\partial}{\partial \vec{Q}}$$

The source velocity $\vec{V}_S$ induced by a source distribution σ on H is defined by

$$\vec{V}_S = \nabla_p \vec{\phi}_s = -\frac{1}{4\pi} \iint_H \sigma \vec{\nabla}_p \frac{1}{R} \, dS_Q$$

$$= +\frac{A}{4\pi} \iint_H \sigma \frac{\vec{R}}{R^3} \, dS_Q \qquad (D.8)$$

The doublet velocity $\vec{V}_d$ induced by a doublet distribution μ on H is defined by

$$\vec{V}_d = \vec{\nabla}_p \phi_d = \frac{1}{4\pi} \iint_H (\hat{n} \cdot \overleftarrow{\nabla}_Q) \vec{\nabla}_p \frac{1}{R} \, ds_Q$$

$$= \frac{1}{4\pi} \iint_H (\hat{n} \otimes \vec{\nabla}\mu) \otimes \overleftarrow{\nabla}_Q \frac{1}{R} \, ds_Q + \frac{1}{4\pi} \int_L \mu \overleftarrow{\nabla}_Q \frac{1}{R} \otimes d\vec{\ell}_Q$$

$$= \frac{\beta^2}{4\pi} \iint_H (\hat{n} \otimes \vec{\nabla}\mu) \otimes \frac{\vec{R}}{R^3} \, ds_Q + \frac{\beta^2}{4\pi} \int_L \frac{\mu \vec{R} \otimes d\vec{\ell}_Q}{R^3} \qquad (D.9)$$

The line integral on the right of (D.9) cancels with the corresponding line integral for adjacent panels and may be ignored except on the panel edge corresponding to the vortex core. For the purpose of evaluating the remaining integrals on the right sides of (D.6), (D.7), (D.8), and (D.9) we approximate H by a flat quadrilateral panel Σ. Σ lies on the plane passing through $\vec{Q}_0$ having a constant normal $\hat{n}$ in the direction $\vec{Q}_s \otimes \vec{Q}_t$. Σ is obtained by projecting the corner points of H onto this plane in a manner to be described later. A local compressible (x',y',z') coordinate system may be defined on Σ in the following way.

$$\begin{pmatrix} X' \\ Y' \\ Z' \end{pmatrix} = T\left\{\begin{pmatrix} X \\ Y \\ Z \end{pmatrix} - \begin{pmatrix} X_0 \\ Y_0 \\ Z_0 \end{pmatrix}\right\} \tag{D.10}$$

where (x,y,z) are the coordinates of a point in the global coordinate system and (x_0,y_0,z_0) are the components of Q_0. The transformation T is defined the column vectors comprising T^{-1}, i.e.,

$$T^{-1} = \begin{pmatrix} \vec{u} & \vec{v} & \vec{w} \\ \downarrow & \downarrow & \downarrow \end{pmatrix} \tag{D.11}$$

so that $\vec{u}$, $\vec{v}$, and $\vec{w}$ are the coordinate axes of the local coordinate system. The vector $\vec{w}$ is defined by

$$\vec{w} = \alpha \tilde{n} \tag{D.12}$$

where

$$\alpha = \frac{1}{\beta\sqrt{(\hat{n}\cdot\tilde{n})}}, \qquad \tilde{n} = B\,\hat{n}$$

The vectors $\vec{u}$ and $\vec{v}$ lie in the plane of Σ and are orthogonal. We have

$$\vec{u} = \frac{1}{(\hat{n}\cdot\tilde{n})} \begin{pmatrix} \sqrt{n_y^2 + n_z^2} \\ -n_x\, n_y \Big/ \sqrt{n_y^2 + n_z^2} \\ -n_x\, n_z \Big/ \sqrt{n_y^2 + n_z^2} \end{pmatrix} \qquad \vec{v} = \begin{pmatrix} 0 \\ n_z \Big/ \sqrt{n_y^2 + n_z^2} \\ -n_y \Big/ \sqrt{n_y^2 + n_z^2} \end{pmatrix} \tag{D.13}$$

If $(n_y^2 + n_z^2) = 0$ then we define $n_y \Big/ \sqrt{n_y^2 + n_z^2} = 1$ and

$$n_z \Big/ \sqrt{n_y^2 + n_z^2} \equiv 0.$$

We now express the integrals of (D.6), (D.7), (D.8) and (D.9) in terms of local coordinates. We have

$$dS = \left|\vec{u} \otimes \vec{v}\right| \, d\xi' d\eta' = \alpha d\xi' d\eta' \tag{D.14}$$

$$R = \sqrt{(\xi' - x')^2 + (\eta' - y')^2 + (\zeta' - z')^2} \tag{D.15}$$

$$\hat{n}\cdot\vec{R} = z' / \beta^2\alpha \tag{D.16}$$

$$(\hat{n} \otimes \vec{\nabla}\mu) \otimes \tilde{\nabla}_Q = T^T\left[(\mu_\xi, \mu_\eta, 0)\frac{\partial}{\partial\zeta'} - (0,0,1)\left(\mu_\xi \frac{\partial}{\partial\xi'} + \mu_\eta \frac{\partial}{\partial\eta'}\right)\right] \tag{D.17}$$

Hence

$$\Phi_s = -\frac{\alpha}{N\pi}\iint_{\Sigma}\frac{\sigma}{R}\,d\xi'd\eta' \tag{D.18}$$

$$\Phi_d = \frac{1}{N\pi}\iint_{\Sigma}\frac{\mu z'}{R^3}\,d\xi'd\eta' \tag{D.19}$$

$$\vec{V}_s = T^T\frac{\alpha}{N\pi}\iint_{\Sigma}\sigma\frac{(\xi'-x',\eta'-y',\zeta'-z')}{R^3}\,d\xi'\,d\eta' \tag{D.20}$$

$$\vec{V}_d = T^T\frac{1}{N\pi}\iint_{\Sigma}\frac{1}{R^3}\left(z'\frac{\partial\mu}{\partial\xi},\ z'\frac{\partial\mu}{\partial\eta},\ (\xi'-x')\frac{\partial\mu}{\partial\xi'}+(\eta'-y')\frac{\partial\mu}{\partial\eta'}\right)d\xi'\,d\eta' \tag{D.21}$$

The singularity distributions σ and μ can be expresses in terms of ξ and η, however since σ and μ are defined in terms of s and t, and s and t are not polynomials in ξ and η, the resultnt distributions would not be polynomials in ξ and η. Therefore we approximate σ by a linear distribution and μ by a quadratic distribution in ξ and η. The approximation is defined by requiring that the derivatives of these approximations evaluated at $\xi=\eta=0$ agree with the exact derivatives of σ and μ to the respective order of the approximation. For this purpose we use the following formulas:

$$\frac{\partial f}{\partial\xi'} = \lambda_o\left[\eta_t\frac{\partial f}{\partial s} - \eta_s\frac{\partial f}{\partial t}\right]$$

$$\frac{\partial f}{\partial\eta'} = \lambda_o\left[-\xi_t\frac{\partial t}{\partial s} + \xi_s\frac{\partial f}{\partial t}\right]$$

$$\frac{\partial^2 f}{\partial\xi^2} = \lambda_o^2\left[\left(\eta_t\eta_{st} + \eta_t\Delta\eta\right)\frac{\partial f}{\partial s} + \left(\eta_s\eta_{st} - \eta_s\Delta\eta\right)\frac{\partial f}{\partial t} + \eta_t^2\frac{\partial^2 f}{\partial s^2} - 2\eta_s\eta_t\frac{\partial^2 t}{\partial s\partial t} + \eta_s^2\frac{\partial^2 f}{\partial t^2}\right] \tag{D.22}$$

$$\frac{\partial^2 f}{\partial \xi' \partial \eta'} = \lambda_o^2 \left[-\left(\xi_t \eta_{st} + \eta_t \Delta_\xi\right)\frac{\partial f}{\partial s} - \left(\eta_s \xi_{st} - \xi_s \Delta_\eta\right)\frac{\partial f}{\partial t} - \xi_t \eta_t \frac{\partial^2 f}{\partial s^2} + \left(\xi_t \eta_s + \eta_t \xi_s\right)\frac{\partial f}{\partial s \partial t} - \xi_s \eta_s \frac{\partial^2 f}{\partial s \partial t} \right]$$

$$\frac{\partial^2 f}{\partial \eta_2'} = \lambda_o^2 \left[\left(\xi_t \xi_{st} + \xi_t \Delta_\xi\right)\frac{\partial f}{\partial s} + \left(\xi_s \xi_{st} - \xi_s \Delta_\xi\right)\frac{\partial f}{\partial t} + \xi_t^2 \frac{\partial f}{\partial s^2} - 2\xi_s \xi_t \frac{\partial^2 f}{\partial t^2} + \xi_s^2 \frac{\partial^2 f}{\partial t^2} \right]$$

where

$$\lambda_o = \frac{1}{\left(\xi_s \eta_t - \xi_t \eta_s\right)}$$

$$\Delta_\eta = \lambda_o \left[2\eta_t \eta_s \xi_{st} - \left(\eta_t \xi_s + \eta_s \xi_t\right)\eta_{st} \right]$$

$$\Delta_\xi = -\lambda_o \left[2\xi_t \xi_s \eta_{st} - \left(\eta_t \xi_s + \eta_s \xi_t\right)\xi_{st} \right]$$

$$(\xi_s, \eta_s, 0) = T\vec{Q}_s \quad (\xi_t, \eta_s, 0) = T\vec{Q}_t \quad (\xi_{st}, \eta_{st}, 0) = T\vec{Q}_{st}$$

Now note from equation (30) that at $s = t = 0$,

$$\begin{aligned} \frac{\partial \mu}{\partial s} &= -1/2\,\mu_6 + 1/2\,\mu_8 \\ \frac{\partial \mu}{\partial t} &= 1/2\,\mu_5 - 1/2\,\mu_7 \\ \frac{\partial^2 \mu}{\partial s^2} &= \mu_6 + \mu_8 - 2\mu_9 \\ \frac{\partial^2 f}{\partial s\,\partial t} &= 1/4\left[\mu_1 - \mu_2 + \mu_3 - \mu_4\right] \\ \frac{\partial^2 f}{\partial t^2} &= \mu_5 + \mu_7 - 2\mu_9 \end{aligned} \qquad \text{(D.23)}$$

so that upon combining (D.22) and (D.23), $\mu_0, \mu_\xi, \mu_\eta, \mu_{\xi\xi}, \mu_{\xi\eta}, \mu_{\eta\eta}$ may be expressed in terms of the nine canonical panel doublet values μ_i, and the result substituted into (D.19) and (D.21). For the source distribution of equations (D.18) and (D.20) we assume $\sigma(\xi,\eta) = \sigma + \sigma_\xi \xi' + \sigma_\eta \eta'$ from the beginning and determine $\sigma_0, \sigma_\xi, \sigma_\eta$ by the process of least squares (ref. 14). The resultant integrals are evaluated in the same manner as for (ref. 14).

The line vortex term of equation (D.9) may be evaluated directly. Without loss of generality we assume the panel edge corresponds to t = -1 in figure A.1. Then

$$\vec{R} = \vec{R}_o - s\vec{R}_s$$

where

$$\vec{R}_o = \vec{P} - \vec{Q}_7 \ , \ \vec{R}_s = 1/2 \ (\vec{Q}_4 - \vec{Q}_3) \tag{D.24}$$

also

$$d\vec{\ell} = \vec{R}_s \, ds$$

Hence

$$\vec{V}_d = \frac{\beta^2}{4\pi} \vec{R}_o \otimes \vec{R}_s \, f \ , \quad f = \int_{-1}^{1} \frac{\mu(s) \, ds}{R^3} \tag{D.25}$$

To evaluate f we note that

$$\mu(s) = \mu_7 + \mu \, 1/2(\mu_4 - \mu_3)s + 1/2(\mu_4 + \mu_3 - 2\mu_7)s^2 \tag{D.26}$$

and

$$R(s) = \sqrt{a + 2bs + cs^2}$$

where

$$a = \vec{R}_o^T A \vec{R}_o, \quad b = -\vec{R}_o^T A \vec{R}_s, \quad c = \vec{R}_s^T A \vec{R}_s$$

Thus we need to compute H(1,3), H(2,3), H(3,3), where

$$H(M,K) = \int_{-1}^{1} \frac{s^{M-1}}{R^K} \, ds \tag{D.27}$$

We obtain from integral tables

$$H\ (1,3) = \frac{1}{cg^2}\ \left[\ cE\ (2,1) + bE\ (1,1)\right] \tag{D.28}$$

where

$$g^2 = a - \frac{b^2}{c} \qquad \text{and} \qquad E\ (M,K) = \frac{s^{M-1}}{R^K}\Bigg|_{-1}^{1}$$

Then

$$H\ (2,3) = -\frac{1}{c}\left[\ bH\ (1,3) + E\ (1,1)\right] \tag{D.29}$$

and

$$H\ (3,3) = \frac{1}{c}\ \left[H(1,1) - aH(1,3) - 2bH(2,3)\right] \tag{D.30}$$

where

$$H\ (1,1) = \frac{1}{\sqrt{c}}\ \log\left(\frac{R_2 + \ell_2}{R_1 + \ell_1}\right) \qquad \ell_1,\ \ell_2 > 0$$

$$= \frac{1}{\sqrt{c}} \log\left(\frac{R_1 - \ell_1}{R_2 - \ell_2}\right) \qquad \ell_1,\ \ell_2 < 0$$

$$= \frac{1}{\sqrt{c}} \log\left(\frac{(R_1 - \ell_1)(R_2 + \ell_2)}{g^2}\right) \qquad \ell_2 \geq 0,\ \ell_1 < 0 \tag{D.31}$$

and

$$\ell = \frac{(cs + b)}{\sqrt{c}}$$

Appendix E

Schemes to Construct the Outer Spline for Doublet Analysis (2), Doublet Design Type I (4) and Type II (6), Doublet Wake Type I (8), Type II (14), Type III (16), Type IV (10)

The outer spline gives the relation between the doublet strength at 9 canonical points on a Hyperbolic Paraboloid element (panel) and the neighboring singularity parameters. For each canonical point, a local tangent plane coordinate system (ξ, η) is set up with the given canonical point as the origin. Then a quadratic function

$$f(\xi,\eta) = a_0 + a_1\xi + a_2\eta + \frac{1}{2} a_3 \xi^2 + a_4\xi\eta + \frac{1}{2} a_5 \eta^2 \qquad (E.1)$$

is fitted (least squares) through the projections of some selected neighboring points where singularity parameters are specified. The coefficients a_0 gives the desired relationship of the doublet strength at the given canonical point in terms of the neighboring singularity parameters. For the 9 canonical points on a H-P element, we have 9 such coefficients a_0's which define the outer spline for a given panel.

In the following, we will discuss schemes to construct the outer spline for various types of doublet singularity networks.

For a given panel of a network, the 9 canonical points consists of panel corner points, midpoint of panel edges, center of panel. We will show how the doublet strength at each of these locations depends on the neighboring singularity parameters

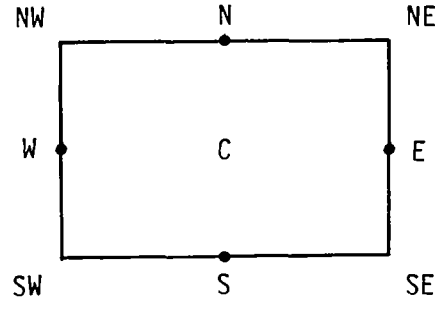

Figure E.1 The 9 Canonical Panel Points

Doublet/Analysis (NT = 2)

For doublet/analysis network, the singularity parameters λ's are specified at the locations as illustrated below.

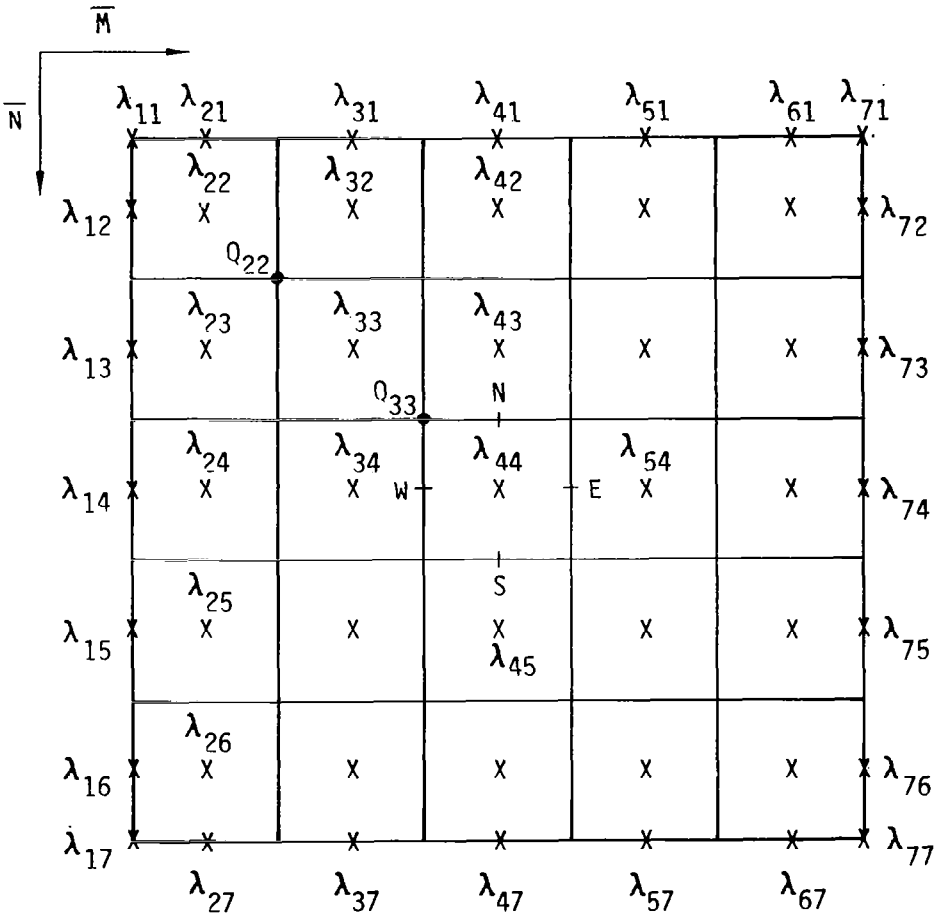

Figure E.2 Doublet/Analysis (2) Network

(E2-1) For network edge grid points, the associated doublet strength is assumed to depend only on the network edge singularity parameters. The network edges are parametrized by arc length t. A least squares fit of the function $f(t) = a + bt + ct^2$ through the four neighboring singularity parameters locations with two on each side of a given edge grid point yields the dependence of the doublet strength at the given point on the neighboring singularity parameters. Constraints are to be set on the two close singularity parameter locations.

(E2-2) For network edge midpoints, the value of the specified singularity parameter defines the doublet strength at each midpoint.

(E2-3) For each interior grid point, the quadratic function $f(\xi, \eta)$ is fitted (least squares) through the 12 neighboring points (its projections on the tangent plane with the grid point as origin) where singularity parameters are specified. A constrained least squares fit will be performed with constraints set at the 4 center points of these panels having the given grid point as their common corner point. It means that 4 equations corresponding to those 4 center points will be satisifed exactly in solving the least squares problem.

e.g., Q_{22} shown in Fig. E.2, a quadratic function will be fitted (least squares) through the 12 neighboring points where λ_{21}, λ_{31}, λ_{12}, λ_{22}, λ_{32}, λ_{42}, λ_{13}, λ_{23}, λ_{33}, λ_{43}, λ_{24}, λ_{34}, are specified with constraints at the 4 center points having λ_{22}, λ_{32}, λ_{23}, λ_{33}, as the associated singularity parameters.

(E2-4) For each interior edge midpoint, the quadratic function $f(\xi, \eta)$ is fitted through the 12 immediate neighboring points where the singularity parameters are specified. Again, a constrained least squares fit will be performed with constraints set at the center points of the two panels sharing an edge on which the given midpoints is located.

e.g., N shown in Fig. E.2, a least squares quadratic function will be fitted thru 12 neighboring points where λ_{32}, λ_{42}, λ_{52}, λ_{33}, λ_{43}, λ_{53}, λ_{34}, λ_{44}, λ_{54}, λ_{35}, λ_{45}, $_{55}$ are specified with constraints at the 2 center points with the associated singularity parameters λ_{43}, λ_{44} also for W shown in Fig. E.2, the 12 neighboring points are locations where λ_{23}, λ_{33}, λ_{43}, λ_{53}, λ_{24}, λ_{34}, λ_{44}, λ_{54}, λ_{25}, λ_{35}, λ_{45}, λ_{55}, are specified. The points where λ_{34} and λ_{44} are specified will be the locations for setting the constraints.

(E2-5) For panel center points, the value of the specified singularity parameters defines the double strength at each center points.

The following table gives the dependence of each canonical point of a given panel on the 21 neighboring singularity parameter (see the panel marked with C, N, S, W, E in Fig. E.2).

	λ_{32}	λ_{42}	λ_{52}	λ_{23}	λ_{33}	λ_{43}	λ_{53}	λ_{63}	λ_{24}	λ_{34}	λ_{44}	λ_{54}	λ_{64}	λ_{25}	λ_{35}	λ_{45}	λ_{55}	λ_{65}	λ_{36}	λ_{46}	λ_{56}
NW	X	X		X	Ⓧ	Ⓧ	X		X	Ⓧ	Ⓧ	X			X	X					
SW					X	X			X	Ⓧ	Ⓧ	X		X	Ⓧ	Ⓧ	X		X	X	
SE						X	X			X	Ⓧ	Ⓧ	X		X	Ⓧ	Ⓧ	X		X	X
NE		X	X		X	Ⓧ	Ⓧ	X		X	Ⓧ	Ⓧ	X			X	X				
W				X	X	X	X		X	Ⓧ	Ⓧ	X		X	X	X	X				
S					X	X	X			X	Ⓧ	X			X	Ⓧ	X		X	X	X
E					X	X	X	X		X	Ⓧ	Ⓧ	X		X	X	X	X			
N	X	X	X		X	Ⓧ	X			X	Ⓧ	X			X	X	X				
C											Ⓧ										

Ⓧ indicates the constraints

Doublet/Design Type I (NT = 4)

For each Doublet/Design network (Type I), the singularity parameters λ's are specified at the locations as illustrated below.

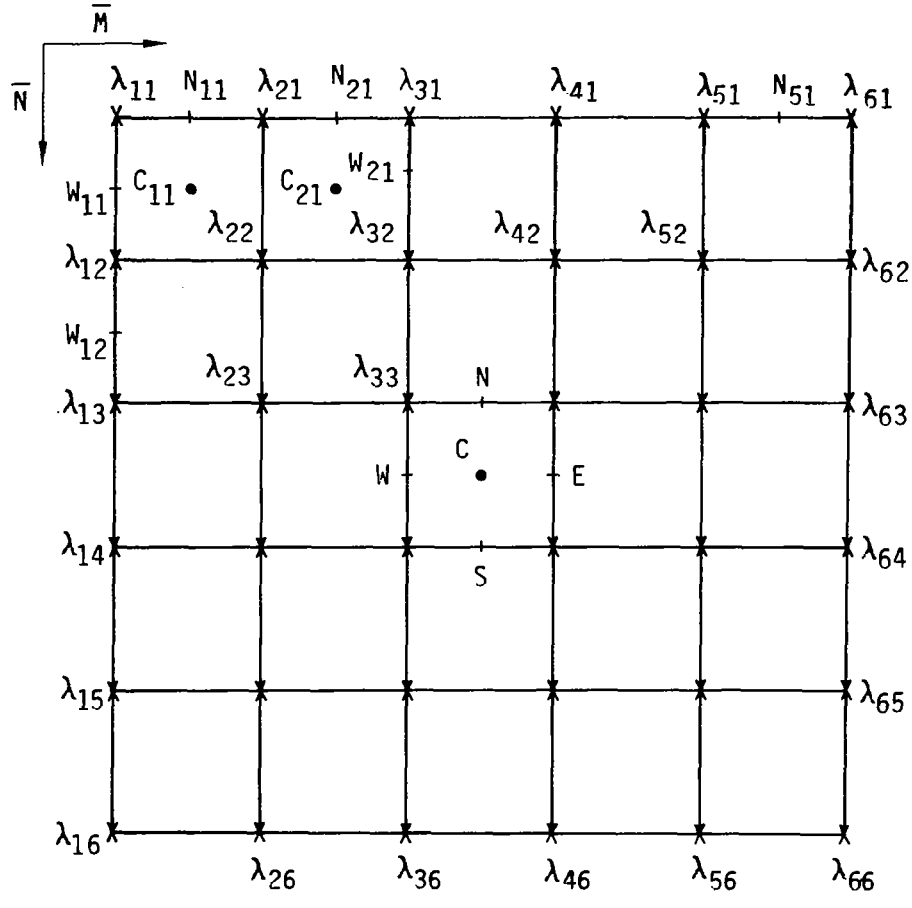

Fig. E.3 Doublet/Design Type I (4) Network

(E4-1) For network edge grid points, the value of the specified singularity parameters defines the doublet strength at each grid point.

(E4-2) For network edge midpoints, the associated doublet strength is assumed to depend only on the network edge singularity parameters. The network edges are parametrized by the length t. A least squares fit of the function $f(t) = a + bt + ct^2$ through the four neighboring singularity parameters locations with two on each side of a given midpoint yields the dependence of the doublet strength at the given point in the neighboring singularity parameters. Constraints are to be set on the two close singularity parameters.

e.g., for N_{21} in Fig. E.3, the four grid points where λ_{11}, λ_{21}, λ_{31}, λ_{41}, are specified will be used in the least squares fit with constraints set at grid points where λ_{21} and λ_{31} are specified.

For special case such as N_{11} shown in Fig. E.3, the corner point where λ_{11} is specified will be treated as two separate but identical points. Likewise for the midpoint N_{51}, the corner point where λ_{61} is specified will be treated as two separate but identical points.

(E4-3) For interior grid points, the value of the specified singularity parameters defines the doublet strength at each grid point.

(E4-4) For each interior edge midpoint, the quadratic function $f(\xi, \eta)$ is fitted through the 12 immediate neighboring grid points where the singularity parameters are specified. A constrained least squares fit will be performed with constraints set at the two grid points which are vertices of the edge containing the given midpoint.

e.g., for N in Fig. E.3, the grid points λ_{22}, λ_{32}, λ_{42}, λ_{52}, λ_{23}, λ_{33}, λ_{43}, λ_{53}, λ_{24}, λ_{34}, λ_{44}, λ_{54} are specified will be used in the least squares fit with constraints set at grid points where λ_{33} and λ_{43} are specified.

Again for special cases such as W_{21} shown in Fig. E.3, each of those three grid points where λ_{11}, λ_{21}, λ_{31} are specified will be treated as two separate but identical points.

(E4-5) For each panel center point, the quadratic function (ξ, η) is fitted through the 16 neighboring grid points where the singularity parameters are specified. A constrained least squares fit will be

performed with constraints set at the four corner points of the panel of which the given center point belongs.

e.g., for C in Fig. E.3, the 16 neighboring grid points where λ_{22}, λ_{32}, λ_{42}, λ_{52}, λ_{23}, λ_{33}, λ_{43}, λ_{53}, λ_{24}, λ_{34}, λ_{44}, λ_{54}, λ_{25}, λ_{35}, λ_{45}, λ_{55} are specified will be used in the least squares fit with constraints setting at four corner points where λ_{33}, λ_{43}, λ_{34}, λ_{44} are specified.

For special case such as C_{11} shown in Fig. E.3, each of those grid points where λ_{21}, λ_{31}, λ_{12}, λ_{13} are specified will be treated as two separate but identical points and the corner point where λ_{11} is specified will be treated as two separate but identical points. Similarly for C_{21} shown in Fig. E.3, each of those grid points where λ_{11}, λ_{21}, λ_{31}, λ_{41} are specified will be treated as two separate but identical points.

The following table gives the dependence of each canonical point of a given panel on the 16 neighboring singularity parameters (see the panel marked with C, N, S, W, E in Fig. E.3).

	λ_{22}	λ_{32}	λ_{42}	λ_{52}	λ_{23}	λ_{33}	λ_{43}	λ_{53}	λ_{24}	λ_{34}	λ_{44}	λ_{54}	λ_{25}	λ_{35}	λ_{45}	λ_{55}
NW						Ⓧ										
SW										Ⓧ						
SE											Ⓧ					
NE							Ⓧ									
W	X	X	X		X	Ⓧ	X		X	Ⓧ	X		X	X	X	
S					X	X	X	X	X	Ⓧ	Ⓧ	X	X	X	X	X
E		X	X	X		X	Ⓧ	X		X	Ⓧ	X		X	X	X
N	X	X	X	X	X	Ⓧ	Ⓧ	X	X	X		X	X			
C	X	X	X	X	X	Ⓧ	Ⓧ	X	X	Ⓧ	Ⓧ	X	X	X	X	X

Ⓧ indicates the constraints

Doublet/Design Type II (NT = 6)

The singularity parameters λ 's of a doublet/design Type II network are specified at the locations as illustrated on the this page.

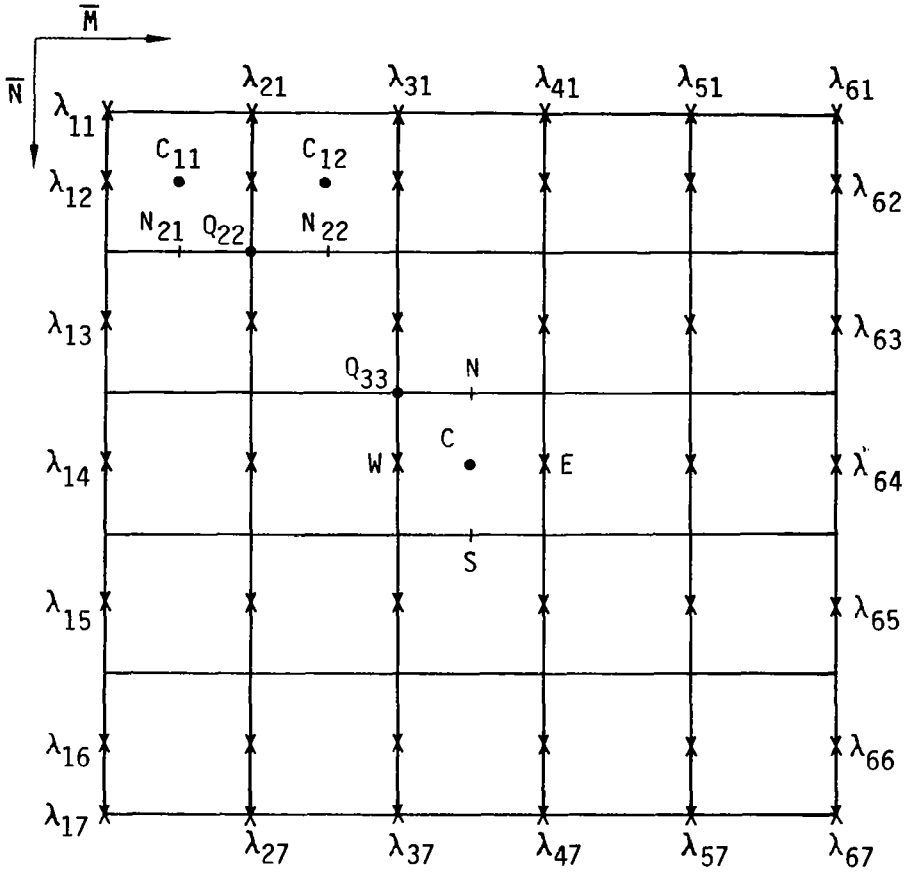

Figure E.4 Doublet/Design Type II (6) Network

(E6-1) For network edge grid points lying on the edge with singularity parameters specified at grid points, the doublet strength are simply the values of singularity parameters as for network edge grid points lying on the edge with singularity parameters specified at edge midpoints and two extreme corner points, the doublet strength are to be found by using the Doublet/Analysis approach (see (E2-1).

(E6-2) For network edge midpoints lying on the edge with singularity parameters specified at grid points, the doublet strengths are to be found by using the Doublet/Design Type I approach (see (E4-2).

For network edge midpoints lying on the edge with singularity parameters specified at edge midpoints and two extreme corner points, the doublet strengths ar simply the value of singularity parameters.

(E6-3) For each interior grid point, the quadratic function (ξ, η) is fitted through the 12 neighboring points where singularity parameters are specified. A constrained least squares fit will be performed with constraints setting at the two edge midpoints which are on the two edges having the given grid point as their common vortex,

e.g., for Q_{33} shown in Fig. E.4, the locations where λ_{22}, λ_{32}, λ_{42}, λ_{23}, λ_{33}, λ_{43}, λ_{24}, λ_{34}, λ_{44}, λ_{25}, λ_{35}, λ_{45} are specified will be used in the least squares fit with constraints set at edge midpoints where λ_{33}, λ_{34} are specified.

For these interior grid points lying on the columns next to the first or last column, those network edge grid points will be used in the least squares fit.

e.g., for Q_{22} shown in Fig. E.4, the edge grid points where λ_{11}, λ_{21}, λ_{31} are specified will be used in conjunction with those edge midpoints where λ_{12}, λ_{22}, λ_{32}, λ_{13}, λ_{23}, λ_{33}, λ_{14}, λ_{24}, λ_{34} are specified.

(E6-4) For the interior midpoints lying on rows of the network, the doublet strengths are simply the values of the specified singularity parameters.

For an interior midpoint lying on columns of the network the quadratic function $f(\xi, \eta)$ is fitted through the 16 neighboring locations where the singularity parameters are specified. A constrained least squares fit will be performed with constraints setting at the four edge midpoints belonging to the two panels both having the given point as their common edge midpoints.

e.g., for N shown in Figure E.4, the locations where λ_{22}, λ_{32}, λ_{42}, λ_{52}, λ_{23}, λ_{33}, λ_{43}, λ_{53}, λ_{24}, λ_{34}, λ_{44}, λ_{54}, λ_{25}, λ_{35}, λ_{45}, λ_{55} are specified will be used in the least squares fit with constraints set at the four edge midpoints where λ_{33}, λ_{43}, λ_{34}, λ_{44} are specified.

For those edge midpoints lying on the columns next to the first or last columns, the network edge grid points will be used in the least squares fit, e.g., for N_{22} shown in Figure E.4, the four edge grid points, where λ_{11}, λ_{21}, λ_{31}, λ_{41} are specified will be used in conjunction with those edge midpoints where λ_{12}, λ_{22}, λ_{32}, λ_{42}, λ_{13}, λ_{23}, λ_{33}, λ_{43}, λ_{14}, λ_{24}, λ_{34}, λ_{44} are specified. In this case, the constraints will be set at the four edge midpoints where λ_{22}, λ_{32}, λ_{23}, λ_{33} are specified.

Special case such as the interior midpoints lying on the corner panels, each of the locations along the network edge where the singularity parameters are specified will be treated as two separate but identical points.

e.g., for N_{12} shown in Figure E.4, the locations where λ_{11}, λ_{12}, λ_{13}, λ_{14} are specified will be counted as twice in the formulation of the least squares problem.

(E6-5) For each panel center point, the quadratic function $f(\xi, \eta)$ is fitted through the 12 immediate neighboring locations where the singularity parameters are specified. A constrained least squares fit will be performed with constraints set on the two edge midpoints on the same panel that the given center point belongs to.

e.g., for C in Figure E.4, the locations where λ_{23}, λ_{33}, λ_{43}, λ_{53}, λ_{24}, λ_{34}, λ_{44}, λ_{54}, λ_{25}, λ_{35}, λ_{45}, λ_{55} are specified will be used in the least squares fit with constraints setting at the two edge midponts where λ_{34}, λ_{44} are specified.

For these center points lying on the first or last column panels, the network edge grid points will be used in the least squares fit.

e.g., C_{21} in Figure 4, the network edge grid points, where λ_{11}, λ_{21}, λ_{31}, λ_{41} are specified will be used in conjunction with the edge midpoints, where λ_{12}, λ_{22}, λ_{32}, λ_{42}, λ_{13}, λ_{23}, λ_{33}, λ_{43} are specified.

Again special case such as those center points lying on the corner panels, each of the locations along the network edge where the singularity parameters are specified will be treated as two separate but identical points.

e.g., for C_{11} in Figure E.4, the locations where λ_{11}, λ_{12}, λ_{13}, λ_{14} are specified will be counted as twice in the formulation of the least squares problem.

The following table gives the dependence of each canonical point of a given panel on the 20 neighboring singularity parameters (see the panel marked with C,N,W,S,E in Figure E.4).

	λ_{22}	λ_{32}	λ_{42}	λ_{52}	λ_{23}	λ_{33}	λ_{43}	λ_{53}	λ_{24}	λ_{34}	λ_{44}	λ_{54}	λ_{25}	λ_{35}	λ_{45}	λ_{55}	λ_{26}	λ_{36}	λ_{46}	λ_{56}
NW	X	X	X		X	Ⓧ	X		X	Ⓧ	X		X	X	X					
SW					X	X	X		X	Ⓧ	X		X	Ⓧ	X		X	X	X	
SE						X	X	X		X	Ⓧ	X		X	Ⓧ	X		X	X	X
NE		X	X	X		X	Ⓧ	X		X	Ⓧ	X		X	X	X				
W										Ⓧ										
S					X	X	X	X	X	Ⓧ	Ⓧ	X	X	Ⓧ	Ⓧ	X	X	X	X	X
E										Ⓧ										
N	X	X	X	X	X	Ⓧ	Ⓧ	X	Ⓧ	Ⓧ	X	X	X	X	X	X				
C					X	X	X	X	Ⓧ	Ⓧ	X	X	X	X	X	X				

Ⓧ indicates the constraints

Doublet/Wake Type I (8)

The singularity parameters are specified at the locations as illustrated below.

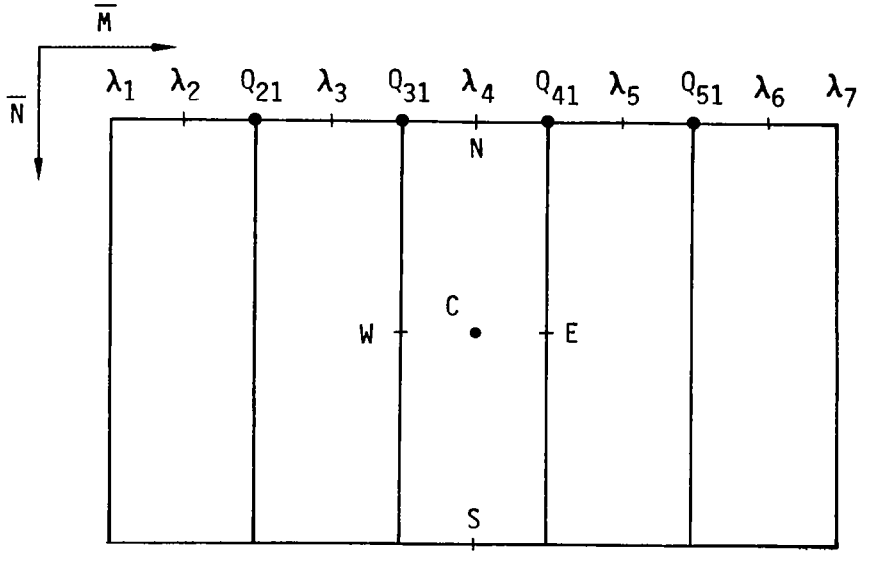

Figure E.5 Doublet/Wake Type I (8) Network

First one computes the values of doublet strength at network edge grid points using Doublet/Analysis approach (see (E2-1). With the assumption of constant singularity strength along the streamwise direction, we define $\mu_{NW} = \mu_W = \mu_{SW} = \mu(Q_{i1})$, $\mu_N = \mu_C = \mu_S = \mu_{i+1}$ and $\mu_{NE} = \mu_E = \mu_{SE} = \mu(Q_{i+1})$ where $\mu(Q_{i1})$ and $\mu(Q_{i+1,1})$ are values of doublet strength at edge grid points Q_{i1} and $Q_{i+1,1}$. The exceptions to the above definition are $\mu_{NW} = \mu_W = \mu_{SW} = \lambda_1$ for the first panel and $\mu_{NW} = \mu_E = \mu_{SE} = \gamma$ for the last panel as illustrated in Figure E.5.

Doublet/Wake Type II (14)

The singularity parameters are specified at the locations as illustrated below.

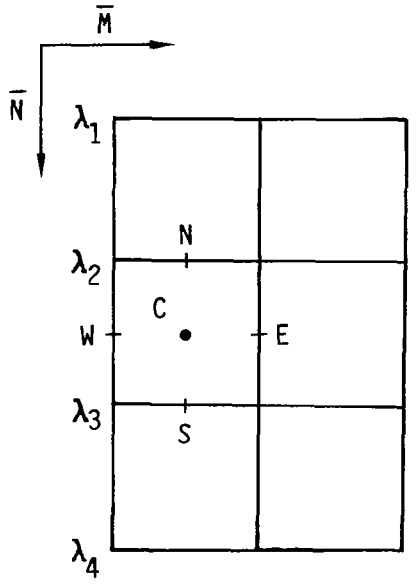

Figure E.6 Doublet/Wake Type II (14) Network

This type of network is used for fed sheet. Similar to Doublet/Design network, the values of the specified singularity parameters define the doublet strength at edge grid points. The values of doublet strength at edge mid points are computed using Doublet/Design approach (see (E4-2). With the assumption of constant singularity strength along the chordwise direction, (row M), we define $\mu_{NW} = \mu_N = \mu_{NE} = \lambda_i$, $\mu_W = \mu_C = \mu_E = \mu(M_i)$ and $\mu_{SW} = \mu_S = \mu_{SE} = \lambda_{i+1}$ where λ_i, λ_{i+1} are values of singularity parameters specified at grid point. Q_i, Q_{i+1} and M_i are edge midpoint on the edge joining Q_i and Q_{i+1}.

Again using the assumption of the constant doublet strength along chordwise direction, the singularity distributions on the panel at 2nd row will be same as those on the panel at 1st row.

Doublet/Wake Type III (16)

The singularity parameters are specified at the locations as illustrated below

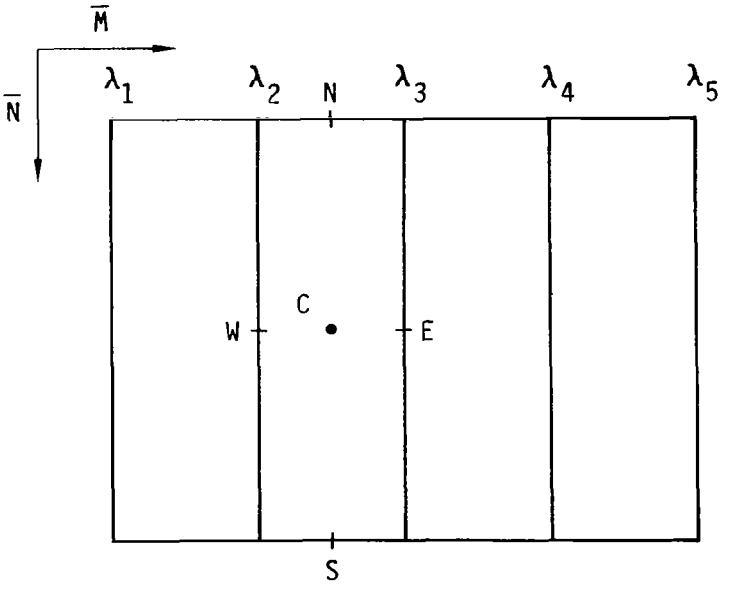

Figure E.7 Doublet/Wake III (16) Network

This type of network is identical to Doublet/Wake Type II (14) and is used mainly for wake network attached to Doublet/Design Network.

Same as Type II (14) network, the values of the specified singularity parameters define the doublet strength at edge grid points. The values of doublet strength at edge midpoints are computed using Doublet/Design approach (see (E4-2). With the assumption of constant singularity strength along the streamwise direction (row M), we define $\mu_{NW} = \mu_W = \mu_{SW} = \lambda_i$, $\mu_N = \mu_C = \mu_S = \mu(M_i)$ and $\mu_{NE} = \mu_E = \mu_{SE} = \lambda_{i+1}$ where λ_i, λ_{i+1} are values of singularity parameters specified at grid point. Q_i, Q_{i+1} and M_i are edge midpoint on the edge joining Q_i and Qi+1.

Doublet/Wake Type IV (10)

There is only one singularity parameter specified at the location shown below.

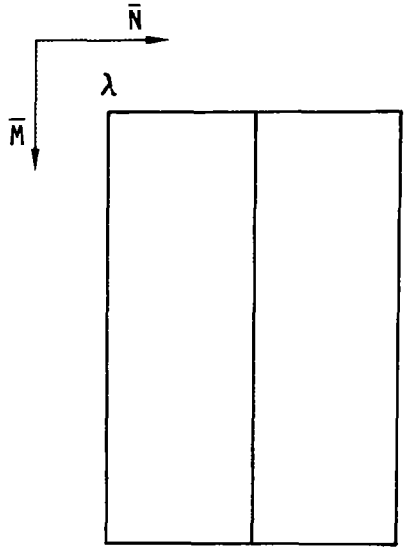

Figure E.8 Doublet/Wake Type (IV) (10) Network

The doublet strength is assumed to be constant over the whole network. The values of doublet strength at the 9 canonical points are all equal to the value of the specified singularity parameter λ .

Appendix F

Function Evaluation and Jacobian Formulation

Function Evaluation

The boundary conditions can be expressed symbolically in terms of the following equations:

$$F(\Lambda,\Theta,\lambda,\nu) = \begin{cases} W_n = 0 & \text{wing and body} \\ \Delta C_p = 0 & \text{Free sheet and wake} \\ \Delta\vec{\zeta}\cdot\hat{\ell} = 0 & \text{Kutta condition} \end{cases} \quad \text{(F.1)}$$

$$G(\Lambda,\Theta,\lambda,\nu) = W_n = 0 \qquad \text{Free sheet} \qquad \text{(F.2)}$$

$$H(\Lambda,\Theta,\lambda,\nu) = f = 0 \qquad \text{Fed sheet} \qquad \text{(F.3)}$$

Where Λ denotes the singularity (doublet and source) strength parameters, Θ represents the angle of inclination of panel edges in transverse cuts defining the spatial location of free sheet, and λ , ν are free geometry parameters controlling the shape of free and fed sheets.

The function F symbolizes the impermeability condition of wing and body, zero pressure jump of free sheet and wake, Kutta condition. The function G is the impermeability condition of free sheet. Finally the function H represents the global boundary condition of zero net force acting on the fed sheet and the line vortex. Each of these functions is evaluated in the following manner.

1. $W_n = \rho_\infty(\vec{V}_\infty + B\bar{V}_A)\cdot\hat{n}$ at a given control point (doublet network)

where $\vec{V}_\infty$ is the free stream velocity $\bar{V}_A$ is the average perturbation velocity at the control point induced by all panels, and $\hat{n}$ is the unit normal at the control point on the HP surface. The matrix B is defined by

$$B = I + (\beta^2 - 1)\,\hat{c}\,\hat{c}^T = \beta^2 A^{-1} \qquad \text{(F.4)}$$

where $\beta^2 = 1 - M_\infty^2$, $\hat{c}$ is the compressibility direction unit vector and $A = \beta^2 I + (1 - \beta^2)\hat{c}\,\hat{c}^T$. For a control point that

lies on a source network to satisfy the upper surface impermeability, we have instead the following expression

$$W_n = \rho_\infty(\bar{V}_\infty + B\bar{V}_A)\cdot\hat{n} + \frac{1}{2}\sigma\rho_\infty \qquad (F.5)$$

where σ is the source singularity strength.

2. $$\Delta C_p = -2(\bar{V}_\infty + B\bar{V}_A)\cdot(\hat{n}\otimes\bar{\nabla}\mu)\otimes\hat{n} \qquad (F.6)$$

where V_∞ , $\vec{V}_A$ and B are defined as before, and $\hat{n}\otimes\Delta\mu$ is evaluated as follows:

$$\hat{n}\otimes\nabla\mu = \frac{1}{|\bar{a}_s\otimes\bar{a}_t|}\left(\bar{a}_t\frac{\partial\mu}{\partial s} - \bar{a}_s\frac{\partial\mu}{\partial t}\right) \qquad (F.7)$$

The unit upper surface normal on the HP surface is given by

$$\hat{n} = \frac{\bar{a}_s\otimes\bar{a}_t}{|\bar{a}_s\otimes\bar{a}_t|}$$

3. The force across the fed sheet is calculated from equation (19) with $\sigma = 0$. We require that the two components normal to the core be zero. In each column of fed sheet panels to be specified we require that

$$f_{\nu_e} = \frac{1}{\mu_e}\hat{\nu}_e\cdot\left[-\iint_{S_c}\vec{w}_A\otimes\vec{\zeta}\,ds + \int_L \mu\ \vec{w}_A\otimes d\vec{\ell}\right] = 0$$
$$f_{n_e} = \frac{1}{\mu_e}\hat{n}_e\cdot\left[-\iint_{S}\vec{w}_A\otimes\vec{\zeta}\,ds + \int_L \mu\ \vec{w}_A\times d\vec{\ell}\right] = 0 \qquad (F.8)$$

where S is the panel column surface, L is the line segment comprising the edge of the panel column (corresponding to the core) and the subscript e denotes quantities evaluated at the midpoint of L. Here $\hat{w}_e$ is given by $\hat{\ell}_e\otimes\hat{n}_e$ where $\vec{\ell}_e = \ell_o\hat{\ell}_e$ is the vector line segment L. From equation (18) we have

$$-(\vec{w}_A\times\vec{\zeta}) = \Delta p\hat{n} + \frac{(\vec{w}_A\cdot\vec{n})(\vec{\zeta}\times\vec{n})}{(\hat{n}\cdot\vec{n})} \qquad (F.9)$$

For modest Mach numbers $\hat{n}_e\otimes\tilde{n}\approx 0.$; moreover by construction of the fed sheet doublet spline $\vec{\zeta}$ is approximately perpendicular to the core so that $\hat{\nu}_e\otimes\vec{\zeta}\approx 0$.

Hence

$$-\hat{\nu}_e \, (\vec{w}_A \otimes \vec{\zeta}) \approx \Delta\vec{p} \, \hat{\nu}_e \cdot \hat{n}$$

and

$$-\hat{n}_e \, (\vec{w}_A \otimes \vec{\zeta}) \approx \Delta p \, \hat{n}_e \cdot \hat{n} \tag{F.10}$$

Thus (F.8) is approximated by

$$f_{\nu_e} = \frac{1}{\mu_e} \hat{\nu}_e \left[\sum_{\substack{\text{Fed Sheet} \\ \text{Panel Column}}} \Delta P_i \, A_i \, \hat{n}_i + \mu_e \, w_A \otimes \vec{\ell}_e \right] = 0$$

$$f_{n_e} = \frac{1}{\mu_e} \hat{n}_e \left[\sum_{\substack{\text{Fed Sheet} \\ \text{Panel Column}}} \Delta P_i \, A_i \, \hat{n}_i + \mu_e \, w_A \otimes \vec{\ell}_e \right] = 0 \tag{F.11}$$

Here p_i is evaluated at center of the ith panel of the panel column and A is the area of the ith panel.

Jacobian Calculation

Taking the partial derivatives of the functions F, G and H with respect to the variables Λ , θ , λ and ν we have the Jacobian matrix

$$\begin{pmatrix} \frac{\partial W_n}{\partial \Lambda} & \frac{\partial W_n}{\partial \theta} & \frac{\partial W_n}{\partial \lambda} & \frac{\partial W_n}{\partial \nu} \\ \frac{\partial C_p}{\partial \Lambda} & \frac{\partial C_p}{\partial \theta} & \frac{\partial C_p}{\partial \lambda} & \frac{\partial C_p}{\partial \nu} \\ \frac{\partial W_{nk}}{\partial \Lambda} & \frac{\partial W_{nk}}{\partial \theta} & \frac{\partial W_{nk}}{\partial \lambda} & \frac{\partial W_{nk}}{\partial \nu} \\ \frac{\partial f}{\partial \Lambda} & \frac{\partial f}{\partial \theta} & \frac{\partial f}{\partial \lambda} & \frac{\partial f}{\partial \nu} \end{pmatrix} \tag{F.12}$$

This gives the variations of the boundary conditions due to the perturbation of singularity strength and geometry parameters

(1)

$$\frac{\partial W_n}{\partial \Lambda} = \frac{\partial(\vec{V}_\infty + B\vec{V}_A)\cdot\hat{n}}{\partial \Lambda} = B \frac{\partial \vec{V}_A}{\partial \Lambda} \cdot \bar{n} \tag{F.13}$$

For body-source network, $\dfrac{\partial W_n}{\partial \Lambda} = \dfrac{\partial\left[(\vec{V}_\infty + B\vec{V}_A)\cdot\hat{n} + 1/2\sigma\right]}{\partial \Lambda}$

$$= B\,\frac{\partial \vec{V}_A}{\partial \Lambda}\cdot\hat{n} + \frac{1}{2}\frac{\partial \sigma}{\partial \Lambda} \qquad (F.14)$$

(2)

$$\frac{\partial W_n}{\partial \Theta} = \frac{\partial(\vec{V}_\infty + B\vec{V}_A)\cdot\hat{n}}{\partial \Theta}\,, \quad \Theta = \theta,\lambda,\nu \qquad (F.15)$$

$$= B\,\frac{\partial \vec{V}_A}{\partial \Theta}\cdot\hat{n} + (\vec{V}_\infty + B\vec{V}_A)\cdot\frac{\partial \hat{n}}{\partial \Theta}$$

For body-source network,

$$\frac{\partial W}{\partial \Theta} = B\,\frac{\partial V_A}{\partial \Theta}\cdot\hat{n} + (\hat{V}+B\bar{V}_A) = \frac{\partial \hat{n}}{\partial \Theta} + \frac{1}{2}\frac{\partial \sigma}{\partial \Theta} \qquad (F.16)$$

(3)

$$\frac{\partial \Delta C_p}{\partial \Lambda} = \frac{\partial\left[-2(\vec{V}_\infty + B\vec{V}_A)\cdot((\hat{n}\otimes\nabla\mu)\otimes\hat{n})\right]}{\partial \Lambda} \qquad (F.17)$$

$$= -2B\,\frac{\partial \vec{V}_A}{\partial \Lambda}\cdot((\hat{n}\otimes\nabla\mu)\otimes\hat{n}) - 2(\vec{V}_\infty + B\vec{V}_A)\frac{\partial((\hat{n}\otimes\vec{\nabla}\mu)\otimes\hat{n})}{\partial \Lambda}$$

$$= -2B\,\frac{\partial \vec{V}_A}{\partial \Lambda}\cdot(\vec{\zeta}\otimes\hat{n}) + 2(\vec{V}_\infty + B\vec{V}_A)\cdot(\hat{n}\otimes\frac{\partial \vec{\zeta}}{\partial \Lambda})$$

(4)

$$\frac{\partial \Delta C_p}{\partial \Theta} = \frac{\partial\left\{-2(\vec{V}_\infty + B\vec{V}_A)\cdot((\bar{n}\otimes\bar{\nabla}\mu)\otimes\vec{n})\right\}}{\partial \Theta}\,, \quad \Theta = \theta,\lambda,\nu \qquad (F.18)$$

$$-2B\,\frac{\partial \vec{V}_A}{\partial \Theta}\cdot((\bar{n}\otimes\bar{\nabla}\mu)\otimes\hat{n}) - 2(\vec{V}_\infty + B\vec{V}_A)\cdot\frac{\partial((\vec{n}\otimes\vec{\ })\otimes\hat{n})}{\partial \Theta}$$

$$-2B\,\frac{\partial \vec{V}_A}{\partial \Theta}\cdot(\vec{\zeta}\otimes\hat{n}) - 2(\vec{V}_\infty + B\vec{V}_A)\cdot(\frac{\partial \vec{\zeta}}{\partial \Theta}\otimes\hat{n} + \vec{\zeta}\otimes\frac{\partial \hat{n}}{\partial \Theta}$$

(5)

$$\frac{\partial f}{\partial \Lambda} = \frac{\partial \vec{V}_e \cdot (\sum_i \vec{f}_i + \vec{f}_e)}{\partial \Lambda}$$

$$= \frac{\partial V_e}{\partial \Lambda} \cdot (\sum_i \vec{f}_i + \vec{f}_e) + V_e \cdot \left(\sum_i \frac{\partial \vec{f}_i}{\partial \Lambda} + \frac{\partial \vec{f}_e}{\partial \Lambda} \right) \quad \text{(F.19)}$$

where

$$\vec{V}_e = \begin{cases} \frac{1}{\mu_e} \hat{n}_e & \text{for } f_n \\ \frac{1}{\mu_e} \hat{\nu}_e & \text{for } f\nu \end{cases} \quad \text{(F.20)}$$

$$f_i = \Delta P_i A_i \hat{n}_i$$

$$f_e = \mu_e \vec{w} A_e \otimes \vec{\ell}_e \quad \text{(F.21)}$$

(6) and $\sum_i$ is a summation overall fed sheet network panels.

$$\frac{\partial f}{\partial \Theta} = \frac{\partial \vec{V}_e \cdot (\sum_i \vec{f}_i + \vec{f}_e)}{\partial \Theta} \qquad \Theta = \theta, \lambda, \nu \quad \text{(F.22)}$$

$$= \frac{\partial \vec{V}_e}{\partial \Theta} \cdot (\sum_i \vec{f}_i + \vec{f}_e) + \vec{V}_e \cdot (\sum_i \frac{\partial f_i}{\partial \Theta} + \frac{\partial f_e}{\partial \Theta})$$

where $\bar{V}$, f_i and f_e are defined as above.

Appendix G

Quasi-Newton Scheme

Denote all geometry degrees of freedom by the vector Θ and all the singularity parameters by Λ. The boundary conditions determining the singularity strength are given by equation set F.1. Denote the set by

$$F(\Lambda,\Theta) = 0 \tag{G.1}$$

Equations F.2 and F.3 determine the geometric degrees of freedom. Denote this set by

$$G(\Lambda,\Theta) = 0 \tag{G.2}$$

Small perturbation of equations G.1 and G.2 from the initial "starting solution" result in a set of linear equations governing the perturbation variables Λ, Θ.

$$\begin{pmatrix} \frac{\partial F}{\partial \lambda} & \frac{\partial F}{\partial \Theta} \\ \frac{\partial G}{\partial \lambda} & \frac{\partial G}{\partial \Theta} \end{pmatrix} \begin{pmatrix} \Delta\Lambda \\ \Delta\Theta \end{pmatrix} = -\begin{pmatrix} F \\ G \end{pmatrix} \tag{G.3}$$

The perturbation quantities in equation G.3 are denoted symbolically as ΔX, the coefficient matrix (Jacobian) as J, and the right-hand side as $-f$. Equation (G.3) becomes

$$J\Delta X = -f \tag{G.4}$$

The set of equation G.1 and G.2 is solved iteratively with a Quasi-Newton scheme. Represent the ith iteration by superscript i. The scheme proceeds to find the corrections $\Delta X^{(i)}$ from the equation

$$J^{(i)}\,\Delta X^{(i)} = -f^{(i)} \tag{G.5}$$

and forms the new approximate solution (termed the next iterate)

$$X^{(i+1)} = X^{(i)} + \delta^{(i)}\,\Delta X^{(i)} \tag{G.6}$$

where $J(i) = J(X(i))$, $f(i) = f(X(i))$, and $\delta(i)$ is a scaling parameter to limit the step size of the correction vector. The Jacobian at $X^{(i+1)}$ is obtained by using the following update formula (reference 38)

$$J^{(i+1)} \approx J^{(i)} + D^{(i)} \tag{G.7}$$

where

$$D^{(i)} = \frac{\left\{f^{(i+1)} - f^{(i)} - J^{(i)}\Delta X^{(i)}\right\}\Delta X^{(i)\,T}}{\Delta X^{(i)T}\,\Delta X^{(i)}} \tag{G.8}$$

In this way, there is no need to reevaluate the partial derivatives comprising the elements of the Jacobian at each iteration. The superscript T denote the transpose of a vector. The aerodynamic influence coefficients which are changed by the geometry update are recalculated every iteration.

The scaling parameter $\delta^{(i)}$ is introduced to alleviate the problem of overshoot in the classical Newton scheme. For each iteration cycle, the following criteria are used to determine $\delta^{(i)}$:

$$0 \leq \delta^{(i)} \leq 1 \tag{G.9}$$

and

$$\delta^{(i)} \left|\Delta\Theta^{(i)}\right| \leq \gamma \tag{G.10}$$

where γ is a predetermined quantity chosen to limit the maximum correction for the panel orientation angles (10 degrees in the code). In addition, a halving process of the scaling parameter $\delta^{(i)}$ is applied to ensure the inequality

$$\|f^{(i+1)}\| < \|f^{(i)}\| \tag{G.11}$$

where $\|\ \|$ is the Euclidean norm representing the length of a vector.

This halving process is performed repeatedly until either the criterion in equation G.11 is satisfied or three cycles of the step size reduction (i.e., three halvings) are completed. The quality of the solution is monitored by examination of the sum of squares of residuals defined by

$$R^2 = \|F\|^2 + \|G\|^2 \qquad (G.12)$$

To initiate the solution process, an initial geometry is required. The size of the fed sheet and the initial free sheet geometry are taken from Smith's conical flow solutions or, as experience allows, by assuming an initial geometry.

REFERENCES

1. Maskell, E. C., "Some Recent Developments in the Study of Edge Vortices," Proceedings of 3rd Congress of Int. Counc. Aero. Sci., 1962, pp 737-749, Spartan Books, Inc. Washington, 1964.

2. Peckham, D. H., "Low-Speed Wind-Tunnel Tests on a Series of Uncambered Slender Pointed Wings with Sharp Edges,: RM 3186, British Aeronautical Research Council, 1961.

3. Polhamus, E. C., "Predictions of Vortex-Lift Characteristics by a Leading-Edge Suction Analogy," J. of Aircraft, Vol. 8, p. 193, 1971.

4. Polhamus, E. C., "A Concept of the Vortex Lift of Sharp-Edge Delta Wings Based on a Leading-Edge-Suction Analogy," NASA TN D-3767, December 1966.

5. Polhamus, E. C., "Application of the Leading-Edge-Suction Analogy of Vortex Lift to the Drag-Due-to-Lift of Sharp-Edge Delta Wings," NASA TN D-4739, August 1968.

6. Smith, J. H. B., "Improved Calculations of Leading-Edge Separation from Slender Delta Wings," RAE Tech. Report 66070, March 1966.

7. Mangler, K. W. and Smith, J. H. B., "A Theory of the Flow Past a Slender Delta Wing with Leading-Edge Separation," Proc. Roy. Soc., May 1959.

8. Nangia, R. K. and Hancock, G. J., "A Theoretical Investigation for Delta Wings with Leading-Edge Separation at Low Speeds," ARC CP 1086, 1968.

9. White, R. P. Jr., "Wing-Vortex Lift at High Angles of Attack," AGARD-CP-204, Sept. 1976.

10. Kandil, O. A., Mook, D. T., and Nayfeh, A. H., "Nonlinear Prediction of the Aerodynamic Loads on Lifting Surfaces," J. of Aircraft 13, pp 22-28, 1976.

11. Rehbach, C., "Etude Numerique de Nappes Turbillonaires Issues D Une Ligne de Decollement Pres du Bord d Attaque," Rech. Aero. 1973-6, pp 325-330, 1973.

12. Kandil, O. A., Mook, D. T. and Nayfeh, A. H., "A Numerical Technique for Computing Subsonic Flow Past Three-Dimensional Canard-Wing Configurations with Edge Separations," AIAA Paper 77-1, 1977.

13. Kandil, O. A., Atta, E. H., and Nayfeh, A. H., "Three Dimensional Steady and Unsteady Asymmetric Flow Past Wings of Arbitrary Planforms," AGARD-CP-227, September 1977.

14. Weber, J. A., Brune, G. W., Johnson, F. T., Lu, P., and Rubbert, P. E., "Three-Dimensional Solution of Flows over Wings with Leading Edge Vortex Separation," AIAA Journal 14, pp 519-525, 1976, also NASA CR 132709 and 132710, 1975.

15. Johnson, F. T., Lu, P., Brune, G. W., Weber, J. A., and Rubbert, P. E., "An Improved Method for the Prediction of Completely Three-Dimensional Aerodynamic Load Distributions on Configurations with Leading-Edge Separtion," AIAA Paper 76-417, 1976.

16. Hoeijmakers, H. W. M. and Bennekers, B., "A Computational Method for the Calculation of the Flow about Wings with Leading-Edge Vortices," Paper No. 25, AGARD-CP-247, January 1979.

17. Smith, J. H. B., "Inviscid Fluid Models, Based on Rolled-Up Vortex Sheets, for Three-Dimensional Separation at High Reynolds Number," Paper No. 9, AGARD Lecture Series No. 94 on Three-Dimensional and Unsteady Separation at High Reynolds Numbers, February, 1978.

18. Kuhlman, John M., "Analytical Studies of Separated Vortex Flow on Highly Swept Wings," NASA CR-3022, November 1978.

19. Brune, G. W. and Rubbert, P. E., "Boundary-Value Problem of Configurations with Compressible Free Vortex Flow," AIAA Journal, Vol. 15, No. 10, pp. 1521-1523, October 1977,

20. Kellogg, O. D., "Foundations of Potential Theory," Dover Publishing Company, New York, 1953.

21. Lamb, H. "Hydrodynamics," Dover Publishing Company, New York, 1945.

22. Johnson, F. T., Ehlers, F. E. and Rubbert, P. E., "A Higher Order Panel Method for General Analysis and Design Applications in Subsonic Flows," Proceedings of the Fifth International Conference on Numerical Methods in Fluid Dynamics, Enschede, The Netherlands, June 28, 1976.

23. Johnson, F. T., and Rubbert, P. E., "Advanced Panel-Type Influence Coefficient Methods Applied to Subsonic Flows," AIAA Paper 75-50, AIAA 13th Aerospace Sciences Meeting, January 1975.

24. Hess, J., Johnson, F. T., and Rubbert, P. E., "Panel Methods Lecture Notebook," pp. 3-20 to 3-28, AIAA Short Course on Panel Methods, July 1978.

25. Morino, L., Chen, L., and Suciu, E. O., "Steady and Oscillatory Subsonic and Supersonic Aerodynamics around Complex Configurations," AIAA Journal, Vol. 13, No. 3, pp. 368-374, March 1975.

26. Tinoco, E. N. and Yoshihara, H., "Subcritical Drag Minimization for Highly Swept Wings with Leading Edge Vortices," Paper No. 26, AGARD-CP-247, January 1979.

27. Wentz, W. H., "Effects of Leading-Edge Camber on Low-Speed Characteristics of Slender Delta Wings," NASA CR-2002, 1972.

28. Kirkpatrick, D. L. I., "Analysis of the Static Pressure Distribution on a Delta Wing in Subsonic Flow," A.R.C. RM 3619, 1970.

29. Fox, C. H., Jr., and Lamar, J. E., "Theoretical and Experimental Longitudinal Aerodynamics Characteristics of an Aspect Ratio 0.25 Sharp-Edge Delta Wing at Subsonic, Supersonic, and Hypersonic Speeds," NASA TN D-7651, August 1974.

30. Bartlett, G. E., and Vidal, R. J., "Experimental Investigation of Influence of Edge Shape on the Aerodynamic Characteristics of Low Aspect Ratio Wings at Low Speeds," JAS. Vol. 22, No. 8, August 1955.

31. Marsden, D. J., Simpson, R. W., and Rambird, W. J., "An Investigation into the Flow over Delta Wings at Low Speeds with Leading Edge Separation," Rep. 114, ARC 20409. The College of Aeronautics, Cranfield, February, 1958.

32. Harvey, J. K., "Some Measurements on a Yawed Slender Delta Wing with Leading Edge Separation," RM No. 3160, 1961.

33. Hummel, D., "On the Vortex Formation over a Slender Wing at Large Angles of Incidence," Paper No. 15, AGARD-CP-247, January 1979.

34. Lamar, John E., "Extension of Leading-Edge Suction Analogy to Wings with Separated Flow around the Side Edges at Subsonic Speeds," NASA TR R-428, October, 1974.

35. Manro, M. E., Manning, K. J. R., Hallstaff, T. H., and Rogers, J. T., "Transonic Pressure Measurements and Comparison of Theory to Experiment for an Arrow-Wing Configuration - Summary Report," NASA CR-2610, 1976.

36. Manro, M. E., Manning, K. J. R., Hallstaff, T. H., and Rogers, J. T., "Transonic Pressure Measurements and Comparison of Theory to Experiment for an Arrow-Wing configurements - Data Reports," NASA CR-132727, NASA CR-132728, and NASA CR-132729, October, 1975.

37. Broyden, C. G., "Quasi-Newton, or Modification Methods," Numerical Solution of Systems of Nonlinear Algebraic Equations, edited by G. D. Bryne and C. A. Hall, Academic Press, New York, 1973.

1 Report No	2 Government Accession No	3 Recipient's Catalog No
NASA CR-3278		

4 Title and Subtitle	5 Report Date
An Improved Panel Method for the Solution of Three-Dimensional Leading-Edge Vortex Flows Volume I - Theory Document	July 1980
	6 Performing Organization Code
7 Author(s) F. T. Johnson, P. Lu, E. N. Tinoco, and M. A. Epton	8 Performing Organization Report No
	10 Work Unit No
9 Performing Organization Name and Address Boeing Aerospace Company P. O. Box 3999 Seattle, WA 98124	11 Contract or Grant No NAS1-15169, NAS1-15275
	13 Type of Report and Period Covered Contractor Report December 1977 - May 1977
12 Sponsoring Agency Name and Address National Aeronautics and Space Administration Washington D.C. 20546	14 Sponsoring Agency Code

15 Supplementary Notes

Langley Technical Monitors: James M. Luckring and Ward E. Schoonover, Jr.

Topical Report

16 Abstract

An improved panel method for the solution of three dimensional flow about wing and wing-body combinations with leading edge vortex separation is presented. The method employs a three-dimensional inviscid flow model in which the configuration, the rolled-up vortex sheets, and the wake are represented by quadratic doublet distributions. The strength of the singularity distribution as well as shape and position of the vortex spirals are computed in an iterative fashion starting with an assumed initial sheet geometry. The method calculates forces and moments as well as detail surface pressure distributions. Improvements include the implementation of improved panel numerics for the purpose of eliminating the highly non-linear effects of ring vortices around doublet panel edges, and the development of a least squares procedure for damping vortex sheet geometry update instabilities.

The documentation is divided up into two parts:

Volume I Theory Document
Volume II User's Guide and Programmer's Document

Volume I contains a complete description of the method. A variety of cases generated by the computer program implementing the method are presented which verify the underlying mathematical assumptions of the method and which compare computed results with experimental data to verify the underlying physical assumptions made by the method.

17 Key Words (Suggested by Author(s))	18 Distribution Statement
Leading Edge Vortex Panel Method Three-Dimensional Separation	Unclassified-Unlimited Subject Category 02

19 Security Classif (of this report)	20 Security Classif (of this page)	21 No of Pages	22 Price*
Unclassified	Unclassified	122	$6.50

*For sale by the National Technical Information Service, Springfield, Virginia 22161

NASA-Langley, 1980